Inner Triplet Quadrupole Fringe Fields in the High Luminosity Large Hadron Collider

Thesis submitted in accordance with the requirements of
the University of Liverpool for the degree of Doctor in Philosophy by

Sam Jones

22nd June 2019

Contents

List of Figures

List of Tables

Abstract

The High Luminosity Large Hadron Collider is an upgrade to the Large Hadron Collider which aims to produce more collisions over a single run of the accelerator. To do so, there is an effort to improve the peak luminosity of the existing machine by a factor of 5, and the total luminosity over time (integrated luminosity) by a factor of 10. To increase the luminosity of the machine, one crucial way is to reduce the size of the beam at the point of collision. To make a smaller beam, stronger focusing magnets are required. Furthermore, the beam would also need to reach greater extents in the inner triplet focusing magnets either side of the collision point. To facilitate the beam size in the inner triplet magnets, the magnets require larger distances between poles. However, larger distances between poles means that the tapering of the field at the end of the magnets is more pronounced. These tapering fields are known as fringe fields, and they have a nonlinear dynamical effect on the beam. This could mean a potentially disastrous effect on the beam performance.

The goal of this thesis is to compare different fringe field models, and to observe the differences between them.

An additional objective was to use a tracking code (SAMM) in a study of this kind. This would be to test its extensibility for new work, and for its GPU tracking abilities.

The suitability of an analytic Enge field description for studies involving fringe fields was also an aim of this work.

Though the results presented in this work show variations between the different models, it is still possible that the fringe fields would have a large impact on the beam stability. The result for the Enge field Taylor map showed a significant reduction in the stability of the beam compared to the no fringe model. On the other hand the numeric field Runge-Kutta fringe field model showed the opposite behaviour. Whereas the Enge field Runge-Kutta and the numeric field Taylor map were found to be in closer agreement to the no fringe model.

The analysis was successfully carried out using SAMM. Through this work its functionality was extended to handle new field models and new integration routines. The GPU tracking allowed frequency map analysis to be run on a desktop computer within a reasonable timescale.

The analytic Enge model was shown to be an alternative to a numeric model, but further work is required to find significant differences between them. The Enge model looks like it could be used as a faster alternative to the numeric model in future projects that require fringe field modelling.

Acknowledgements

I would like to thank my supervisors, Andrzej Wolski and David Newton, for their guidance, help, and time. I found both of them be very intelligent and patient men. I am grateful to have worked with them, and to have benefited from their mentorship.

I am very grateful to Sonal Mistry for the emotional and logistical support she has provided me.

I would like to thank all the Cockcroft students who I shared my time at Cockcroft with. I would like to particularly thank Alexandra Alexandrova, Alisa Healey, Chris Edmonds, and Emilia Cruz-Alaniz.

To my family: Dave, Carol, and Jack. I am thankful for your love and support.

I would also like to thank Adam Kewley and Marcus Gallagher-Jones for their feedback and support.

Chapter 1

Introduction

The Large Hadron Collider (LHC) is a particle accelerator that was constructed with the goal of probing physics beyond the Standard Model [1]. The machine is primarily a proton-proton collider[1] with collision energies of 14 TeV. The data collected during the proton-proton collisions is used to probe a range of different physics theories from the Higgs boson to super symmetry. It is the products of the collisions that provide an insight into different physical processes. It therefore follows that generating more collisions will result in more data, and consequently enable statistically acute observations. The amount of collisions is known as the luminosity, and the LHC was designed to have a luminosity with a peak value of $10^{34}\,\mathrm{cm}^{-2}\,\mathrm{s}^{-1}$ [1].

The High Luminosity upgrade to the Large Hadron Collider (HL-LHC) is designed to improve the peak luminosity of the existing machine by a factor of 5, and the total luminosity over time (integrated luminosity) by a factor of 10 [2]. One method to increase the luminosity of the collider is to ensure that the beam size at the point of collision, β^*, is minimised. The smaller the beam size, the higher the density. This increased density of the beams results in an increased probability of collisions.

Several changes to the LHC lattice are necessary to meet the specifications. Central to the work presented in this thesis is the change to the inner triplet (IT) focusing quadrupole magnets. To reduce β^* at the interaction region requires the beam to reach a larger extent in the focusing inner triple quadrupoles either side of the interaction point [3]. To accommodate the larger beam, the magnetic poles are required to be further apart. The further apart the magnets, the greater the fringe fields extend from the edge of the magnets. Fringe fields have a nonlinear effect on the beam and nonlinear effects can significantly reduce the dynamic aperture and stability of the beam.

The work in this thesis aims to identify what potential effects the fringe fields from the new IT magnets could have on the HL-LHC beam.

[1] The LHC can also be run as an ion-ion collider, for ions such as lead atoms.

Four different fringe field implementations have been investigated against each other and the hard-edge model as is used in the HL-LHC v1.0 lattice used in SixTrack. The four models are generated from two fields: a numeric field data from simulation and an analytic Enge field fit to the former, and from two methods of integration: a truncated Taylor map generated from a Wu-Forest-Robin integrator and a Runge-Kutta integrator.

These implementations were compared using several techniques:

1. Transfer functions were employed to examine the focusing properties of the fringe fields.
2. The chromaticity of the lattice was calculated to determine whether the chromaticity of the lattices with fringe fields agreed with the fringe free lattice.
3. The tune shift with amplitude of the lattice was calculated to examine simple differences between the fringe field models. This is a simpler benchmark than the more advanced frequency map analysis.
4. Finally frequency map analysis was performed to test the stability of the beam in phase space and tune space.

Each of the techniques rely on particle tracking to numerically simulate the phase space evolutions of particles within the lattice.

The tracking was performed using a program known as SAMM which allows the simulation to be performed on a graphics card (GPU) using the CUDA language. Graphics cards are known to have higher performance than general processors (CPUs) for highly parallelisable tasks. The studies in this paper benefit from the speed improvement of GPU tracking.

Chapter 2

Literature Review

In this chapter, a background of topics relevant to this thesis is presented. Firstly, to set the context, an overview of the literature detailing the High Luminosity upgrade to the Large Hadron Collider (HL-LHC) is presented. Next, a comparison between the particle tracking codes SAMM and MAD-X is given, to determine whether SAMM could be used in this study. Then the technique of generalised gradients developed by Dragt et al. [4] is critically reviewed, to determine its usefulness in providing accurate transfer maps for fields with longitudinal dependence. Following on, a short description of the use of David Newton's BlitzDA differential algebra code is presented, followed by a review of the analytic fringe field model presented by Muratori et al. [5]. Finally, a short review of frequency map analysis is given.

2.1 HL-LHC studies

2.1.1 The effect of fringe fields on the linear optics of the HL-LHC

Work carried out by Kelly et al. [6] in 2013 demonstrated how the fringe fields of the inner triplet affect the linear optics of the HL-LHC. The optics were analysed using MAD-X [7] in two optics scenarios known as SLHCV3.1b [8] and HLLHCV1.0 [9]. The fringe fields were modelled using three functions each fitted piecewise to simulated magnetic field data. The piecewise fitting uses two exponential models and one arctan model to provide a piecewise analytic model between two chosen points s_0 and s_1. Because of this approach, the nonzero B_z term that must exist in a fringe field is not modelled by the piecewise fitting of the transverse field. The tracking was performed using a thick lens model and the tracking element in MAD-X that corresponds to an inner triplet was replaced with a combination of magnets representing the body and the fringe field. The body was simulated as a truncated magnet with a strength equal to the magnet it replaced. The fringe field was described by many smaller magnets, of equal length, with strength

derived from the functions fit to fringe field data, i.e. each component magnet becomes weaker further away from the body. The authors of the paper measured the change in β-beat due to the fringe fields. β-beating occurs when the bunches oscillate with a different frequency than expected by the Courant-Snyder parameters. It can happen when the bunch and beamline Courant-Snyder parameters are not matched (equal) [10]. They concluded that the changes due to the field would have a detrimental effect on the safety and efficient running of the accelerator.

Though Kelly et al. have successfully shown the impact of fringe fields, there is definitely an opportunity to improve upon these studies by using a more detailed model, as well as looking at potential effects beyond linear optics.

2.1.2 Numeric estimate of the impact of the fringe fields

In a study conducted by Dalena et al. [11] in 2014 a numerical estimate of the impact of fringe fields was presented. The implementation details of how the fringe fields could be integrated into the code SixTrack were also discussed. SixTrack has been described as the workhorse for studies at CERN which require simulation of the beam dynamics [12], and a particular topic noted by the paper was dynamic aperture studies. The authors use magnetic field data to construct generalised gradients.

The study then compares a Lie algebra transformation, which uses the vector potential calculated from the generalised gradients, to a symplectic integrator, which uses the Lorentz force and finds them comparable. This is a useful result because it shows generalised gradients can be used to process the inner triplet field.

2.1.3 Dynamic aperture studies for the HL-LHC optics

De Maria et al. [13] in 2015 conducted dynamic aperture studies in the HL-LHC. This was to determine the inner triplet field quality necessary to meet the machine's dynamic aperture requirements. This study did not include quadrupole fringe fields.

Dynamic aperture studies are presented for the HL-LHCV1.0 lattice with round beam optics of $\beta^* = 15$ cm. It was found that the dynamic aperture is a lot smaller compared to a lattice with a larger β^*.

The dynamic aperture results serve as an interesting comparison with the frequency map analysis performed in this study.

2.2 Benchmarking SAMM against PTC and MAD-X using LHC optics

The Simple Accelerator Modelling in Matlab (SAMM) code [14] is used in this thesis and described in more detail in section 4.5. A paper by Hock et al. [15] in 2013 presents benchmarks of SAMM against PTC [16] and MAD-X [7]. In that study a MAD-X sequence file (LHC V6.500) is used for describing a set of LHC optics. Each program is used to interpret the optics files and then the tracking results were compared. Additionally, results of tracking through individual elements such as a quadrupole or kicker were also compared. The paper found that whilst there were many agreements in the results between the codes, there were some differences also. The paper notes that SAMM and MAD-X use the paraxial approximation. The paraxial approximation is used in the Wu-Forest-Robin integrator employed in this thesis. The paraxial approximation is an approximation that can be made to expand the Hamiltonian by assuming that the transverse momenta of the particles is small. Obviously this approximation may not be appropriate if the transverse momenta of the particles is large, such as in the focusing portion of a collider.

The paper suggests that the SAMM code could be a suitable candidate for beam tracking studies. The simulation results for SAMM are in broad agreement with two other well understood codes (MAD-X and PTC). SAMM code offers the additional advantage of being flexible enough to allow the addition of bespoke features, such as GPU tracking and implementation of new integration routines, which have been used in the production of the results presented in this thesis.

2.3 Generalised gradients

In Mitchell et al. [4], a system is presented which allows high order derivatives of field data to be computed in the representation of analytic generalised gradients. It is mentioned that the generalised gradients rely on numeric field data to be fit onto a bounding cylinder. In this geometric setup, harmonic fields take their extrema on the boundary and are subject to a feature known as smoothing; this means that any noise on the surface is damped towards the interior of the cylinder. This effect is more pronounced for larger cylinder diameters. From the fitted surface field data the analytic generalised gradients can be calculated, and from the gradients the magnetic field, B, magnetic scalar potential, ϕ, and magnetic vector potential, A, can also be calculated. These results can then be used in integrators to produce an accurate transfer map up to high orders, as it is tolerant to noise amplification from differentiation as a result of the smoothing feature. Mitchell et al. uses a non-physical monopole doublet setup for benchmarking; a proposed ILC damping ring wiggler is also used for benchmarking [17]. The monopole doublet is

analytically solvable but requires high order derivatives. It was found that the monopole doublet setup was accurately described with a small impact from noise even up to 7th order, and that the noise can be further reduced by more points in the surface field data. The study found good agreement in the case of the ILC damping ring wiggler.

One limitation of the generalised gradients is that it does a poor job of calculating values outside of the cylinder used to produce the generalised gradients. This is because the damping of errors inside the cylinder also has the side effect that errors grow exponentially outside of the cylinder. For this reason the generalised gradients should not be used to calculate field values outside the cylinder.

To conclude, there is scope to use these techniques to describe a fringe field.

2.4 Differential algebra BlitzDA code

D. Newton developed a C++ differential algebra code (BlitzDA) for storing, manipulating, and applying mathematical operations to polynomial objects. When used in conjunction with the generalised gradient technique, the code is able to store a polynomial description of magnetic or electric fields which are decomposed into their multipole elements and spatial derivatives. It has been used to describe inner triplet magnets in the HL-LHC [18], or electrostatic elements of ELENA [19, 20] and g-2 [21].

Therefore it is an appropriate tool to use for applying the generalised gradient technique to the fields studied in this thesis.

2.5 Analytic description of a fringe field

In a study by Muratori et al. [5] in 2015 an analytic description of fringe fields of multipole magnets was developed. Importantly the fringe fields of quadrupole magnets and higher order magnets can be described using the expressions derived in this paper. This is advantageous because whilst dipole fringe fields are easily modelled and implemented in numeric tracking, implementing quadrupoles and higher order fringe fields depends on numeric field models or series expansion from the axis. Numeric field models require detailed models of the magnet or direct empirical measurement. Therefore future particle tracking studies can take advantage of the techniques described in this paper to allow fringe field effects to be taken into account earlier than would otherwise have been possible. When considering series expansion about the axis, another advantage that the expressions provide is that they are analytic in the transverse plane, which is a more suitable model than series expansion for beams that cannot be assumed to travel along the beam axis. In this paper, two examples used for benchmarking the analytic description include an inner triplet quadrupole from the HL-LHC, and a magnet from

the non-scaling FFAG EMMA [22]. The analytic expressions in both cases are in good agreement with numerical field maps.

There is scope for an investigation into whether the differences between a numeric field map and analytic expression would produce differences in particle tracking studies with strong nonlinear dynamic features.

2.6 Frequency map analysis

Frequency map analysis is a technique for analysing the stable and chaotic motion at different points in phase space. It was originally used in "celestial mechanics, galactic dynamics, atomic physics Hamiltonian toy models" [23]; its use in particle accelerators was outlined by Laskar [24]. Later, Papaphilippou uses frequency map analysis to investigate some of the nonlinear dynamical properties of the LHC lattice [25, 23].

Generally speaking, frequency map analysis is used in conjunction with the method Numerical Analysis of Fundamental Frequencies (NAFF). NAFF is able to determine the fundamental frequencies (represented by peaks in frequency space) with an accuracy orders of magnitude better than a Fourier transform alone [26].

Frequency map analysis is a useful tool because it can be used to identify more unstable regions of the beam. These unstable regions can be used as an estimate of the dynamic aperture. Using the frequency map analysis to find the dynamic aperture is better than using survival studies which requires orders of magnitude more tracking and is therefore much less efficient.

Chapter 3

Physics Theory

In this section, the theoretical concepts that underpin the results of the work done in this thesis will be detailed.

3.1 Magnets in accelerators

Magnetic fields are a key tool for directing the motion of charged particles. This section will introduce general concepts for working with magnetic fields. Focus will then move to quadrupoles individually, and after introducing the High Luminosity upgrade to the Large Hadron Collider (HL-LHC) lattice, their part to play within this lattice will be explored. Finally the magnetic field models will be expanded to the case of fields with s-dependence (such as fringe fields which are the continuous nonlinear tapering of a field between full field and zero field regions). A concept called generalised gradients will be discussed and its advantages in relation to s-dependent fields.

3.1.1 Multipole fields

Particle accelerators rely on electromagnetic fields to control the charged particles within them. The forces these fields generate on the charged particles can be used to steer, focus, and accelerate charged particles This can be seen in the Lorentz force:

$$F_{\mathrm{EM}} = q\left(E + v \times B\right) . \tag{3.1}$$

The electromagnetic force, F_{EM}, is the sum of the contributions due to the electric field, E, and the magnetic field, B. The left hand side of the sum is the force acting parallel and due to the electric field. The vector cross product on the right hand side of the equation means that the force due to the magnetic field requires a moving particle with

charge, q, and it acts perpendicular to both the magnetic field and velocity of the charge, v. Therefore the action that can be taken upon the charged particles is constrained by the electromagnetic system that can be created.

The electromagnetic fields themselves must obey Maxwell's equations, which can be stated as follows:

$$\nabla \cdot D = \rho \,, \tag{3.2}$$

$$\nabla \cdot B = 0 \,, \tag{3.3}$$

$$\nabla \times E = -\frac{\partial B}{\partial t} \,, \tag{3.4}$$

$$\nabla \times H = J + \frac{\partial D}{\partial t} \,. \tag{3.5}$$

There are several new parameters introduced in Maxwell's equations above. The sources of the electromagnetic field are the electric charge density, ρ, and electric current density, J. The permittivity of free space, ϵ_0, and the vacuum permeability, μ_0, both are constants defined in vacuum to be:

$$\epsilon_0 = \frac{1}{\mu_0 c^2} \,, \tag{3.6}$$

$$\mu_0 = 4\pi \times 10^{-7} \mathrm{Hm}^{-1} \,, \tag{3.7}$$

where μ_0 has the units of henries per metre.

The speed of light, c, is also defined in relation to these constants as:

$$c = \frac{1}{\sqrt{\epsilon_0 \mu_0}} \,. \tag{3.8}$$

The electric permittivity, ϵ, and magnetic permeability, μ, constants are described by:

$$\epsilon = \epsilon_r \epsilon_0 \,, \tag{3.9}$$

$$\mu = \mu_r \mu_0 \,, \tag{3.10}$$

where the ϵ_r and μ_r are the relative permittivity and relative permeability respectively of the material in which the fields propagate. Lastly the electric displacement, D, and magnetic intensity, H, are related to the magnetic field, B, and electric field, E, by:

$$D = \epsilon E \,, \tag{3.11}$$

$$B = \mu H \,, \tag{3.12}$$

The fields themselves in the region in which the particles travel can be assumed to be charge free, and therefore the fields must also obey the charge-free Laplace equation:

$$\Delta V \equiv \nabla^2 V = 0 \,, \tag{3.13}$$

where V is the magnetic scalar potential. When written in cylindrical coordinates this becomes [3, eq. 3.2]:

$$\Delta V = \frac{\partial^2 V}{\partial r^2} + \frac{1}{r}\frac{\partial V}{\partial r} + \frac{1}{r^2}\frac{\partial^2 V}{\partial \phi^2} + \frac{\partial^2 V}{\partial z^2} \equiv 0 \,. \tag{3.14}$$

Equation (3.14) has a solution that, whilst it is not general, does contain all multipole fields which will be described shortly [3, eq. 3.3]:

$$V = -R_b \sum_{n \geq 0} \frac{1}{n!} A_n r^n e^{in\phi} \,, \tag{3.15}$$

$$V = -R_b \sum_{n \geq 0} \frac{1}{n!} A_n \left(x + iy\right)^n \,, \tag{3.16}$$

where A_n are field coefficients derived from eq. (3.14), and R_b is the beam rigidity. The beam rigidity is defined as:

$$R_b = B\rho = \frac{P_0}{q} = \frac{\beta E}{qc} \,, \tag{3.17}$$

where B is the magnetic field needed to steer a beam with rigidity, R_b (in T m), along a circle of gyroradius ρ. This can also be represented in terms of P_0 the reference momentum of the beam, and q the charge of the particles that make up the beam.

The magnetic field is related to the magnetic scalar potential as follows [3]:

$$B = \mu H = -\mu \nabla V \,, \tag{3.18}$$

where H is the magnetic H-field which satisfies eq. (3.12).

The constants in eq. (3.16) and the factor μ introduced by eq. (3.18) can be represented by:

$$C_n = \frac{\mu R_b A_n}{n - 1!} \,. \tag{3.19}$$

Using the relation in eq. (3.18), a standard set of fields known as the multipole fields can be derived. The derivations are shown below as outlined by Wolski in [10]. The multipole fields are solutions to Maxwell's equations and the wave equation. They can be described by eq. (3.20):

$$B_y + iB_x = \sum_{n=1}^{\infty} C_n \left(x + iy\right)^{n-1} \,, \tag{3.20}$$

where the index n refers to the multipole field (where $n = 1$ is a dipole field, $n = 2$ is a quadrupole field, etc) and C_n are the multipole coefficients. The zeroth order multipole field is the solenoid term that usually has zero B_x, B_y terms and non-zero B_z, therefore it is not considered a multipole field. The multipole coefficients can be represented as:

$$C_n = |C_n| e^{i\phi_n} \,, \tag{3.21}$$

$$C_n = b_n + ia_n \,. \tag{3.22}$$

Equation (3.21) shows that each multipole coefficient, C_n, can be represented as a scalar value and an associated phase. C_n has units that depend on the order of the multipole, n, C_1 has units of the dipole field (T), C_2 has units of the quadrupole field gradient ($\mathrm{T\,m^{-1}}$), C_3 has units of the sextupole field strength ($\mathrm{T\,m^{-2}}$), and so on.

The multipole components b_n and a_n quantify the normal and skew components respectively. In the case that the multipole components are represented as dimensionless quantities, such as in eq. (3.24), then a reference field B_{ref} and reference radius R_{ref} are required for scaling.

$$B_y + iB_x = B_{\mathrm{ref}} \sum_{n=1}^{\infty} |C_n| e^{i\phi_n} \left(\frac{re^{i\theta}}{R_{\mathrm{ref}}}\right)^{n-1} \tag{3.23}$$

$$B_y + iB_x = B_{\mathrm{ref}} \sum_{n=1}^{\infty} \left(b_n + ia_n\right) \left(\frac{x + iy}{R_{\mathrm{ref}}}\right)^{n-1} \tag{3.24}$$

The surface of the magnetic poles should be shaped such that the magnet follows an equipotential line of magnetic scalar potential, from eq. (3.1) associated with the required field [10, p23].

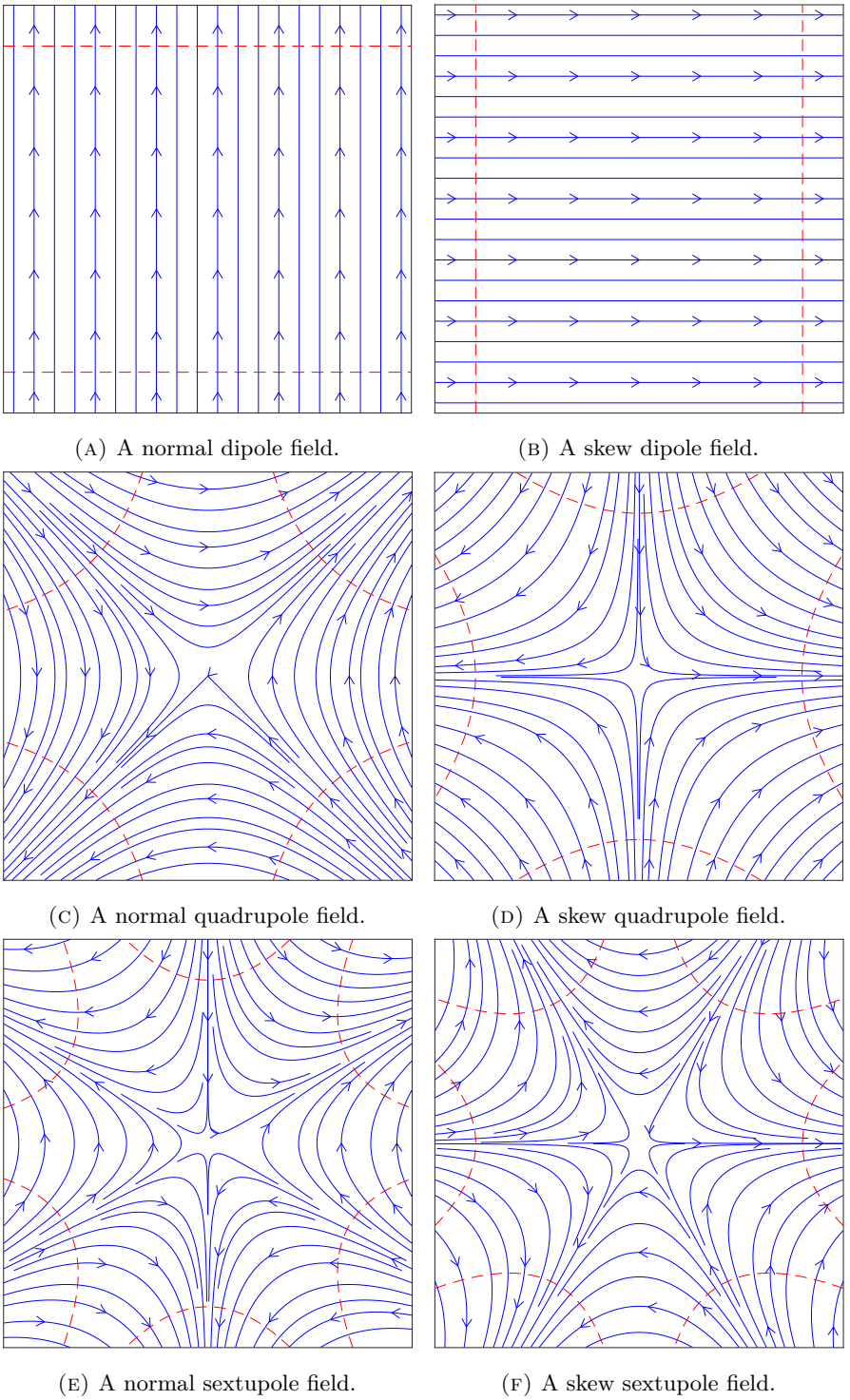

(A) A normal dipole field.

(B) A skew dipole field.

(C) A normal quadrupole field.

(D) A skew quadrupole field.

(E) A normal sextupole field.

(F) A skew sextupole field.

FIGURE 3.1: The field line (blue) and pole face (red) geometries for normal and skew multipoles from dipole up to sextupole.

The shape of the multipole fields from dipole, $n = 1$, up to octupole, $n = 4$, as well as the dodecapole field, $n = 6$, represented by eq. (3.20) are shown in figs. 3.1 and 3.2. As

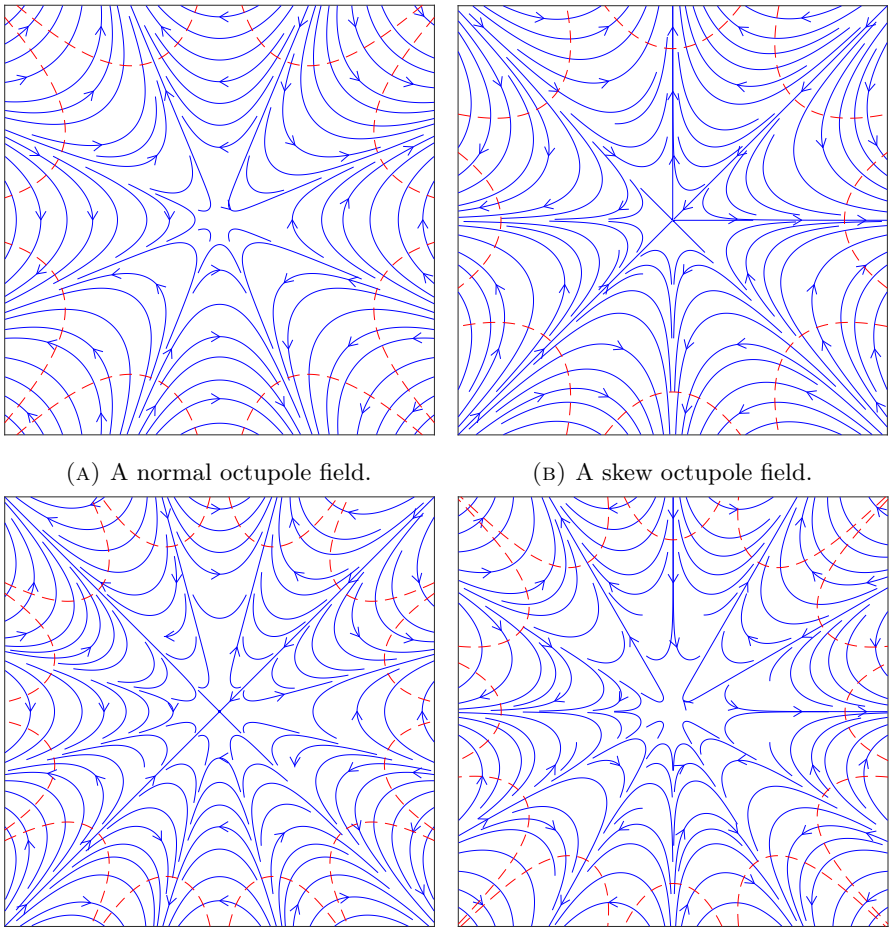

(A) A normal octupole field.

(B) A skew octupole field.

(C) A normal 12-pole field.

(D) A skew 12-pole field.

FIGURE 3.2: The field line and pole face geometries for normal and skew multipoles of the octupole and dodecapole (12-pole). The dodecapole has a sign change under $\pi/12$ and as such is an allowed higher order multipole of the quadrupole.

can be seen in figs. 3.1 and 3.2, it is apparent that there is a set of orthogonal fields with a rotation around the z axis of $\pi/2n$. These are known as skew multipoles in comparison with the unrotated normal multipoles.

Upon further inspection it is evident that the field direction is reversed upon each π/n rotation of the field around the z axis. In terms of the phase in eq. (3.21), normal multipoles occur when $\phi_n = 0$ or $\phi_n = \pi$ and skew multipoles when $\phi_n = \pm\pi/2$. In terms of the dimensionless representation in eq. (3.22), normal multipoles occur when $a_n = 0$ and skew multipoles when $b_n = 0$.

A rotation of π/n about the z axis is equivalent to a change in ϕ_n by $-\pi$. Consider a field that is a combination of two multipoles of order m and n with $m \neq n$. Then a rotation of the field by π/n is equivalent in a change of ϕ_n by $-\pi$, but a change in ϕ_m is equal to a change of $-m\pi/n$. Therefore to maintain symmetry (a change of sign through a rotation of π/n) the following must be true:

$$e^{-im\pi/n} = -1\,. \tag{3.25}$$

Euler's identity and symmetry under 2π mean that eq. (3.25) leads to the result that $m/n = 3, 5, 7, \ldots$. It may not seem intuitive that higher order multipoles are given by odd integer multipoles - but this is a necessary requirement to satisfy a change of sign for a π/n rotation. Figure 3.2 shows this clearly; in the case of a quadrupole multipole, $n = 2$, a rotation of π/n would result in an identical field for the octupole, where the 12-pole would have a change of sign. The higher order multipoles symmetries, that satisfy eq. (3.25) for a given multipole n are known as allowed multipoles, and those that do not as forbidden multipoles.

Production of pure multipole fields require infinitely long magnets, that are transversely homogeneous.

3.1.2 Quadrupoles

The Lorentz force from eq. (3.1) states that the resultant force on a charge is perpendicular to both a magnetic field and the direction of the charge through the field. A particle travelling normal to the dipole field, as seen in fig. 3.1a, will experience forces in the horizontal plane. Dipole fields therefore are often used to steer beams.

The quadrupole field can be seen in fig. 3.1c, from the figure it is evident that the field geometry of a quadrupole is more complicated than that of the dipole. The quadrupole term of the multipole expansion, $n = 2$, taken from eq. (3.20) is as follows:

$$B_y + iB_x = B_{\text{ref}}\,(b_2 + ia_2)\left(\frac{x+iy}{R_{\text{ref}}}\right)\,. \tag{3.26}$$

The gradient of a quadrupole field is linear which can be seen when taking the derivative of eq. (3.26),

$$\frac{\partial B_y}{\partial x}_{\,y=0} = B_{\text{ref}}\frac{b_2 + ia_2}{R_{\text{ref}}}\,. \tag{3.27}$$

The quadrupole field is focusing in one direction whilst defocusing in the other as can be seen in fig. 3.3.

A combination of alternating gradient quadrupoles separated by drifts provides strong focusing in both axes of the transverse plane. This combination is known as a FODO lattice and the physics behind it is covered in more detail in section 3.2.7.

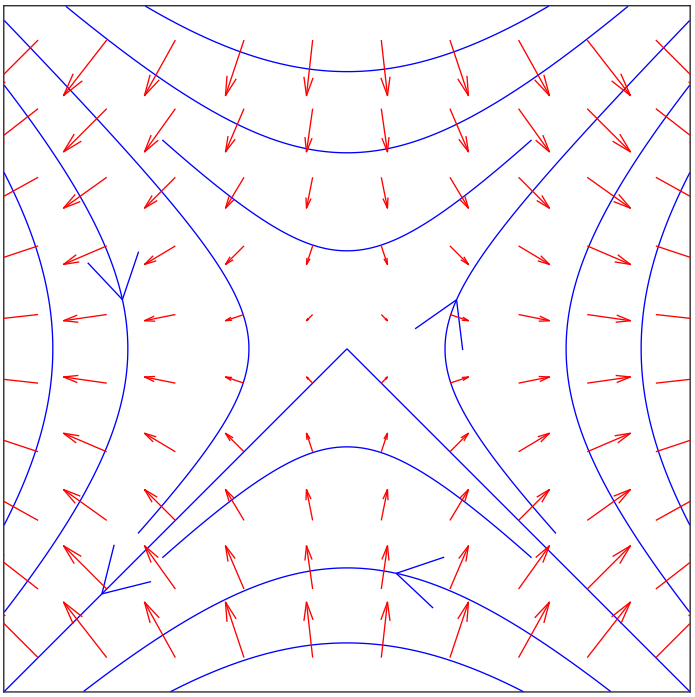

FIGURE 3.3: The force field (red) on a positive charge, travelling perpendicularly and into the plane of the paper, due to a normal quadrupole field (blue).

Quadrupole magnets transversely focus a particle beam and when used in conjunction with bending dipole magnets are the basis of determining the desired path of a beam within an accelerator [3, p68].

3.1.3 HL-LHC lattice

The High Luminosity Large Hadron Collider (HL-LHC) aims to increase the number of collisions by a factor of 5 compared to the Large Hadron Collider [2].

There are several key improvements to the LHC lattice that were designed with this goal in mind. The most important one for this discussion is the implementation of new focusing quadrupoles. These quadrupoles come in the form of triplets either side of the interaction (collision) points. One way to produce more particle collisions is to reduce the size of the beam at the interaction point, known as β^*. To accomplish a reduction in β^*, the size of the beam at the inner triplet quadrupoles must be large, and the inner triplet must therefore have a stronger field gradient. Therefore the quadrupoles must be designed with a larger aperture (the distance between magnetic poles) to accommodate the beam, as well as having a larger field gradient.

The instantaneous luminosity of the HL-LHC can be described by [27]:

$$L = \frac{n_b N^2 f_{\text{rev}} \gamma}{4\pi\sigma^{*2}} F \,, \tag{3.28}$$

where n_b is the number of bunches in lattice at one time. N is the number of particles per bunch. f_{rev} is the revolution frequency for a particle with reference momentum. γ is relativistic gamma. β^* is a measure of the beam size at the interaction point. ϵ_n is the normalised emittance of the beam [27].

$$F = 1/\sqrt{1 + \left(\frac{\theta_c \sigma_z}{2\sigma^*}\right)^2}, \tag{3.29}$$

F is a luminosity reduction factor due to geometric effects from the crossing angle and hourglass effect. $\sigma^*$and σ_z are the transverse and longitudinal r.m.s beam sizes respectively [27].

The specifics of the lattice parameters are detailed in table 3.1 [2, Table 2.1]. The relevant parameters with respect to luminosity improvements between the nominal LHC and HL-LHC are: the number of particles per bunch (which has increased), β^* (which has reduced), and the normalised emittance (which has reduced). These improvements are mitigated by: a larger crossing angle and increased normalized beam-beam separation, and a smaller number of bunches per beam. The result of these changes is a predicted peak luminosity for the HL-LHC of 7.18 compared to $1 \times 10^{34}\,\text{cm}^{-2}\text{s}^{-1}$ for the nominal LHC.

The specifics of the lattice optics are detailed in table 3.2 [2, Table 2.2]. The HL-LHC has been described by several succeeding lattice configurations SLHCv3.1b [8], HLLHCv1.0 [9], and HLLHCv1.1 [28]. One key difference between them is the choice of inner triplet magnets. SLHCv3.1b implements higher gradient $150\,\text{Tm}^{-1}$ Nb3Sn magnets and overall shorter magnetic length. HL-LHC v1.0 and HL-LHC v1.1 are based on $140\,\text{Tm}^{-1}$ Nb3Sn magnets, but have a longer magnetic length, with Q1 and Q3 each split into two components. To help visualise the differences between the LHC and the HL-LHC, a schematic of the inner triplet is shown in fig. 3.4 [2, Figures 3.1 & 3.2].

A plot of the Courant-Snyder parameters of the inner triplet of the HL-LHC is shown in fig. 3.5 [2, Figure 2.4]. The properties of a lattice can be described by Courant-Snyder parameters (which are also commonly known as Twiss parameters) which are discussed further in section 3.2.8. It is relevant to state here that the β functions is a description of the relative beam size at a point in the lattice. As can be seen in fig. 3.5, β becomes much larger either side of the interaction region reaching its greatest extent in the inner triplets. This is necessary in order to reach a small β^*. The larger β in the inner triplets will thus result in a beam that is spread across a larger transverse area, and will result in particles with larger amplitudes from the closed orbit. Particles with larger amplitudes will be more affected by the nonlinear dynamics of the quadrupole fringe fields. This is explained in more detail in the relevant subsections of section 3.2.

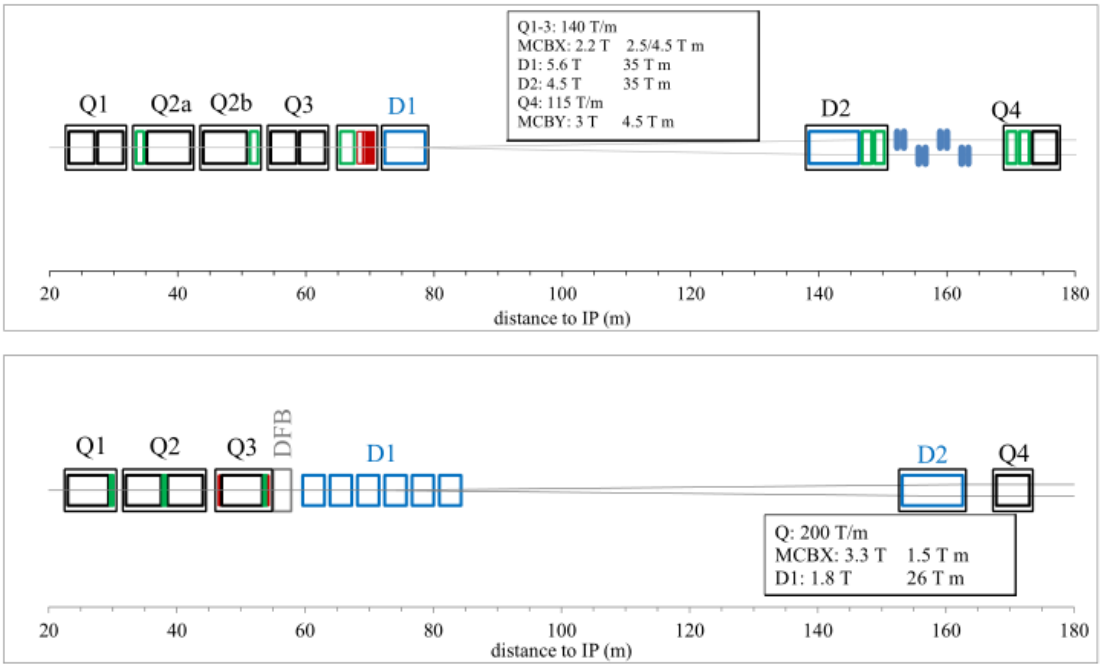

FIGURE 3.4: A schematic of the inner triplet configurations of the HL-LHC (top image) and LHC (bottom image). The comparison between the field strengths of the quadrupoles (Q) and dipoles (D) and their distances from the interaction point (IP) is shown. The magnets have thick black outlines and cryostats that contain the magnets have thin black outlines [2].

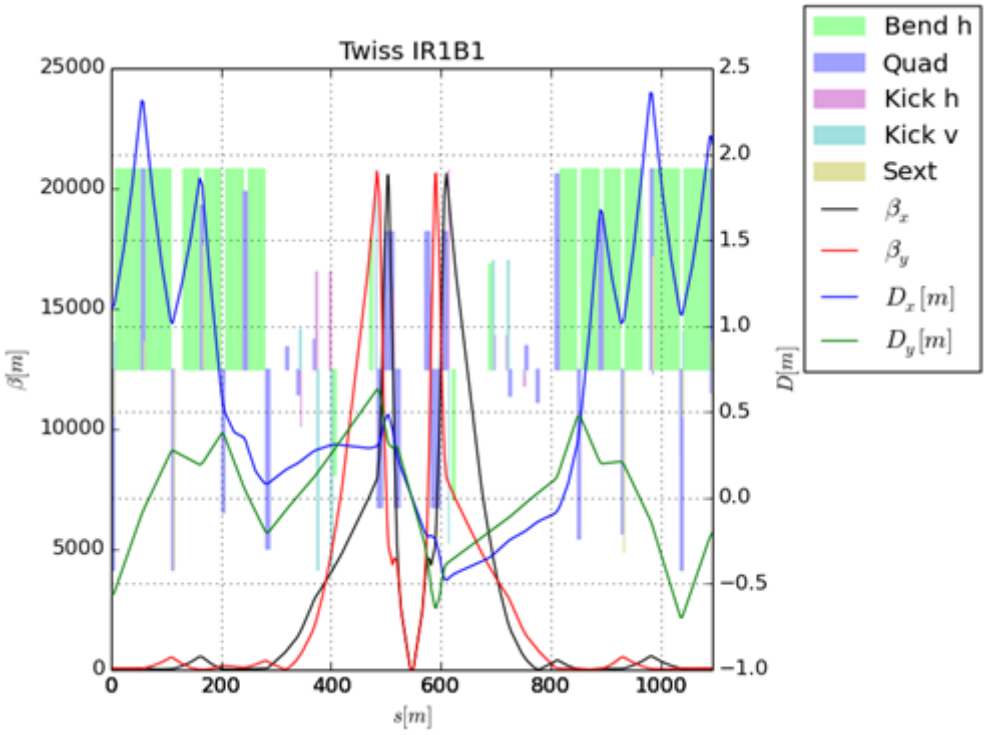

FIGURE 3.5: The Courant-Snyder parameters, for collision optics, in a 1000m section of inner triplet section which includes an interaction point [2].

Parameter	Nominal LHC (design report)	HL-LHC (standard)	HL-LHC (BCMS)
Beam energy in collision [TeV]	7	7	7
Particles per bunch, N [10^{11}]	1.15	2.2	2.2
Number of bunches per beam	2808	2748	2604
Number of collisions in IP1 and IP5[1]	2808	2736	2592
N_{tot} [10^{14}]	3.2	6.0	5.7
Beam current [A]	0.58	1.09	1.03
Crossing angle in IP1 and IP5 [μrad]	285	590	590
Normalized long range beam-beam separation [σ]	9.4	12.5	12.5
Minimum β^* [m]	0.55	0.15	0.15
ε_n [μm]	3.75	2.50	2.50
ε_L [eVs]	2.50	2.50	2.50
r.m.s. energy spread [0.0001]	1.13	1.13	1.13
r.m.s. bunch length [cm]	7.55	7.55	7.55
IBS horizontal [h]	105	18.5	18.5
IBS longitudinal [h]	63	20.4	20.4
Piwinski parameter	0.65	3.14	3.14
Total loss factor R_0 without crab-cavity	0.836	0.305	0.305
Total loss factor R_1 with crab-cavity	-	0.829	0.829
Beam-beam / IP without crab cavity	0.0031	0.0033	0.0033
Beam-beam / IP with crab cavity	0.0038	0.011	0.011
Peak luminosity without crab-cavity [10^{34} cm^{-2}s^{-1}]	1.00	7.18	6.80
Virtual luminosity with crab-cavity $L_{peak}\times R_1/R_0$ [10^{34} cm^{-2}s^{-1}]	(1.18)	19.54	18.52
Events/crossing without levelling and without crab-cavity	27	198	198
Levelled luminosity [10^{34} cm^{-2}s^{-1}]	-	5.00[2]	5.00[2]
Events/crossing (with levelling and crab-cavities for HL-LHC)[3]	27	138	146
Maximum line density of pile up events during fill [event/mm]	0.21	1.25	1.31
Levelling time [h] (assuming no emittance growth)[3]	-	8.3	7.6
Number of collisions in IP2/IP8	2808	2452/2524[4]	2288/2396[4]
N at LHC injection [10^{11}][5]	1.20	2.30	2.30
Maximum number of bunches per injection	288	288	288
N_{tot} / injection [10^{13}]	3.46	6.62	6.62

TABLE 3.1: The comparison of machine parameters for the LHC and HL-LHC [2, Table 2.1].

3.1.4 Fringe fields

In many applications it is reasonable to assume that the magnetic field does not vary with longitudinal position. There is a further assumption that the field stops at some position and there is a discontinuous change to a field-free region.

In reality the field of a magnet must falloff continuously in the boundary region between the body of a magnet and a field-free region. The field in this boundary region is known as a fringe field. The size of the fringe field is determined in part by the size of the aperture of the magnet. A larger apertures means that the fallout region will also be larger. As discussed in section 3.1.3, the inner triplet magnets have been designed with larger apertures than before; in combination with the larger field gradient, the resultant fringe fields will have a larger effect than those of the existing focusing magnets.

	SLHC V3.1b	HLLHCV1.0	HLLHCV1.1 (Baseline)
Collision β* IP1,5	Round: 15cm, (10 cm, 33 cm, 40 cm). Flat: 30/7.5cm, (20/5 cm) with HV, VH crossing.	Round: 15cm, (10 cm). Flat: 30/7.5cm, (20/5 cm) with HV, VH crossing. Complete squeeze.	
Pre-squeeze β* IP1,5	40 cm, (2 m)	44 cm, (3 m) transition strengths.	44 cm
Injection β* IP1,5	5.5 m, (11 m)	6 m, (11 m, 18 m)	6 m (15 m)
Triplet gradient	150 T/m	140 T/m	140 T/m
Triplet magnetic length	Q1-Q3: 7.685 m Q2: 6.577 m	Q1-Q3: 4.002 m ×2 Q2: 6.792 m	Q1-Q3: 4.00 m ×2 Q2: 6.8 m
Triplet corrector package	Nested triplet nonlinear corrector package with new a_5, b_5, a_6 corrector coils	Super ferric, non-nested, nonlinear corrector package.	
Insertion region dipoles	D2 moved towards the IP by 15 m. For version HLLHCV1.1 the magnetic length of D1 [35] and D2 has been shortened.		
Insertion region quadrupoles	MQYY type for Q4 in IR1,5. Q5 moved towards arc by 11m. MQYL type for Q5 in IR1,5,6. Additional MS in Q10 of IR1 and IR5.	MQYY type for Q4 in IR1,5. Q5 moved towards the arc by 11m. MQYL type for Q5 in IR1,5,6. Additional MS in Q10 of IR1 and IR5.	Q4 moved towards arc by 8m. MQYY type for Q4 in IR1,5. Q5 moved towards arc by 11m. MQY at 1.9 K type for Q5 in IR1,5. Double MQY for Q5 in IR6. Additional MS in Q10 of IR1,5.
Crab cavities	3		4

TABLE 3.2: The comparison of machine optics for the LHC and HL-LHC [2].

Fringe fields have a non-linear effect on the beam dynamics. Changes to the nonlinear dynamics of a beam can produce substantial changes to a beam. It is therefore important to understand and determine if the fringe fields of the HL-LHC inner triplet will have any major effect on the HL-LHC beam.

3.1.5 Enge fields

The Enge field is a model that approximates the fall-off of a field between a field-free region and the body of a magnet.

The equation for an Enge field is given by [29][30]:

$$F(s) = 1/\left[1 + \exp\left(\sum_{i=1}^{N} a_i \left(\frac{s}{D}\right)^{i-1}\right)\right] . \tag{3.30}$$

Therefore, by eq. (3.30) a three parameter Enge field would be:

$$F(s) = 1/\left[1 + \exp\left(a_1 + a_2\left(\frac{s}{D}\right) + a_3\left(\frac{s}{D}\right)^2\right)\right] . \tag{3.31}$$

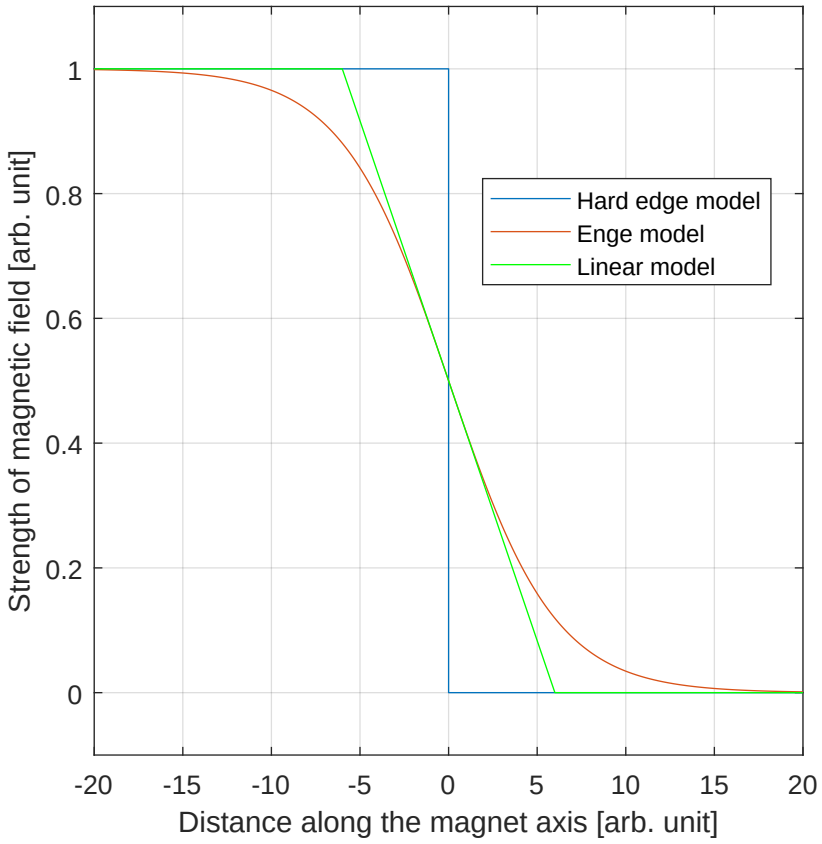

FIGURE 3.6: A comparison of a hard-edge field model against a linear model and also an Enge fringe field model.

The advantage of such a model is that it is simple to calculate for a given set of parameters. Different fringe fields can be modelled by varying the Enge parameters, a_i.

One disadvantage of such a model is that it may not provide detailed enough features to accurately portray the physical reality of a fringe field. Furthermore, the fitting of an Enge field is complicated by the matter that the Enge parameters are dependent on each other. For instance, adding an extra parameter requires recalculation of all parameters.

3.1.6 Generalised gradients

There will always be some level of uncertainty about the nature of reality, and sometimes this is a limiting factor in the ability to construct the most accurate models. In other cases though it may be that the limiting factor to construct an accurate model is instead due to the intrinsic description or construction of the model itself. The next technique to be discussed places some restrictions upon the electric or magnetic field; these restrictions can provide advantages and a framework for reasoning about the fields themselves. The

technique involves the generation of a set of functions known as *generalised gradients* that model the fields in an accelerator component [31].

For magnetic fields with high order which may impact on the beam dynamics of an accelerator, it may be necessary to construct a transfer map that is an accurate model of the high order impact from the component. High order transfer maps will require high order derivatives; unfortunately a direct approach of iterating through each derivative by calculating each numerically from field data is very sensitive to noise. Factors like truncation, round-off, or error on the field measurements can have too large an impact on numerically calculated high order derivatives. Instead of a direct numeric approach, the generalised gradients technique uses the field data to generate a set of functions that satisfy Maxwell's equations and can be differentiated analytically to calculate higher order terms. The field described by the generalised gradients must differ from the field used to generate it, but it also has a property known as numeric error smoothing. The smoothing means the errors on the field description becomes smaller the closer to the central axis of the model. It is important to note that the errors on the field description grow larger when calculating fields radially outside of the cylinder. Therefore the generalised gradients should not be used to extrapole fields outside of the original cylinder used to create it [1].

There are several methods for calculating generalised gradients. These involve the use of field data situated on circular, elliptical, or rectangular cylinders. They can also be found using potential data on a circular cylinder. The data from an experimental or theoretical model does not have to lie on these cylinders required for the generalised gradients. Instead the data required at points on the surface of the cylinder can be calculated via interpolation.

In this study generalised gradients were calculated using the normal component of the magnetic field on the surface of a circular cylinder, $B_\rho\left(R,\phi,z\right)$. The first step is to perform Fourier transforms on the surface data along ϕ and z [31, eq 17.3.1 & 17.3.2] [2]:

$$\tilde{B}_\rho\left(R,m,z\right)=\frac{1}{2\pi}\int_0^{2\pi}d\phi\exp\left(-im\phi\right)B_\rho\left(R,\phi,z\right)\ , \tag{3.32}$$

$$\tilde{\tilde{B}}_\rho\left(R,m,k\right)=\frac{1}{2\pi}\int_{-\infty}^{\infty}dz\exp\left(-ikz\right)\tilde{B}_\rho\left(R,m,z\right)\ . \tag{3.33}$$

The Fourier transforms can be performed in either order to get the following result [31, eq 17.3.3]:

[1] The inner triplet quadrupoles studied in this work are designed to be placed at parts of the lattice where the beam is far from the magnetic axis. As will be seen in section 4.1, the cylinder cross section chosen to calculate the generalised gradients is much larger than the maximum extent of the particles in the inner triplet of the HL-LHC.

[2] Unless otherwise stated i is the imaginary unit $i=\sqrt{-1}$.

$$\tilde{\tilde{B}}_\rho(R,m,k) = [1/2\pi]^2 \int_{-\infty}^{\infty} dz \exp(-ikz) \int_0^{2\pi} d\phi \exp(-im\phi) B_\rho(R,\phi,z) \ . \tag{3.34}$$

The normal component of the magnetic field is related to the scalar potential of the field by [31, eq 17.3.4]:

$$B_\rho(R,\phi,z) = [\partial_\rho \psi(\rho,\phi,z)]_{\rho=R} \ . \tag{3.35}$$

This equation is equivalent to the expression from eq. (3.18), but for the case of the normal component on cylindrical geometry. Dragt derives a general scalar potential, ψ, in cylindrical coordinates that satisfies Laplace's equation [31, eq. 15.3.7]. Substituting that expression of the scalar potential in to eq. (3.35) gives [31, eq 17.3.5]:

$$B_\rho(R,\phi,z) = \sum_{m=-\infty}^{\infty} \int_{-\infty}^{\infty} dk G_m(k) \exp(ikz) \exp(im\phi) kI_m(kR) \ , \tag{3.36}$$

where $I_m(kR)$ are the modified Bessel functions, and $G_m(k)$ are arbitrary functions.

Dragt has derived an expression of the generalised gradients, $C_m^{[n]}(z)$, in terms of the arbitrary functions, $G_m(k)$, from the general scalar potential solution [31, eq. 15.3.15]. Dragt shows that by substituting eq. (3.36) into eq. (3.34), that the generalised gradients can now be stated in terms of the Fourier transformed field, $\tilde{\tilde{B}}$ [31, eq 17.3.8]:

$$C_m^{[n]}(z) = i^n (1/2)^{|m|} (1/|m|!) \int_{-\infty}^{\infty} dk \left[k^{n+|m|-1}/I_m(kR)\right] \tilde{\tilde{B}}_\rho(R,m,k) \exp(ikz) \ . \tag{3.37}$$

The exponential smoothing mentioned earlier is a result [31, eq 17.3.9]:

$$|I_m(kR)| \sim \exp(|k|R) / \sqrt{2\pi|k|R} \text{ as } |k| \to \infty \, . \tag{3.38}$$

As $I_m(kR)$ is in the denominator of eq. (3.37) it means that the contributions from high order noise are exponentially reduced.

Whilst deriving a general solution to Laplace's equation, Dragt let the scalar potential, ψ, take a complex form. Dragt derives a result in terms of a scalar potential, ψ, that is real; this result has expressions of the generalised gradients that are decomposed into cosine and sine harmonics [31, eq. 15.3.33]. A similar approach is taken by Dragt to decompose the generalised gradients in eq. (3.37) in to cosine and sine components [31, eq 17.3.23]:

$$C^{[n]}_{m,\alpha}(z) = i^n (1/2)^m (1/m!) \int_{-\infty}^{\infty} dk \left[k^{n+m-1}/I_m(kR)\right] \tilde{\tilde{B}}^{\alpha}_{\rho}(R,m,k) \exp(ikz) \ , \quad (3.39)$$

where $m > 0$, and $C^{[n]}_{m,\alpha}$ is either the cosine or sine generalised gradient, $\alpha \in (c,s)$. $\tilde{\tilde{B}}^{\alpha}_{\rho}$ is given by [31, eq 17.3.21]:

$$\tilde{\tilde{B}}^{c}_{\rho}(R,m=0,k) = \frac{1}{2\pi} \int_{-\infty}^{\infty} dz \exp(-ikz) \tilde{B}^{c}_{\rho}(R,m=0,z) \ , \quad (3.40)$$

where [31, eq 17.3.22]:

$$\tilde{B}^{c}_{\rho}(R,m=0,z) = \tilde{B}_{\rho}(R,m=0,z) = \frac{1}{2\pi} \int_{0}^{2\pi} d\phi B_{\rho}(R,\phi,z) \ . \quad (3.41)$$

It should be noted that m corresponds to the multipole harmonic over ϕ. Equation (3.39) provides the generalised gradients for fields with $m > 0$, the monopole (solenoid) fields are given by [31, eq 17.3.24 & 17.3.25]:

$$C^{[n]}_{m=0,s}(z) = 0 \, , \quad (3.42)$$

$$C^{[n]}_{m=0,c}(z) = C^{[n]}_{0}(z) = i^n \int_{-\infty}^{\infty} dk \left[k^{n-1}/I_0(kR)\right] \tilde{\tilde{B}}^{c}_{\rho}(R,m=0,k) \exp(ikz) \ . \quad (3.43)$$

Although Dragt does offer an alternative to generating monopole generalised gradients using the normal component of the cylindrical surface data (eqs. (3.42) and (3.43)), and instead suggests the longitudinal component[31].

It has been established how to generate generalised gradients from cylindrical surface data. The generalised gradients are a generalisation of the multipole description (for which fields are constant in s) to fields that have s-dependence. Therefore the generalised gradients offer a description of a field that is decomposed into its multipole harmonics, as well as its longitudinal harmonics.

Dragt provides expressions of the vector potential in the *azimuthal-free gauge* [31, eq. 15.4.2]:

$$A_{\phi} = 0 \, . \quad (3.44)$$

The azimuthal-free gauge is a gauge transformation for which the azimuthal component is chosen to be 0. Dragt provides the following results for the vector potential [31, eq.15.4.21 - 15.4.26]:

$$A_x^{m,c} = -(1/m)x\,\mathrm{Im}[(x+iy)^m]\sum_{l=0}^{\infty}(-1)^l\frac{m!}{2^{2l}l!(l+m)!}C_{m,c}^{[2l+1]}(z)(x^2+y^2)^l\,, \tag{3.45}$$

$$A_y^{m,c} = -(1/m)y\,\mathrm{Im}[(x+iy)^m]\sum_{l=0}^{\infty}(-1)^l\frac{m!}{2^{2l}l!(l+m)!}C_{m,c}^{[2l+1]}(z)(x^2+y^2)^l\,, \tag{3.46}$$

$$A_z^{m,c} = -(1/m)\,\mathrm{Im}[(x+iy)^m]\sum_{l=0}^{\infty}(-1)^l\frac{(2l+m)m!}{2^{2l}l!(l+m)!}C_{m,c}^{[2l]}(z)(x^2+y^2)^l\,, \tag{3.47}$$

$$A_x^{m,s} = -(1/m)x\,\mathrm{Re}[(x+iy)^m]\sum_{l=0}^{\infty}(-1)^l\frac{m!}{2^{2l}l!(l+m)!}C_{m,s}^{[2l+1]}(z)(x^2+y^2)^l\,, \tag{3.48}$$

$$A_y^{m,s} = -(1/m)y\,\mathrm{Re}[(x+iy)^m]\sum_{l=0}^{\infty}(-1)^l\frac{m!}{2^{2l}l!(l+m)!}C_{m,s}^{[2l+1]}(z)(x^2+y^2)^l\,, \tag{3.49}$$

$$A_z^{m,s} = -(1/m)\,\mathrm{Re}[(x+iy)^m]\sum_{l=0}^{\infty}(-1)^l\frac{(2l+m)m!}{2^{2l}l!(l+m)!}C_{m,s}^{[2l]}(z)(x^2+y^2)^l\,. \tag{3.50}$$

The generalised gradients can be used to describe the fringe field of HL-LHC inner triplet by using a sample of the magnetic field on the surface of a cylinder. It has the property of smoothing such that noise is exponentially damped when reconstructing fields inside the cylinder. The generalised gradients will then allow vector potentials to be calculated for arbitrary points along s. The vector potential can then be used in various integrators to provide transfer maps of the fringe field.

3.1.7 Electromagnetic fields with s-dependence

Fringe fields are not the only fields to exhibit s-dependence. For example, free electron lasers (FELs) make use of repeating configurations of magnets to produce an oscillating path through the magnets for a given particle [3]. This magnet configuration is known as an undulator or a wiggler depending on the wiggler strength K [3].

$$K = C_K B_0 \lambda_p\,, \tag{3.51}$$

where the magnetic field B_0 is in Teslas and λ_p is in centimetres. C_K is a constant:

$$C_K = \frac{ce}{2\pi mc^2} = 0.934\,\mathrm{T}^{-1}\mathrm{cm}^{-1}\,. \tag{3.52}$$

As an aside, a wiggler is for a configuration where $K \gg 1$.

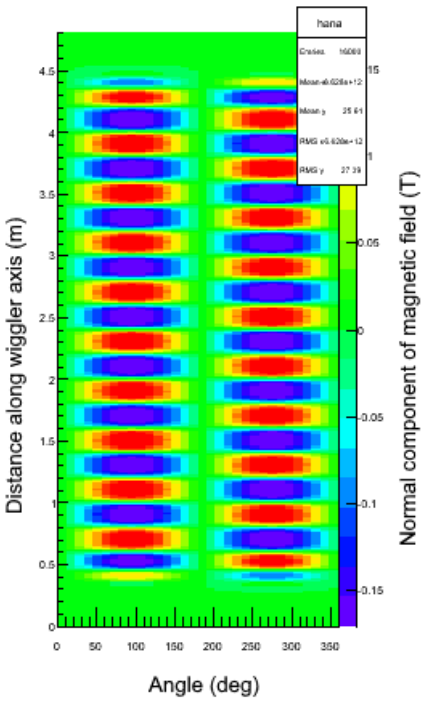

FIGURE 3.7: The normal component of a demonstrative wiggler magnetic field on a circular cylindrical surface.

In fig. 3.7 the s-dependence of the wiggler can be seen. The field is changing with z direction which is collinear with s due to it being a straight line element. Figure 3.7 shows the normal component of the magnetic field on a circular cylinder centred on the longitudinal axis of the accelerator component. The normal component of the field on a cylinder is the first step towards generating generalised gradients. A similar technique is used for the inner triplet HL-LHC magnets in the method chapter (section 4.1.3).

This shows that the generalised gradient method can be used for other fields with s-dependence and not just for quadrupole fringe fields.

3.2 Particle dynamics discussion

In this section the different methods to describe the dynamical nature of particles within an accelerator are presented.

3.2.1 Newtonian mechanics

The method of Newtonian mechanics relies on the Newtonian equation where the force, F, is defined as the change in momentum, p, over time, eq. (3.53), whilst the forces

applied are described by the Lorentz Force in eq. (3.1).

$$F = \frac{dp}{dt} \tag{3.53}$$

$$F_{EM} = q\,(E + v \times B) \tag{3.1 revisited}$$

Solving eq. (3.53) involves integrating with respect to time. This is inconvenient as the positions of electric and magnetic fields in the accelerator are better parametrised in terms of position, instead of time.

The Lagrangian and Hamiltonian can be parametrised with respect to position and therefore each have an advantage over Newtonian formulations.

3.2.2 Lagrangian mechanics

There exists a set of equations known as the Euler-Lagrange equations [3, eq. 1.63 - 1.65]:

$$\frac{\partial L}{\partial q_i} - \frac{d}{dt}\left(\frac{\partial L}{\partial \dot{q}_i}\right) = 0\,, \tag{3.54}$$

where the Lagrangian, $L = L(q_i, \dot{q}_i; t)$, can be any function where q_i and $\dot{q}_i$ are the canonical variables of position and velocity and t is the independent variable time. For the case of the Euler-Lagrange equations the action over a path of motion between two points (t_1 and t_2) is a minimum point.

$$\delta S = \delta \int_{t_0}^{t_1} L(t)dt = 0\,. \tag{3.55}$$

Where δ represents the change resulting from a change in path between the t_1 and t_2, and S is the action.

The Lagrangian can be chosen to suit the problem being solved. For example the simple case of a non-relativistic system without dissipative forces can be represented by [32]:

$$L = T - V\,, \tag{3.56}$$

where T is the kinetic energy of the system and V is the potential energy of the system. The choice of Lagrangian is not unique to the problem; any choice of Lagrangian is valid if it is a solution to the Euler-Lagrange equations. Wiedemann derives the following Lagrangian [3, eq. 1.86]:

$$L = -mc\sqrt{c^2 - \dot{x}^2 - \dot{y}^2 - h^2\dot{z}^2} + e\left(\dot{x}A_x + \dot{y}A_y + h\dot{z}A_z\right) - e\phi\,, \tag{3.57}$$

where [3, eq. 1.85]:

$$h = 1 + \kappa_x x + \kappa_y y\,, \tag{3.58}$$

and x, y, z and $\dot{x}, \dot{y}, \dot{z}$ are the coordinates and velocities using a Frenet-Serret coordinate system. $A_{x,y,z}$ are components of the vector potential of the magnetic field. The Frenet-Serret coordinates are curvilinear. $\kappa_x x$ represents the curvature of the reference trajectory of the particles. The Lagrangian in eq. (3.57) can be used to describe the motion of a charged particle within an electromagnetic field. Wiedemann derives equations of motion from this Lagrangian [3, eqs 2.42 a & b]:

$$x'' \approx \kappa_x h - (1-\delta)\frac{e}{p_0}\left(hB_y - y'B_z\right) + \frac{eE_x}{\gamma m v^2}\,, \tag{3.59}$$

$$y'' \approx \kappa_y h + (1-\delta)\frac{e}{p_0}\left(hB_x - x'B_z\right) + \frac{eE_y}{\gamma m v^2}\,, \tag{3.60}$$

where p_0 is the reference momentum of a particle, and δ is the momentum deviation from the reference momentum. $E_{x,y,z}$ and $B_{x,y,z}$ are the electric and magnetic field respectively. These equations of motions are not symplectic and therefore not suitable for long term tracking. Symplecticity is a guarantee that areas of phase space are conserved when applying a transfer map. If a transfer map is not symplectic then small errors affecting phase space area can grow and lead to incorrect results (see section 3.2.6) [3].

3.2.3 Hamiltonian mechanics

The Hamiltonian can be derived in terms of a suitable Lagrangian:

$$H\left(q_i, p_i\right) = \sum_i \dot{q}_i P_i - L\left(q_i, \dot{q}_i\right)\,, \tag{3.61}$$

where the Hamiltonian is a function $H(x, p; t)$, and x and p are the canonical variables of position and canonical momentum, and t is the independent variable time. Canonical momentum can also be represented in terms of the Lagrangian:

$$p_i = \frac{\partial L}{\partial \dot{q}_i}\,, \tag{3.62}$$

which is to be distinguished from the mechanical momentum mv.

The equations of motions for the Hamiltonian, or Hamilton's equations, are:

$$\frac{dx_i}{dt} = \frac{\partial H}{\partial p_i}\,, \tag{3.63}$$

$$\frac{dp_i}{dt} = -\frac{\partial H}{\partial x_i}\,. \tag{3.64}$$

Compared to the set of second order differential Euler-Lagrange equations, the first order differential Hamilton's equations are less complex to work with and so the Hamiltonian is preferable in that regard [10].

3.2.4 Dynamical variables from a Hamiltonian

The derivation of dynamical variables from a Hamiltonian is given below, as described by Wolski [32]. The Hamiltonian can take the form:

$$H = T + V\,, \tag{3.65}$$

where similar to the Lagrangian, T is the kinetic energy and V is the potential energy of the system. Substituting in expressions for the kinetic energy and potential energy into eq. (3.65) gives:

$$H = \sqrt{(p - qA)^2\, c^2 + m^2 c^4} + q\phi\,, \tag{3.66}$$

where A and ϕ are the vector and scalar potentials of the magnetic field respectively. The electric charge of a test charge inside the field is given by q, and its mass is given by m. The charge travels in the field with a momentum p.

It is useful to use the path length along the accelerator, s, as the independent variable instead of the time, t. This is because magnetic fields and other structures are placed along the lattice at certain path lengths. Therefore it is easier to describe when a particle reaches certain components in terms of path length, s, as opposed to the time, t. Using the principle of least action (eq. (3.55), Wolski derives a choice of canonical variables that provides a description of the motion in terms of path length; these canonical variables are (x, p_x), (y, p_y), $(-t, H)$. Rearranging eq. (3.66) in terms of p_z gives:

$$p_z = \sqrt{\frac{(E - q\phi)^2}{c^2} - m^2 c^2 - (p_x - qA_x)^2 - (p_y - qA_y)^2} + qA_z\,. \tag{3.67}$$

H_1 can then be substituted for $-p_z$ to give:

$$H_1 = -\sqrt{\frac{(E - q\phi)^2}{c^2} - m^2c^2 - (p_x - qA_x)^2 - (p_y - qA_y)^2} - qA_z \,. \tag{3.68}$$

Wolski recommends normalising the momenta with respect to the reference momentum e.g. p_i/P_0. Such a normalisation will also require normalisation of the Hamiltonian too, $\tilde{H} = H_1/P_0$. This will result in the following Hamiltonian represented in terms normalised momenta:

$$\tilde{H} = -\sqrt{\frac{(E - q\phi)^2}{P_0^2c^2} - \frac{m^2c^2}{P_0^2} - (\tilde{p}_x - a_x)^2 - (\tilde{p}_y - a_y)^2} - a_z \,, \tag{3.69}$$

where the normalised vector potential is given by:

$$a = q\frac{A}{P_0} \,. \tag{3.70}$$

Wolski applies a further translation to change the longitudinal momentum, E/P_0, into the energy deviation, δ. An energy deviation, $\delta = 0$, represents a particle that has momentum equal to the reference momentum. The energy deviation is a more convenient description than the longitudinal momentum, which would be close to the speed of light for each particle $E/P_0 = c$. The Hamiltonian in the new coordinates is [32, Lecture 2 eq. 51]:

$$H = \frac{\delta}{\beta_0} - \sqrt{\left(\frac{1}{\beta_0} + \delta - \frac{q\phi}{P_0c}\right)^2 - (p_x - a_x)^2 - (p_y - a_y)^2 - \frac{1}{\beta_0^2\gamma_0^2}} - a_z \,. \tag{3.71}$$

eq. (3.71) describes the motion along a straight reference trajectory, i.e. for straight elements. Bending magnets, e.g. dipoles, have a curved reference trajectory. Wolski derives a Hamiltonian for elements with a curved reference trajectory:

$$H = -(1 + hx)\sqrt{\left(\frac{1}{\beta_0} + \delta - \frac{q\phi}{P_0c}\right)^2 - (p_x - a_x)^2 - (p_y - a_y)^2 - \frac{1}{\beta_0^2\gamma_0^2}} - (1 + hx)\, a_s + \frac{\delta}{\beta_0} \,, \tag{3.72}$$

where curvature is defined as:

$$h = \frac{1}{\rho} \,. \tag{3.73}$$

Hamilton's equations can also be written in terms of s as the independent variable:

$$\frac{dx_i}{ds} = \frac{\partial H}{\partial p_i}\,, \tag{3.74}$$

$$\frac{dp_i}{ds} = -\frac{\partial H}{\partial x_i}\,. \tag{3.75}$$

The Hamiltonian (for straight and curved elements) can now be used to produce symplectic maps. This is will be done by expanding the Hamiltonian to second order in terms of the dynamical variables.

3.2.5 Transfer maps for beamline elements

A transfer map describes how the phase space variables change between an initial point, s_0, and final point, s_1, along a path length, δs. A transfer map can be found using a suitable Hamiltonian and Hamilton's equations. Arbitrary electromagnetic geometries can then be investigated by using the scalar and vector potentials, ϕ and a, of the field with an appropriate Hamiltonian. The following derivations follow those given by Wolski [32].

As an example, applying the field free case, $\phi = 0$ and $a = 0$ to the Hamiltonian in eq. (3.71) gives:

$$H = \frac{\delta}{\beta_0} - \sqrt{\left(\frac{1}{\beta_0} + \delta\right)^2 - (p_x)^2 - (p_y)^2 - \frac{1}{\beta_0^2\gamma_0^2}}\,. \tag{3.76}$$

The Hamiltonian above has no dependence on position, x_i; therefore by Hamilton's equations (eq. (3.75)) there should be no change in the momenta, i.e.:

$$\Delta p_x = 0\,, \tag{3.77}$$

$$\Delta p_y = 0\,, \tag{3.78}$$

$$\Delta \delta = 0\,. \tag{3.79}$$

There is however a dependence on the canonical momenta, p_i. Performing the necessary differentiation to the Hamiltonian results in:

$$\frac{\Delta x}{L} = \frac{p_x}{\sqrt{\left(\frac{1}{\beta_0}+\delta\right)^2 - p_x^2 - p_y^2 - \frac{1}{\beta_0^2\gamma_0^2}}}\,, \tag{3.80}$$

$$\frac{\Delta y}{L} = \frac{p_y}{\sqrt{\left(\frac{1}{\beta_0}+\delta\right)^2 - p_x^2 - p_y^2 - \frac{1}{\beta_0^2\gamma_0^2}}}\,, \tag{3.81}$$

$$\frac{\Delta z}{L} = \frac{1}{\beta_0} - \frac{\frac{1}{\beta_0}+\delta}{\sqrt{\left(\frac{1}{\beta_0}+\delta\right)^2 - p_x^2 - p_y^2 - \frac{1}{\beta_0^2\gamma_0^2}}}\,. \tag{3.82}$$

A Taylor expansion can be applied to the expressions in eqs. (3.80) to (3.82) as long as the canonical momenta is small [32]. Applying the Taylor expansion means that the expressions can then be represented by a matrix, R. The phase space coordinates, $\vec{x}_{s_1}$, at the end of the transfer map, with length L, can be determined by the initial coordinates, $\vec{x}_{s_0}$:

$$\vec{x}_{s_1} = R \cdot \vec{x}_{s_0}\,, \tag{3.83}$$

where $\vec{x}$ is the column vector of coordinates $(x, p_x, y, p_y, z, \delta)$.

The transfer maps given below can also be found in [10]. The transfer map, R, of the drift (after performing a Taylor expansion) is:

$$R_{\text{drift}} = \begin{pmatrix} 1 & L & 0 & 0 & 0 & 0 \\ 0 & 1 & 0 & 0 & 0 & 0 \\ 0 & 0 & 1 & L & 0 & 0 \\ 0 & 0 & 0 & 1 & 0 & 0 \\ 0 & 0 & 0 & 0 & 1 & \frac{L}{\beta_0^2\gamma_0^2} \\ 0 & 0 & 0 & 0 & 0 & 1 \end{pmatrix}. \tag{3.84}$$

Equation (3.85) represents the transfer matrix for a dipole:

$$R_{\text{dipole}} = \begin{pmatrix} \cos\omega L & \frac{\sin\omega L}{\omega} & 0 & 0 & 0 & \frac{1-\cos\omega L}{\omega\beta_0} \\ -\omega\sin\omega L & \cos\omega L & 0 & 0 & 0 & \frac{\sin\omega L}{\beta_0} \\ 0 & 0 & 1 & L & 0 & 0 \\ 0 & 0 & 0 & 1 & 0 & 0 \\ -\frac{\sin\omega L}{\beta_0} & -\frac{1-\cos\omega L}{\omega\beta_0} & 0 & 0 & 1 & \frac{L}{\beta_0^2\gamma_0^2} - \frac{\omega L - \sin\omega L}{\omega\beta_0^2} \\ 0 & 0 & 0 & 0 & 0 & 1 \end{pmatrix}, \tag{3.85}$$

where,

$$\omega = \sqrt{hk_0}\,, \tag{3.86}$$

and h is the curvature, $h = 1/\rho$, and k_0 is the normalised dipole field strength.

Looking at the first row of eq. (3.87) the change in horizontal position is bounded and will decrease by a factor of $\cos\omega L$. Although when considering row three it is evident that the vertical position is unbounded and will increase by a factor of $\cosh\omega L$. Therefore the transfer matrix represented in eq. (3.87) is of a horizontally focusing quadrupole.

Figure 3.3 shows how a quadrupole is focusing in one dimension and then diverging in the other:

$$R_{\text{quadrupole}} = \begin{pmatrix} \cos\omega L & \frac{\sin\omega L}{\omega} & 0 & 0 & 0 & 0 \\ -\omega\sin\omega L & \cos\omega L & 0 & 0 & 0 & 0 \\ 0 & 0 & \cos\omega L & \frac{\sinh\omega L}{\omega} & 0 & 0 \\ 0 & 0 & \omega\sinh\omega L & \cosh\omega L & 0 & 0 \\ 0 & 0 & 0 & 0 & 1 & \frac{L}{\beta_0^2\gamma_0^2} \\ 0 & 0 & 0 & 0 & 0 & 1 \end{pmatrix}. \tag{3.87}$$

The skew quadrupole transfer matrix is represented by:

$$R_{\text{skew quadrupole}} = \begin{pmatrix} \frac{1}{2}(\mathcal{C}+) & \frac{1}{2\omega}(\mathcal{S}+) & \frac{1}{2}(\mathcal{C}-) & \frac{1}{2\omega}(\mathcal{S}-) & 0 & 0 \\ -\frac{\omega}{2}(\mathcal{S}-) & \frac{1}{2}(\mathcal{C}+) & -\frac{\omega}{2}(\mathcal{S}+) & \frac{1}{2}(\mathcal{C}-) & 0 & 0 \\ \frac{1}{2}(\mathcal{C}-) & \frac{1}{2\omega}(\mathcal{S}-) & \frac{1}{2}(\mathcal{C}+) & \frac{1}{2\omega}(\mathcal{S}+) & 0 & 0 \\ -\frac{\omega}{2}(\mathcal{S}+) & \frac{1}{2}(\mathcal{C}-) & -\frac{\omega}{2}(\mathcal{S}-) & \frac{1}{2}(\mathcal{C}+) & 0 & 0 \\ 0 & 0 & 0 & 0 & 1 & \frac{L}{\beta_0^2\gamma_0^2} \\ 0 & 0 & 0 & 0 & 0 & 1 \end{pmatrix}, \tag{3.88}$$

where

$$\omega = \sqrt{k_{1s}}\,, \tag{3.89}$$

and

$$\mathcal{C}\pm = \cos\omega L \pm \cosh\omega L\,, \tag{3.90}$$

$$\mathcal{S}\pm = \sin\omega L \pm \sinh\omega L\,. \tag{3.91}$$

As can be seen in eq. (3.88), the horizontal phase space is affected by both the initial horizontal phase space coordinates but also the vertical phase space coordinates. This is known as coupling, which means that the horizontal and vertical motion are interdependent.

In the theory of chromaticity section (section 3.2.9), equations of motion in the horizontal phase space of a quadrupole with chromaticity is taken into account is given.

3.2.6 Symplecticity

Hamiltonian systems are symplectic. That is to say that a transfer map, S, between any two points are symplectic if [32]:

$$J^T S J = S\,, \tag{3.92}$$

where J is the Jacobian matrix. The physical importance of a symplectic transformation is that phase space area is conserved under the transformation.

3.2.7 The FODO lattice

A *FODO lattice* is a periodic lattice which produces *strong focusing* of the beam. This section will show how the FODO exhibits strong focusing, which is the focusing of the beam in both transverse planes. Many accelerators require a beam to be constrained, and therefore make use of the FODO lattice. First the details of the FODO lattice will be introduced, and then the dynamics of the lattice will be discussed.

The FODO lattice is so called due to its construction and elements. The unit cell consists of a focusing (F) quadrupole, a defocusing (D) quadrupole, and two drifts (O) that separate the quadrupoles.

The linear matrices for quadrupoles and drifts have already been shown in eq. (3.87) and eq. (3.84). It is common to analyse the FODO in the thin-lens approximation due to the simplification it offers whilst maintaining the dynamical properties of the FODO [3]. As part of the thin-lens approximation, the finite length of the quadrupoles is taken in the limit to zero:

$$L \to 0\,. \tag{3.93}$$

In addition, the product of the length of the quadrupole and the gradient of the quadrupole has a finite limit:

$$kL \to \frac{1}{f}\,, \tag{3.94}$$

where k is the normalised gradient, and L is the drift length.

These limits result in the following transfer matrix for the focusing (F) quadrupole:

$$R_{\mathrm{F}} = \begin{pmatrix} 1 & 0 & 0 & 0 & 0 & 0 \\ -1/f & 1 & 0 & 0 & 0 & 0 \\ 0 & 0 & 1 & 0 & 0 & 0 \\ 0 & 0 & 1/f & 1 & 0 & 0 \\ 0 & 0 & 0 & 0 & 1 & 0 \\ 0 & 0 & 0 & 0 & 0 & 1 \end{pmatrix}. \tag{3.95}$$

The defocusing (D) thin lens quadrupole is defined similarly in the limit to eq. (3.95), but the focal length f is negated, e.g. $f = -f_{\mathrm{F}}$.

The transfer matrix for the FODO can then be computed by composition of the transfer matrices of the individual elements. There is a choice of unit cell, which commonly is defined from the middle of the focusing quadrupole or from the edge entering the focusing quadrupole. Using the transfer matrix for the drift from eq. (3.84), which will be referred to here as R_{O}, will give the following transfer matrix for unit cell with a boundary at the start of the focusing quadrupole,

$$R_{\mathrm{FODO}} = R_{\mathrm{O}} R_{\mathrm{D}} R_{\mathrm{O}} R_{\mathrm{F}}\,. \tag{3.96}$$

For the unit cell with a boundary in the middle of the focusing quadrupole a transfer function representing traversal through half the quadrupole can be represented by $R_{\mathrm{F}/2}$, with focal length $f = f_{\mathrm{F}}/2$. The transfer matrix of this FODO is represented by:

$$R_{\mathrm{FODO}} = R_{\mathrm{F}/2} R_{\mathrm{O}} R_{\mathrm{D}} R_{\mathrm{O}} R_{\mathrm{F}/2}\,. \tag{3.97}$$

As there is no coupling in the transfer matrices, the matrix composition can be evaluated in the horizontal, vertical, and longitudinal dynamics separately.

In the case for the FODO beginning at the entrance of the focusing quadrupole [10, Eq 4.10 - 4.12]:

$$R_{\mathrm{horizontal}} = \begin{pmatrix} 1 - \frac{L}{f} - \frac{L^2}{f^2} & 2L + \frac{L^2}{f} \\ \frac{-L}{f^2} & 1 + \frac{L}{f} \end{pmatrix}. \tag{3.98}$$

$$R_{\text{vertical}} = \begin{pmatrix} 1 + \frac{L}{f} - \frac{L^2}{f^2} & 2L - \frac{L^2}{f} \\ \frac{-L}{f^2} & 1 - \frac{L}{f} \end{pmatrix} . \tag{3.99}$$

$$R_{\text{longitundinal}} = \begin{pmatrix} 1 & \frac{2L}{{\beta_0}^2 {\gamma_0}^2} \\ 0 & 1 \end{pmatrix} . \tag{3.100}$$

Whereas in the case for the FODO with the unit cell starting halfway through the focusing quadrupole [32, Lecture 6, eq 7]:

$$R_{\text{horizontal}} = \begin{pmatrix} 1 - \frac{L^2}{2{f_0}^2} & \frac{L}{f_0}\left(L + 2f_0\right) \\ \frac{L}{4{f_0}^3}\left(L - 2f_0\right) & 1 - \frac{L^2}{2{f_0}^2} \end{pmatrix} . \tag{3.101}$$

$$R_{\text{vertical}} = \begin{pmatrix} 1 - \frac{L^2}{2{f_0}^2} & -\frac{L}{f_0}\left(L - 2f_0\right) \\ -\frac{L}{4{f_0}^3}\left(L + 2f_0\right) & 1 - \frac{L^2}{2{f_0}^2} \end{pmatrix} . \tag{3.102}$$

As can be seen in eqs. (3.98) and (3.99) the transfer matrix is focusing in both horizontal and vertical planes. This focusing in both planes is also known as strong focusing.

If a particle is given a horizontal deviation from the closed orbit (which for the FODO is the magnet longitudinal axis) and then simulated traversing the FODO multiple times whilst recording the variables of the particle at each complete traversal of the FODO unit cell, then it would result in fig. 3.8.

The particle when tracked through complete iterations of the unit cell, traces out an ellipse in phase space. An ellipse would be impossible if there was energy lost to friction, instead a spiral would be produced in that case. This shows that in the model of the FODO developed here is frictionless. Furthermore this is another confirmation that the matrices described to track through a FODO lattice are symplectic.

3.2.8 Courant-Snyder parameters

The derivation of the Courant-Snyder parameters shown below is based on [10] and [32].

When the transfer matrices are solutions to Hamilton's equations, then they are symplectic. A combination of symplectic matrices are also symplectic. The symplecticity condition (eq. (3.92)) has a general solution; the portion of an uncoupled symplectic matrix for horizontal motion, R_2, can be described as:

$$R_2 = I_2 \cos\mu_x + S_2 \cdot A_x \sin\mu_x \,, \tag{3.103}$$

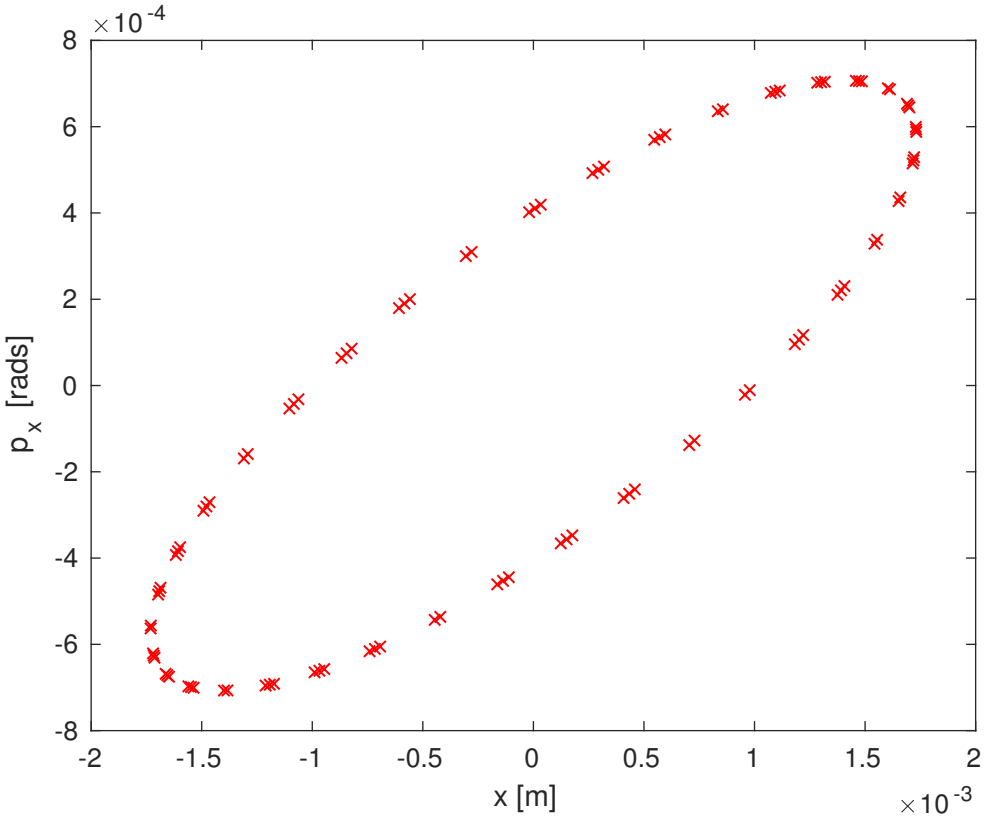

FIGURE 3.8: The phase space results of tracking a particle, with a horizontal deviation from the closed orbit, through a FODO cell. The coordinates at each pass through the FODO cell are plotted.

where I_2 is the 2 x 2 identity matrix, μ is a parameter, and A_x is a 2 x 2 symmetric matrix. S_2 is the antisymmetric matrix:

$$S_2 = \begin{pmatrix} 0 & 1 \\ -1 & 0 \end{pmatrix} . \tag{3.104}$$

As A_x is 2 x 2 symmetric matrix, it is therefore defined in terms of three unique parameters. These parameters are given in eq. (3.105):

$$A_x = \begin{pmatrix} \gamma_x & \alpha_x \\ \alpha_x & \beta_x \end{pmatrix} , \tag{3.105}$$

where γ_x, β_x, and α_x are known as the Courant-Snyder parameters (or also the Twiss parameters). The subscript denotes that they are properties associated with horizontal phase space, and a similar set can be derived for vertical phase space.

From eqs. (3.103) and (3.105) it is possible to write R_x as:

$$R_x = \begin{pmatrix} \cos\mu_x + \alpha_x \sin\mu_x & \beta_x \sin\mu_x \\ -\gamma_x \sin\mu_x & \cos\mu_x - \alpha_x \sin\mu_x \end{pmatrix} . \tag{3.106}$$

The Courant-Snyder parameters and the phase advance can be determined by the four parameters of the transfer matrix R_x [10, page 134]. From eq. (3.106) the parameter μ_x (the phase advance) can be obtained from the trace of the R_x matrix.

$$\mathrm{Tr}R_x = 2\cos\mu_x \,. \tag{3.107}$$

Firstly it is important to observe that the transfer map R_F of the FODO is dependent on the starting position within the FODO, eqs. (3.98) and (3.101). Therefore the choice of starting position will also influence the Courant-Snyder parameters.

It has been established already that the FODO matrix is symplectic. The symplectic condition, eq. (3.92), results in:

$$R_2^T \cdot S_2 \cdot R_2 = S_2 \,. \tag{3.108}$$

Equation (3.108) is only valid when:

$$\beta_x\gamma_x - \alpha_x^2 = 1 \,. \tag{3.109}$$

If the transfer matrix is considered from a different starting point within the FODO, such as after the focusing quadrupole, this point will be called s_1 to distinguish it from conventional starting point s_0, this would result in the following expression:

$$R\left(s_1\right) = R_\mathrm{F}R_\mathrm{O}R_\mathrm{D}R_\mathrm{O} = R_\mathrm{F}R\left(s_0\right)R_\mathrm{F}^{-1} \,. \tag{3.110}$$

For now it is assumed that the parameter μ_x is constant with respect to the starting position chosen. Whether this is a reasonable assumption will become evident later. If μ_x is constant then the change in R_x is determined by S_2 and A_x, therefore:

$$S_2A_x\left(s_1\right) = R_{\mathrm{F}x}S_2A_x\left(s_0\right)R_{\mathrm{F}x}^{-1} \,, \tag{3.111}$$

The result is:

$$A_x\left(s_1\right) = S_2^{-1}R_{\mathrm{F}x}S_2A_x\left(s_0\right)R_{\mathrm{F}x}^{-1} \,, \tag{3.112}$$

where $R_{\mathrm{F}x}$ is the horizontally focusing part of the transfer matrix of a FODO focusing quadrupole R_{F}. It should be noted that $R_{\mathrm{F}x}$ is also symplectic given that the focusing quadrupole is symplectic and its transfer matrix is block diagonal [32]. Therefore using eq. (3.108):

$$S_2^{-1} R_{\mathrm{F}x}^{\mathrm{T}} S_2 = R_{\mathrm{F}x}^{-1} \,. \tag{3.113}$$

Using the rules for transposing matrices, $A^{\mathrm{T}} B^{\mathrm{T}} = (BA)^{\mathrm{T}}$, as well as the result that S_2 is a skew-symmetric matrix and therefore also an orthogonal matrix and so $S_2^{\mathrm{T}} = S_2^{-1}$, then:

$$S_2^{-1} R_{\mathrm{F}x} S_2 = \left(R_{\mathrm{F}x}^{\mathrm{T}}\right)^{-1} \,. \tag{3.114}$$

Using this result in eq. (3.112) gives:

$$A_x\left(s_1\right) = \left(R_{\mathrm{F}x}^{\mathrm{T}}\right)^{-1} A_x\left(s_0\right) R_{\mathrm{F}x}^{-1} \,. \tag{3.115}$$

The Courant-Snyder parameters at different points in a lattice can be calculated if there are respective transfer matrices to those different points. This is due to the following result:

$$A_x\left(s_1\right)^{-1} = R_x\left(s_1, s_0\right) A_x\left(s_0\right)^{-1} R_x\left(s_1, s_0\right)^{\mathrm{T}} \,, \tag{3.116}$$

where $A_x\left(s_1\right)^{-1}$ and $A_x\left(s_0\right)^{-1}$ are the inverse A_x matrices at points s_0 and s_1. $R_x\left(s_1, s_0\right)$ is a transfer matrix describing the motion from s_0 to s_1. Like A_x, A_x^{-1} is also given in terms of the Courant-Snyder parameters - therefore if the Courant-Snyder parameters are known at some starting position s_0, and transfer matrices to some other point s_1 are known then it is possible to calculate the Courant-Snyder parameters at that point.

Using eq. (3.115), an invariant to application of transfer matrix, R, can be constructed:

$$J_x = \frac{1}{2} \begin{pmatrix} x & p_x \end{pmatrix} A_x \begin{pmatrix} x \\ p_x \end{pmatrix} \,. \tag{3.117}$$

A_x changes as shown in eq. (3.115), and the phase space coordinates evolve like:

$$\begin{pmatrix} x \\ p_x \end{pmatrix} \mapsto R \begin{pmatrix} x \\ p_x \end{pmatrix} \,. \tag{3.118}$$

Wolski shows that eq. (3.117) results in the following:

$$J_x = \frac{1}{2}\left(\gamma_x x^2 + 2\alpha_x x p_x + \beta_x p_x^2\right) . \tag{3.119}$$

The invariant is known as the action of a particle, J, and is defined by the Courant-Snyder parameters. It is invariant under transport along the beam line. The Courant-Snyder parameters are determined by a periodic cell of a beamline, and therefore are representative of the beamline rather than of a single particle [32]. The phase space coordinates in eq. (3.119) can be the phase space coordinates of a particle within the lattice. The action can then be calculated for that particle. Plotting eq. (3.119) gives fig. 3.9.

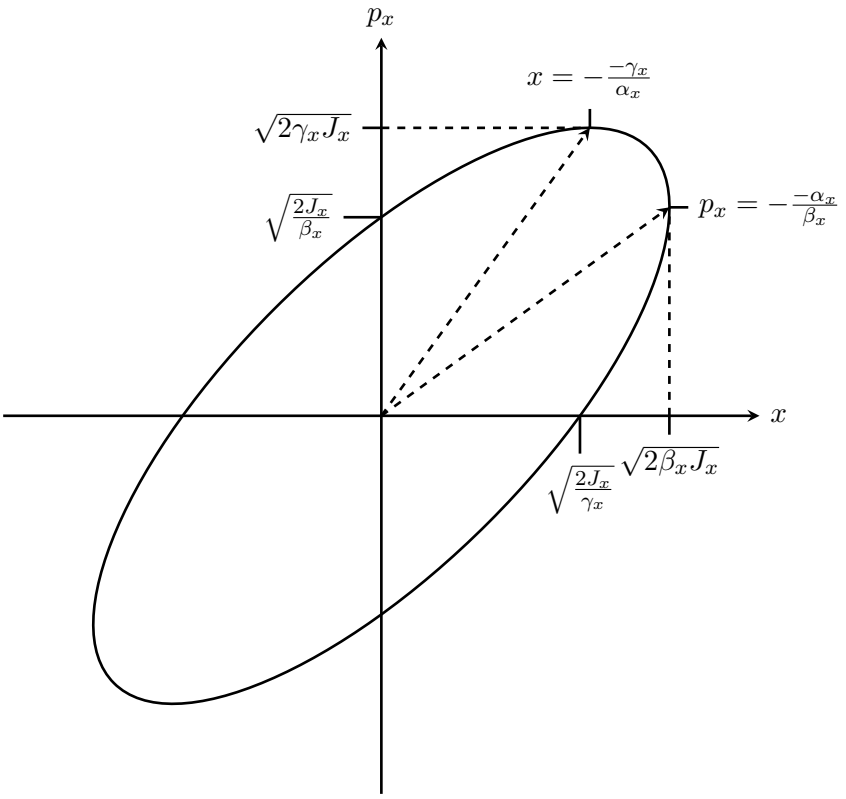

FIGURE 3.9: A horizontal phase space ellipse for a given action J_x, and its features in relation to Courant-Snyder parameters α_x, β_x, and γ_x.

Figure 3.9 shows the dimensions of a phase space ellipse for a given action. The area of the ellipse is $2\pi J_x$. Notice that the tracking through the FODO also resulted in an ellipse fig. 3.8. It is now clear why this should be the case for the FODO. Every traversal of the FODO represents a new set of phase space coordinates, and due to them sharing the same action, they must lie on points traced by the ellipse.

To describe a set of phase space coordinates of a given action, it can be determined by ϕ the angle made between the position on the ellipse and the positive horizontal axis.

This angle is in fact defined in terms of Courant-Snyder parameters and phase space coordinates:

$$\tan\phi_x = -\beta_x \frac{p_x}{x} - \alpha_x \,. \tag{3.120}$$

Equations (3.119) and (3.120) provide the following expression for the horizontal phase coordinates.

$$x = \sqrt{2\beta_x J_x}\cos\phi_x \,, \tag{3.121}$$

$$p_x = -\sqrt{\frac{2J_x}{\beta_x}}\left(\sin\phi_x + \alpha_x\cos\phi_x\right) \,. \tag{3.122}$$

From eq. (3.121) it can be seen that the position depends on both the action and angle, but crucially also the β function. This is significant because the action is constant so β determines the extent of amplitude of a particle with a given action. Additionally it is important to note that the position is also dependent on the angle, but crucially the possible amplitude is set by the β function and as the Courant-Snyder parameters describe the lattice, this means that the amplitude of the particle is periodic with the lattice [32]. The angle increases around the lattice as $\frac{d\phi_x}{ds} = \frac{1}{\beta_x}$.

The Courant-Snyder parameters for a FODO cell are given in [10, eqs. 4.68 - 4.70]. These can be plotted in fig. 3.10.

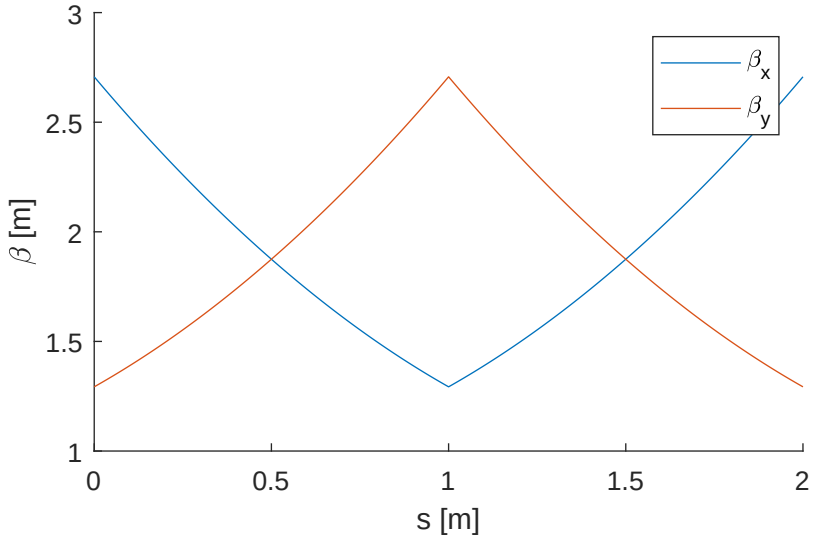

FIGURE 3.10: The beta function calculated when tracking through a FODO cell, with drift length, $L = 1\,\text{m}$ and focusing strength $f = \sqrt{2}\text{m}$.

The β functions in a FODO (fig. 3.10) alternate between: reaching their smallest extent at the defocusing magnet, and reaching their largest extent at the focusing magnet.

Despite the fact that quadrupole focus and defocus in different planes, the FODO is able to keep both planes bounded.

A particle's action is invariant (eq. (3.119)); therefore at points in the lattice with smaller beam sizes (small β), the particle must have a larger transverse momentum. This concept is important to consider when thinking about the small β values that are required within the HL-LHC to achieve the luminosities at the collision points.

3.2.9 Chromaticity

Chromaticity is the change of tune with respect to the energy of a particle. It is due to differences in focusing strength with respect to the energy of a particle. A transfer matrix for a quadrupole has already been discussed in section 3.2.5, but there the treatment was made using a paraxial approximation of the Hamiltonian. This resulted in the loss of terms higher than second order, such as the chromatic effect, which is an important nonlinear effect.

Wolski gives the equations of the transverse phase space coordinates after transport in a quadrupole, taking into account chromaticity [10]. This is achieved by considering the transverse phase space separately from the longitudinal phase space. The equations are as follows:

$$x(L) = \cos(\omega' L)x(0) + \frac{\sin(\omega' L)}{\omega' D}p_x(0)\,, \tag{3.123}$$

$$p_x(L) = -\,\omega' D \sin(\omega' L)x(0) + \cos(\omega' L)p_x(0)\,, \tag{3.124}$$

$$y(L) = \cosh(\omega' L)y(0) + \frac{\sinh(\omega' L)}{\omega' D}p_y(0)\,, \tag{3.125}$$

$$p_y(L) = \omega' D \sinh(\omega' L)x(0) + \cosh(\omega' L)p_y(0)\,, \tag{3.126}$$

where

$$D = \sqrt{1 + \frac{2\delta}{\beta_0} + \delta^2}\,, \tag{3.127}$$

and

$$\omega' = \sqrt{\frac{k_1}{D}}\,. \tag{3.128}$$

Chromaticity of a FODO

The treatment of the FODO lattice can also be extended to consider chromaticity. This is useful because the FODO lattice is used across lattice designs due to its property of strong focusing. The horizontal chromaticity, ξ_x of a FODO depends on the phase advance over the lattice μ_x:

$$\xi_x = -\frac{1}{\pi}\tan\left(\frac{\mu_x}{2}\right) . \tag{3.129}$$

Chromaticity in a storage ring

Quadrupoles and dipoles introduce negative chromaticity to a storage ring. Wolski states that for storage rings with high currents it can be necessary for beam stability to maintain a zero or even slightly positive chromaticity [10]. Therefore to keep the chromaticity as close to zero as possible, it is sometimes desirable to reduce beta functions and quadrupole strengths as required. This option is not compatible with the design requirements of colliders, such as the HL-LHC, which require high strength quadrupoles placed at areas of the ring with large beta functions.

On the other hand, sextupoles can be used to correct the chromaticity without having a large impact on the linear dynamics, such as the closed orbit, the beta functions, and dispersion [10]. The Hamiltonian for a sextupole is defined below:

$$H = \frac{\delta}{\beta_0} - \sqrt{\left(\frac{1}{\beta_0} + \delta - \frac{q\phi}{P_0 c}\right)^2 - (p_x - a_x)^2 - (p_y - a_y)^2 - \frac{1}{\beta_0^2\gamma_0^2}} + \frac{1}{6}k_2\left(x^3 - 3xy^2\right) , \tag{3.130}$$

where

$$a = \frac{q}{P_0} = \left(0, 0, -\frac{1}{6}k_2\left(x^3 - 3xy^2\right)\right) , \tag{3.131}$$

a, is the vector potential of the sextupole with the magnetic axis along $x = y = 0$.

Sextupoles are used to add positive contributions to the chromaticity. But sextupoles are also constrained to have inverse effects on the horizontal and vertical chromaticities. For example, a sextupole that increases the horizontal chromaticity must also decrease the vertical chromaticity. It is possible overall to add positive chromaticity in both planes by placing sextupoles in locations where their positive contribution in one dimension outweighs the negative contribution in the other. For example, sextupoles with positive strength at locations where $\beta_x > \beta_y$ can be combined with sextupoles with negatives

strengths at locations where $\beta_y > \beta_x$ (assuming there is also positive horizontal dispersion, η_x).

Chromaticity is tuned to zero or close to zero so that the range of tunes of particles in a bunch is minimised. There is also a term known as the head tail instability which means that a positive chromaticity is needed for beam stability in a storage ring running above transition [10].

Sextupoles have nonlinear effects on the beam which can be undesirable for beam stability. For example, sextupoles have geometric effects and chromatic effects. This means that they affect the particles with zero and non-zero energy deviations respectively. Wolski notes that the geometric effects can be effectively cancelled by pairing sextupoles that are separated by a distance corresponding with a $-I$ transformation. When the sextupoles are separated in this way it results in a better dynamic aperture [10].

3.2.10 Tracking with many particles

In the Courant-Snyder parameter section only single particles were considered. Accelerators usually contain many particles, such at the HL-LHC which is designed to have up to 2.2×10^{11} particles per bunch.

How might it be possible to describe the dynamics of such a large amount of particles in a bunch? It is easier to consider the averages of phase space coordinates. For example $\langle x \rangle$ is the average horizontal position for all the particles in the bunch. These averages when performed on the six dynamical variables $(x, p_x, y, p_y, z, \delta)$ are known as first order moments of the bunch distribution. The collection of first order moments are known as the bunch centroid. The tracking of many particles is considered below as described by Wolski [32] [10].

As stated in the Courant-Snyder section (section 3.2.8) they are a property of the beamline and not the beam. Restating another concept established in that section, the Courant-Snyder parameters can be found at the point representing the beginning of a periodic transfer matrix. Not all beamlines are periodic and so it follows that this technique does not apply for all beamlines. It is possible to choose the parameters arbitrarily but the β and α functions will not exhibit the same periodicity as the lattice unless the previous technique is used.

There is a technique to generate the Courant-Snyder parameters from the beam itself. Specifically the many particle distributions in position and momentum-space can used to determine the parameters.

For example the first order moment of the x^2 parameter, using eq. (3.121), is:

$$\langle x^2 \rangle = 2\beta_x \langle J_x \cos^2 \phi_x \rangle \,. \tag{3.132}$$

If it can be assumed that the angle variables of the particles are equally distributed, then eq. (3.132) can be simplified to:

$$\langle x^2 \rangle = \beta_x \langle J_x \rangle \,. \tag{3.133}$$

This leads to the definition of a useful property of the bunch, the horizontal emittance ϵ_x:

$$\epsilon_x = \langle J_x \rangle \,. \tag{3.134}$$

It then follows that eq. (3.133) becomes:

$$\langle x^2 \rangle = \beta_x \epsilon_x \,. \tag{3.135}$$

Using eqs. (3.121) and (3.122) similar results can be found for other averages to second order:

$$\langle x p_x \rangle = -\alpha_x \epsilon_x \,, \tag{3.136}$$

$$\langle p_x^2 \rangle = \gamma_x \epsilon_x \,. \tag{3.137}$$

Each of these averages to second order are in terms of the Courant-Snyder parameters. Using these results in combination with eq. (3.109) it follows that:

$$\epsilon_x = \sqrt{\langle x^2 \rangle \langle p_x^2 \rangle - \langle x p_x \rangle^2} \,. \tag{3.138}$$

Equation (3.138) is an important result because it means that if the beam distribution is well known at some point in the lattice, then the emittance can be computed. Other Courant-Snyder parameters can be calculated if the emittance is known. The Courant-Snyder parameters can then be calculated at different points around the beamline by applying symplectic transfer matrices to those points (as seen in section 3.2.8). As the transfer matrices are symplectic, then the action will be an invariant and therefore so will the emittance. Therefore the Courant-Snyder parameters describe the properties of the beam. It is only if the Courant-Snyder parameters are chosen to be equal to the values derived from a periodic cell of the lattice, that the Courant-Snyder parameters will exhibit the same periodicity as the lattice. This result is known as beam matching.

If the Courant-Snyder parameters are different from the values from a periodic cell, then this results in a beam oscillating with a different periodicity to that of the beamline. Such behaviour is known as beta-beating [10].

The second order moments describe the size of the bunch.

$$\Sigma_{ij} = \langle (x_i - \langle x_i \rangle)(x_j - \langle x_j \rangle) \rangle = \langle x_i x_j \rangle - \langle x_i \rangle \langle x_j \rangle \tag{3.139}$$

Swapping the i and j parameters in Σ_{ij} will result in the same result. Therefore Σ_{ij} can be represented as a symmetric matrix, Σ. The components lying along the diagonal of the matrix, i.e. $i = j$, are the variances of the dynamical variables for all particles in a bunch:

$$\Sigma_{11} = \langle x^2 \rangle - \langle x \rangle^2 = \sigma_x^2 \tag{3.140}$$

When working with a single particle approach for the Courant-Snyder variables, it was seen that an invariant, the action J, could be constructed to simplify the description of the amplitude of the oscillation of the particles. Furthermore, because the action was invariant under symplectic transport, it led to assumptions to do with phase space area. A similar approach can be taken when it comes to the second order moments. It turns out this invariant description gives the eigenvalues of ΣS. This can be shown by putting the invariant description through symplectic transport $R(s_0, s_1)$ between s_0 and s_1:

$$\Sigma S \mapsto R \Sigma R^{\mathrm{T}} S = R \Sigma S R^{-1} \,. \tag{3.141}$$

For eq. (3.141) the result of the second order moments under symplectic transport, R, is needed:

$$\left(\langle x_i x_j \rangle - \langle x_i \rangle \langle x_j \rangle \right)_{s_1} = \sum_{i',j'=1}^{6} R_{ii'} R_{jj'} \left(\langle x_{i'} x_{j'} \rangle - \langle x_{i'} \rangle \langle x_{j'} \rangle \right)_{s_0} \,, \tag{3.142}$$

which when written in matrix form is:

$$\Sigma(s_1) = R \Sigma(s_0) R^{\mathrm{T}} \,. \tag{3.143}$$

Looking back to eq. (3.141), ΣS maps to $R \Sigma S R^{-1}$. Why is this result important? Wolski makes the observation that "for any matrices M and N, the eigenvalues of NMN^{-1} are the same as the eigenvalues of M" [32, Lecture 8 p. 10]. Thus it is clear that from this result it must be that the eigenvalues of ΣS are invariant under symplectic transport.

The horizontal emittance represented by the eigenvalues of horizontal portion of the uncoupled ΣS are conserved. The vertical and longitudinal emittances are similarly conserved. These emittances ϵ_k and eigenvalues are related as follows:

$$\lambda_{\pm} = \pm i\epsilon_k \,, \tag{3.144}$$

where $k \in x, y, \delta$ to represent the horizontal, vertical, and longitudinal degrees of freedom respectively.

3.2.11 Coupled optics

A bunch distribution is uncoupled if it has no non-zero second order moments mixing variables from different degrees of freedom. An uncoupled bunch distribution will remain uncoupled under uncoupled transport. However Wolski states that the effect of coupling in a beamline will introduce coupling into a previously uncoupled bunch distribution [32, Lecture 8 pg. 8]. A coupled bunch distribution will have non-zero off-diagonal elements in the Σ describing its second order moments.

Coupled optics are relevant to this work because SAMM uses coupled optics formalisms[3] to calculate the Courant-Snyder parameters of a lattice. To do this, a transfer matrix for one periodic cell is needed. This can be generated by applying each transfer matrix of a HL-LHC component in turn to the identity matrix multiplied by a small value to keep the transport mostly dominated by linear effects. If the closed orbit does not lie along the coordinate axis, then the identity matrix in fact has the starting closed orbit variables added to each column. The matched distribution can be found as described in Wolski [32]. If both the transfer matrix and the matched distribution are known, then the eigenvalues and eigenvectors of the transfer matrix can be found. The eigenvalues, $\exp(\pm i\mu_k)$, are the phase advances across a single periodic cell in each degree of freedom k. From Wolski, "The eigenvectors may be used to construct coupled lattice functions B^k for coupled optics, which relate the sigma matrix directly to the bunch emittances" [32, Lecture 9 pg. 36]. In SAMM, the Courant-Snyder variables are taken from the coupled lattice functions B^k.

3.2.12 Tune shift with amplitude and frequency map analysis

Tune shift with amplitude is an example of a technique that can be used to analyse the behaviour of particles in a complicated beamline environment. It is so named because it is the change in tune for particles with some amplitude away from the closed orbit.

[3] Using the ComputeMatchedTwiss function.

Tune shift with amplitude is a nonlinear effect, which can be produced by sextupoles and higher order multipole magnets. Dipoles and quadrupoles can have field errors that would result in higher order fields; therefore these magnets can also contribute to the tune shift with amplitude [10].

Tune shift with amplitude can be explained by starting with an simple model. Beginning with the Hamiltonian represented in terms of action as:

$$H = aJ + bJ^2 \,, \tag{3.145}$$

where a and b are constants. The equations of motion in terms of action and angle give the following result [10, eq. 11.28]:

$$\frac{d\phi}{ds} = \frac{dH}{dJ} = a + 2bJ \,. \tag{3.146}$$

Such a result shows that the phase advance would increase depending on the b factor. As the tune is the phase advance over one complete turn, it shows how the tune can be dependent on the action of a particle, J.

If the Hamiltonian was dependent on higher order terms in action, e.g. J^3, J^4, etc, then the tune shift with amplitude will have a more complicated relationship to the action.

Betatron tune shift with amplitude can be approximated using perturbation theory or normal form analysis. Both techniques aim to transform the Hamiltonian into a simpler form so that it is possible to estimate the tune shift with amplitude from the simplified Hamiltonian.

An example of how perturbation theory is used to calculate the tune shift with amplitude due to a sextupole is given by Wolski[10, eq. 11.174].

Extending eq. (3.146) to the x-y plane gives:

$$H = a_x J_x + a_y J_y + b_{xx} J_x^2 + b_{xy} J_x J_y + b_{yy} Jy^2 \,, \tag{3.147}$$

where $a_{x,y}$ and $b_{x,y}$ are constants.

$$\frac{d\phi_x}{ds} = a_x + 2b_{xx} J_x + b_{xy} J_y \,, \tag{3.148}$$

$$\frac{d\phi_y}{ds} = a_y + 2b_{yy} J_y + b_{xy} J_x \,. \tag{3.149}$$

Frequency map analysis is based on a two dimensional tune shift with amplitude. When the particles with different amplitudes are plotted in tune space, the particles are observed to be spread across the tune grid according to their tune shift. One corner of the plot in tune space is represented by particles close to the closed orbit, and the rest of the particles are spread out. The shape and size of the particles spread over tune space is dependent on the tune shift with amplitude and therefore the constants in eq. (3.146).

A Hamiltonian that depends on action as well as angle will have terms that drive resonances. Resonances can have different effects, some of which can be complicated. For example, particles close to a resonance can experience chaotic or unstable motion, which can lead to the loss of the particle in the accelerator. These effects can be studied using perturbation theory or normal form analysis.

The nominal working point of the accelerator, the tune of particles on the closed orbit, might be chosen so that it does not cross the stronger resonances due to their potentially detrimental effects. But tune shift with amplitude can mean that some particles will have their tunes close to a resonance. A resonance can then have the effect of drawing the particle onto the resonance (by changing the tune of the particle). This can be seen in frequency map analysis plots with particles lying on or close to resonance lines.

As stated before, octupoles can also affect the tune shift with amplitude. In particular they can be used to make sure that certain problematic resonances are avoided by modifying the tune shift with amplitude accordingly.

But using this method is not trivial. Optimising the dynamic aperture by changing the tune shift of octupoles and other components is an iterative process, which can take time. This is because the components can drive resonances themselves.

3.2.13 Dynamic aperture

Particles beyond a limit, known as the dynamic aperture, are usually lost - which is to say that they are no longer bound. The dynamic aperture is related to the nonlinear properties of a lattice. This is because the amplitudes reached when modelling linear motion are usually smaller than nonlinear motion.

The dynamic aperture calculation is carried using long term turn-by-turn tracking. Therefore it is important to use symplectic maps to do this tracking.

3.3 Numeric integration methods

In this section the theory behind the two integration methods, Wu-Forest-Robin and Implicit Runge-Kutta methods, used for the study will be discussed.

A key property of an integration method, that is important in long-term tracking studies in particular, is whether the transfer maps produced are symplectic. As seen in section 3.2.8, the action is invariant under symplectic transport. This is not the case for a non symplectic map. Therefore a non symplectic map can see the growth or damping of betatron oscillations due to the growth or damping of the action variable.

For the Wu-Forest-Robin integration, one powerful technique involves the use of Lie transformations. They are useful for algebraic manipulation and analysis, but they do not allow for convenient evaluation. A more convenient way to evaluate is to use a transfer map expressed as a power series; this evaluation is also computationally fast to calculate. The power series formulation is explicit, which means that the map does not require an an iterative solution to be performed based on the dynamical variables of the particle. Although the representation of a real accelerator component requires an infinite number of terms. Therefore the map must be truncated at some point and the resulting truncated power series will not be symplectic. Another property that will be seen of Wu-Forest-Robin integration is that it requires the paraxial approximation ($|p_x|, |p_y| \ll 1$).

The Runge-Kutta methods as an integration scheme can be either implicit or explicit. Explicit Runge-Kutta schemes are not symplectic [10, p. 327]. There is a simple scheme known as the implicit midpoint method which is symplectic. Being implicit requires algebraic manipulation at each integration step and is therefore computationally slow. The Runge-Kutta does not require the paraxial approximation and therefore might be a useful scheme for modelling particles that have high transverse momentums. The HL-LHC inner triplet focusing quadrupole sections are an interesting benchmark to test this assumption.

3.3.1 Wu-Forest-Robin

An integration technique devised by Wu, Forest, and Robin [33] allows for symplectic integration of s-dependent fields. This description of the Wu-Forest-Robin in this chapter is based on the following citations: [10] [34] [33]. The integration is explicit, meaning that the map can be applied to dynamical variables without first manipulating them.

It was seen in section 3.2.3 that it is possible to construct a Hamiltonian for straight line elements:

$$H = \frac{\delta}{\beta_0} - \sqrt{\left(\frac{1}{\beta_0} + \delta - \frac{q\phi}{P_0 c}\right)^2 - (p_x - a_x)^2 - (p_y - a_y)^2 - \frac{1}{\beta_0^2\gamma_0^2}} - a_z\,. \quad \text{(3.71 revisited)}$$

If the Hamiltonian in eq. (3.71) is independent between 0 and s, then a transfer map can be expressed in terms of Lie transformations:

$$f(s) = e^{-s:H:} f(0)\,, \tag{3.150}$$

where $:H:$ is the Lie operator applied to the Hamiltonian. The Lie operator $:g:$ for an arbitrary function $g(x_i, p_i)$, depending on phase space coordinates x_i, p_i with degrees of freedom $i = 1 \cdots n$, is given by:

$$:g: := \sum_{i=1}^{n} \frac{\partial g}{\partial x_i}\frac{\partial}{\partial p_i} - \frac{g}{\partial_i}\frac{\partial}{\partial x_i}\,. \tag{3.151}$$

Unfortunately, if the Hamiltonian is dependent on s because for example a_s is calculated from an s-dependent field like a fringe field (for more information see section 3.1.7), then the eq. (3.150) is no longer applicable.

There is a way to describe the map using Lie transformations for maps that have s-dependent Hamiltonians between their initial and final values. To do this the phase space is extended, by introducing an independent variable σ and transforming s into a new dynamical variable. With the new independent variable is an associated canonical momentum p_s. The extended Hamiltonian becomes:

$$H = \frac{\delta}{\beta_0} - \sqrt{\left(\frac{1}{\beta_0} + \delta - \frac{q\phi}{P_0 c}\right)^2 - (p_x - a_x)^2 - (p_y - a_y)^2 - \frac{1}{\beta_0^2\gamma_0^2}} - a_s + p_s\,. \tag{3.152}$$

As σ is independent when the Hamiltonian is integrated between $s = 0$ and $s = L$, then the transfer map can be written in terms of Lie transformations in terms of σ:

$$f(\sigma) = e^{-\sigma:H:} f(0)\,. \tag{3.153}$$

The extended Hamiltonian, in eq. (3.152) can be split into integrable terms [34]. With an appropriate gauge transform the horizontal vector potential a_x becomes 0. The paraxial approximation is also taken, to restate $|p_x|, |p_y| \ll 1$. Therefore the splitting of the Hamiltonian becomes:

$$\bar{H} \approx H_1 + H_2 + H_3\,. \tag{3.154}$$

With H_1:

$$H_1 = -\left(\frac{1}{\beta_0} + \delta\right) + \frac{1}{2\beta_0^2\gamma_0^2}\left(\frac{1}{\beta_0} + \delta\right)^{-1} + \frac{\delta}{\beta_0} + \frac{p_x^2}{2\left(\frac{1}{\beta_0} + \delta\right)} + p_s\,, \tag{3.155}$$

and H_3:

$$H_3 = -a_s \,, \tag{3.156}$$

and H_2:

$$H_2 = \frac{(p_y - a_y)^2}{2D} \,, \tag{3.157}$$

and where D is:

$$D = \sqrt{1 + \frac{2\delta}{\beta_0} + \delta^2} \,. \tag{3.158}$$

H_1 and H_3 are integrable, but as H_2 depends on both coordinates and momentum, a different technique is required. Wolski shows how H_2 can be represented as the generator of a Lie transformation, and that it can then be further composed into Lie transformations with integrable generators [10, p. 322].

Here is the Lie transformation which can be later composed of other transforms:

$$e^{-\Delta\sigma:H_2:} = e^{:I_y:} \exp\left(-\Delta : \frac{p_y^2}{2D} :\right) e^{-:I_y:} \,, \tag{3.159}$$

which is only valid as long as:

$$e^{:I_y:} p_y = p_y - a_y \,. \tag{3.160}$$

I_y above is given by:

$$I_y = -\int_0^y a_y(x, y', s) dy' \,. \tag{3.161}$$

Wolski shows that $e^{-\Delta\sigma:H_2:}$ can be used to now decompose $e^{-\Delta\sigma:\bar{H}:}$ into the following integrable Lie transformations:

$$\begin{aligned} e^{-\Delta\sigma:\bar{H}:} &\approx e^{-\Delta\sigma:H_1+H_2+H_3:} \,, \\ &\approx e^{-\frac{\Delta\sigma}{2}:H_1+H_3:} e^{-\Delta\sigma:H_2:} e^{-\frac{\Delta\sigma}{2}:H_1+H_3:} \,, \\ &\approx e^{-\frac{\Delta\sigma}{4}:H_1:} e^{-\frac{\Delta\sigma}{2}:H_3:} e^{-\frac{\Delta\sigma}{4}:H_1:} e^{-\Delta\sigma:H_2:} e^{-\frac{\Delta\sigma}{4}:H_1:} e^{-\frac{\Delta\sigma}{2}:H_3:} e^{-\frac{\Delta\sigma}{4}:H_1:} \,. \end{aligned} \tag{3.162}$$

Equation (3.162) shows that the Lie transformation can be decomposed into smaller integrable Lie transformations. Wolski shows formulae for the smaller Lie transformations applied to the dynamical variables, and skips the results that are effectively identity transformations [10, p. 323]. This important result provides an explicit symplectic integrator for s-dependent fields, where the integration is over a step from σ_0 to $\sigma_0 + \Delta\sigma$. It can be seen that in the Lie transformation:

$$e^{-\frac{\Delta\sigma}{4}:H_1:}s = s + \frac{\Delta\sigma}{4}\,, \tag{3.163}$$

which represents a change in the variable s during the integration. This is possible due to the extension of the phase space and treating (s, p_s) as dynamical variables. The physical significance of this is that the vector potential $a_y(x, y', s)$ in eq. (3.161) is effectively sampled at different points of the integration step due to the change in s. Had the phase space not been extended then s would be fixed at the initial value of the integration.

3.3.2 Implicit Runge-Kutta

The Wu-Forest-Robin integrator discussed in section 3.3.1 required the paraxial approximation to integrate the split Hamiltonian terms of eq. (3.154).

The Runge-Kutta methods do not require the paraxial approximation. As spoken about already in the HL-LHC section (see section 3.1.3) the regions around the interaction regions with the smallest β^* must reach some large β inside the focusing inner triplet quadrupoles. These inner triplet quadrupoles must also have high strength fields to produce the required focusing to achieve the design β^*. A high strength focusing will result in greater transverse momenta. Therefore the paraxial approximation may not be a good approximation in these focusing regions. Therefore it is suitable to investigate the Runge-Kutta as an option for the fringe fields of the inner triplet.

The discussion of Runge-Kutta methods given below are drawn from [10]. The Runge-Kutta methods are symplectic under certain conditions. Unfortunately these same conditions mean that the Runge-Kutta methods are therefore implicit, meaning that an algebraic solution must be found at each step of integration. The additional algebraic solution needed at each step increases the computational cost of the integration. Therefore, one downside of a symplectic Runge-Kutta is that the integration scheme is more difficult to calculate and slower to calculate than the Wu-Forest-Robin.

Next the theory behind the Runge-Kutta will be detailed. Let the solution to the ordinary differential equation be:

$$\frac{dx}{ds} = f(x, s)\,, \tag{3.164}$$

where $x(s)$ with an initial condition of $x(s_0) = x_0$, and f is an arbitrary function. Runge-Kutta methods make it possible to integrate the ordinary differential equation in eq. (3.164):

$$x(s_n + \Delta s) = x(s_n) + \sum_{i=1}^{m} b_i \kappa_i \,. \tag{3.165}$$

b_i represent constant coefficients, the choice of which is specific to a choice of Runge-Kutta scheme. κ_i is calculated using:

$$\kappa_i = \Delta s f(x_n^{(i)}, s_n^{(i)}) \,, \tag{3.166}$$

where $x_n^{(i)}$ and $s_n^{(i)}$ are intermediate values. These intermediate values are themselves calculated using:

$$x_n^{(i)} = x_n + \sum_{j=1}^{m} a_{ij} \kappa_{ij} \,, \tag{3.167}$$

$$s_n^{(i)} = s_n + c_i \Delta s \,. \tag{3.168}$$

a_{ij} and c_i also represent constant coefficients, and like b_i are specific to the choice of Runge-Kutta scheme. Together a_{ij}, b_i, and c_i can be displayed in what is known as a Butcher tableau:

$$\begin{array}{c|cccc} c_1 & a_{11} & a_{12} & \cdots & a_{1m} \\ c_2 & a_{21} & a_{22} & \cdots & a_{2m} \\ \vdots & \vdots & \vdots & \ddots & \vdots \\ c_m & a_{m1} & a_{m2} & \cdots & a_{mm} \\ \hline & b_1 & b_2 & \cdots & b_m \end{array} \,. \tag{3.169}$$

It is also required that:

$$c_i = \sum_{j=1}^{m} a_{ij} \,. \tag{3.170}$$

The implicit midpoint rule is a scheme with the following Butcher tableau:

$$\begin{array}{c|c} \frac{1}{2} & \frac{1}{2} \\ \hline & 1 \end{array} \,. \tag{3.171}$$

This scheme is symplectic because it agrees with the following constraint:

$$b_i a_{ij} + b_j a_{ji} = b_i b_j \,. \tag{3.172}$$

The next step is to apply the implicit midpoint rule to the Hamiltonian system, which is more relevant to the requirements of this study. If x is chosen to be the vector of the dynamical variables of the Hamiltonian system $\vec{x} = (x, p_x, y, p_y, z, \delta)$, then the ordinary differential equation in eq. (3.164) has to be generalised to include the other coordinates. This can be done by using derivatives of the Hamiltonian:

$$\frac{d\vec{x}}{ds} = S\nabla_{\vec{x}} H(\vec{x}, s)\,, \tag{3.173}$$

where S is the antisymmetric matrix, and:

$$\nabla_{\vec{x}} = \left(\frac{\partial}{\partial x}, \frac{\partial}{\partial p_x}, \frac{\partial}{\partial y}, \frac{\partial}{\partial p_y}, \frac{\partial}{\partial z}, \frac{\partial}{\partial \delta}, \right)\,, \tag{3.174}$$

is the differential operator. For this choice of f, then eq. (3.166) becomes:

$$\kappa_i = \Delta s S \nabla_{\vec{x}} H(\vec{x}_n^{(i)}, s_n^{(i)})\,. \tag{3.175}$$

The integration step of eq. (3.165) becomes:

$$x(s_n + \Delta s) = x(s_n) + \delta s \left.\frac{\partial H}{\partial p_x}\right|_{x=x_n^{(1)}, p_x = p_{xn}^{(1)}}\,, \tag{3.176}$$

$$p_x(s_n + \Delta s) = p_x(s_n) + \delta s \left.\frac{\partial H}{\partial x}\right|_{x=x_n^{(1)}, p_x = p_{xn}^{(1)}}\,. \tag{3.177}$$

The intermediate values of eqs. (3.167) and (3.168) becomes:

$$x_n^{(1)} = x(s_n) + \frac{1}{2}\delta s \left.\frac{\partial H}{\partial p_x}\right|_{x=x_n^{(1)}, p_x = p_{xn}^{(1)}}\,, \tag{3.178}$$

$$p_{xn}^{(1)} = p_x(s_n) + \frac{1}{2}\delta s \left.\frac{\partial H}{\partial x}\right|_{x=x_n^{(1)}, p_x = p_{xn}^{(1)}}\,. \tag{3.179}$$

Wolski shows that for the case of a Hamiltonian representing a relativistic particle within a sextupole field, exact solutions of the integral steps (eqs. (3.176) and (3.177)) can be written in terms of $x(s_n)$ and $p_x(s_n)$.

There are a family of implicit Runge-Kutta integrators known as Gauss methods or Gauss-Legendre methods of which the implicit midpoint rule (eq. (3.171)) is just one.

In this study the implicit midpoint integrator is used as the Runge-Kutta integrator of choice. Whilst it is less performant than the Wu-Forest-Robin integrator due to its increased computational cost, it provides an interesting comparison as unlike the Wu-Forest-Robin it does not require the paraxial approximation. It is also a symplectic integrator, which the truncated Wu-Forest-Robin is not.

Chapter 4

Method

In this chapter, the techniques employed to produce the results (chapter 5) are discussed. Two magnetic field models are used to describe the inner triplet quadrupole fringe field. These are the *numeric field* and *Enge field*. These fields are processed so that they can be described using generalised gradients. The generalised gradients are also used to produce transfer maps via integrators that use the vector potential as a parameter. The transfer maps can then be used to perform particle tracking studies. Particle tracking was used in several studies to find: the transfer functions of the transfer maps, the chromaticity exhibited by the HL-LHC lattice, and the tune shift with amplitude exhibited the HL-LHC lattice. Finally, frequency map analysis was used to analyse the stability of the HL-LHC beam.

In the first part of this chapter, the techniques concerning the magnetic field data are described. This includes the initial simulation of the HL-LHC inner triplet magnetic field and its construction into a full 3-dimensional field. There are two magnetic field models of the inner triplet that are discussed: the numeric field and the Enge field. The *numeric field* refers to descriptions that derive from the magnetic field generated from simulation by S. Bermudez [35]}. The *Enge field* refers to the analytic description described by Muratori et al. [5].

The generation of generalised gradients for both numeric and Enge fields is then described. The generalised gradients construction requires a description of the magnetic field data lying on a cylindrical surface, which is achieved via cubic spline interpolation. Afterwards, how the generalised gradients are generated from this cylindrical magnetic field is outlined.

In the second part of the chapter the key steps which are necessary to construct the HL-LHC lattice model used in the results are described. The first step was to generate a lattice description for use in SAMM from a pre-existing MAD lattice file. The next step was to modify the lattice description in the relevant points to allow the addition of a fringe field. The addition of a fringe field can modify the linear dynamics of the lattice, and so the method to restore the chromaticity to a desired value is also described.

In the final part of the chapter, the techniques which are used to investigate the effect of the fringe field in the HL-LHC are described in detail. The results of these techniques will later form the basis of the results chapter (chapter 5).

4.1 Magnetic field descriptions of the inner triplet

4.1.1 Simulating the numeric field

The inner triplet magnets have been modelled and the resultant magnetic field data that would be generated by the magnetic geometry was simulated by S. Bermudez [35]. The field data itself has been simulated in two partitions along the longitudinal axis; for $z \in [300, 700]$ mm and $z \in [700, 1100]$ mm, in steps of 5 mm. There is a regular grid in the transverse plane for each point in z. The gridpoints are from 0 mm to 75 mm, in 3 mm steps, for both x and y coordinates. This data forms a 3-D grid in the first Cartesian quadrant, when the partitions are combined, is spaced 0.8 m in length along the magnetic axis. The Cartesian components of magnetic field data, $B = (B_x, B_y, B_z)$, have been calculated at each grid point.

Both partitions of data share an x-y grid at the $z = 700$ mm point. There can be different ways of combining the partitions. The method that was chosen for the numeric grid data was to take the average of both 700 mm points.

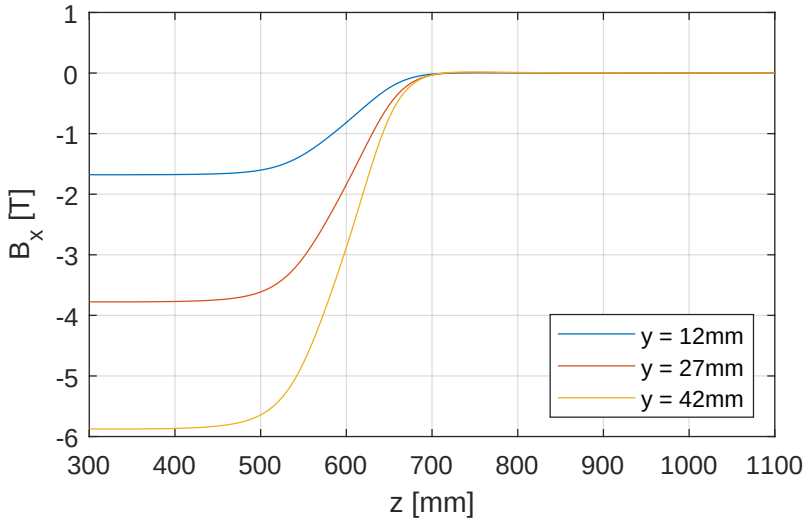

FIGURE 4.1: The magnetic field data of an HL-LHC inner triplet quadrupole magnet produced via simulation using an electromagnetic code. The horizontal component is shown, B_x, at $x = 0$ mm and for different y values. The field spans the region, along the z axis, between full field in the body of the magnet and vacuum.

To generate a full 3-D field that includes values for negative x and y, the relevant symmetry operations, as necessary for a quadrupole field (see fig. 3.1c), were performed.

The resultant field will therefore be on a grid $x, y \in [-75, 75]$ mm in 3 mm steps, and $z \in [0, 800]$ mm in 5 mm steps.

4.1.2 Fitting the Enge field

Techniques have been developed by Muratori et al. [5] to produce analytical descriptions of a fringe field. These techniques will be used to contrast the numeric field data provided in section 4.1.1. The analytic descriptions derived by Muratori et al. are general and can therefore be applied to different fringe field models. Enge fringe fields, introduced in section 3.1.5, have the advantage of being a model that can approximate a multipole fringe field. The analytical descriptions used in this thesis are the same as the the analytical descriptions derived by Muratori et al. in [5] and are therefore based on an Enge model.

The Enge model is required to be fit to the numeric model given in section 4.1.1. The first step of the fitting process is to rescale the field and offset it appropriately, using eqs. (4.1) to (4.3), so that the resultant field shape can be fitted appropriately by the analytic field description outlined by Muratori et al. [5].

$$x' = \zeta_{\text{scale}} \cdot x \,, \tag{4.1}$$

$$y' = \zeta_{\text{scale}} \cdot y \,, \tag{4.2}$$

$$z' = \zeta_{\text{scale}} \cdot (z - \zeta_{\text{offset}}) \,, \tag{4.3}$$

where ζ_{scale} and ζ_{offset} are scaling and offsets respectively [5]. In conjunction with two other free parameters used for fitting, b and b_{scale}, the Enge field can then be calculated using [5]:

$$\begin{aligned} B_x = b_{\text{scale}} \Bigg[y' + \frac{b}{2\sqrt{2}\,(1-b^2)} \times \Big\{ &\ln\left(1 + e^{\sqrt{2}z' + ih}\right) - \ln\left(1 + e^{\sqrt{2}z' - ih}\right) \\ &+ \ln\left(1 + e^{\sqrt{2}z' - i\bar{h}}\right) - \ln\left(1 + e^{\sqrt{2}z' + i\bar{h}}\right) \Big\} \Bigg] \,, \end{aligned} \tag{4.4}$$

$$\begin{aligned} B_y = b_{\text{scale}} \Bigg[x' + \frac{ib}{2\sqrt{2}\,(1+b^2)} \times \Big\{ &\ln\left(1 + e^{\sqrt{2}z' + ih}\right) - \ln\left(1 + e^{\sqrt{2}z' - ih}\right) \\ &- \ln\left(1 + e^{\sqrt{2}z' - i\bar{h}}\right) + \ln\left(1 + e^{\sqrt{2}z' + i\bar{h}}\right) \Big\} \Bigg] \,, \end{aligned} \tag{4.5}$$

$$B_z = b_{\text{scale}} \left[\frac{-ib^2}{\sqrt{2}\,(1-b^4)} \times \left\{ \ln\left(1+e^{\sqrt{2}z'+ih}\right) + \ln\left(1+e^{\sqrt{2}z'-ih}\right) - \ln\left(1+e^{\sqrt{2}z'-i\bar{h}}\right) - \ln\left(1+e^{\sqrt{2}z'+i\bar{h}}\right) \right\} \right], \tag{4.6}$$

where h, $\bar{h}$ are functions defined as follows:

$$h = \frac{1}{\sqrt{2}}\left(\frac{1}{b}+b\right)x' + \frac{i}{\sqrt{2}}\left(\frac{1}{b}-b\right)y', \tag{4.7}$$

$$\bar{h} = \frac{1}{\sqrt{2}}\left(\frac{1}{b}+b\right)x' - \frac{i}{\sqrt{2}}\left(\frac{1}{b}-b\right)y'. \tag{4.8}$$

The b parameter controls how the off-axis fringe field decays longitudinally. The fringe field on axis is not affected by the b parameter [5].

The Enge field was fit to the numeric field data to provide the best agreement. The fitting was performed by A. Wolski [36]. The same numeric field data was used for the fit as in section 4.1.1 , and the same symmetry reconstruction was used to generate the full 3-D field. One crucial difference in this case was that the field data was reflected in $z = 0$. Thus the result this would represent a fringe field that begins as field-free to full strength with increasing z. Another difference in this case was that the grid data files were combined differently compared to section 4.1.1. The $z = 700\,\text{mm}$ point is common to both longitudinal partitions of the grid data, 300 mm to 700 mm and 700 mm to 1100 mm. In this case the field data which the Enge field was fit against, used the 700 mm data values from the 300 mm to 700 mm partition. This is in contrast to the numeric field merging which took an average of these points (see section 4.1.1).

The results of the Enge fit are presented in table 4.1.

b	ζ_{scale}	ζ_{offset}	b_{scale}
1.5	-19.2	-0.6	7.3

TABLE 4.1: The values of the free parameters used to fit the analytic Enge field model to the simulated numeric field data.

As evidenced by fig. 4.2, the Enge field is in agreement with the numeric field. The numeric field exhibits an asymmetry that is not modelled by the Enge field; this is apparent in the longitudinal component in fig. 4.2c. For a static magnetic field, Gauss's law of magnetism and Ampère's circuital law (see eqs. (3.3) and (3.5)) can be simplified to:

$$\nabla \cdot B = \nabla \times B = 0\,. \tag{4.9}$$

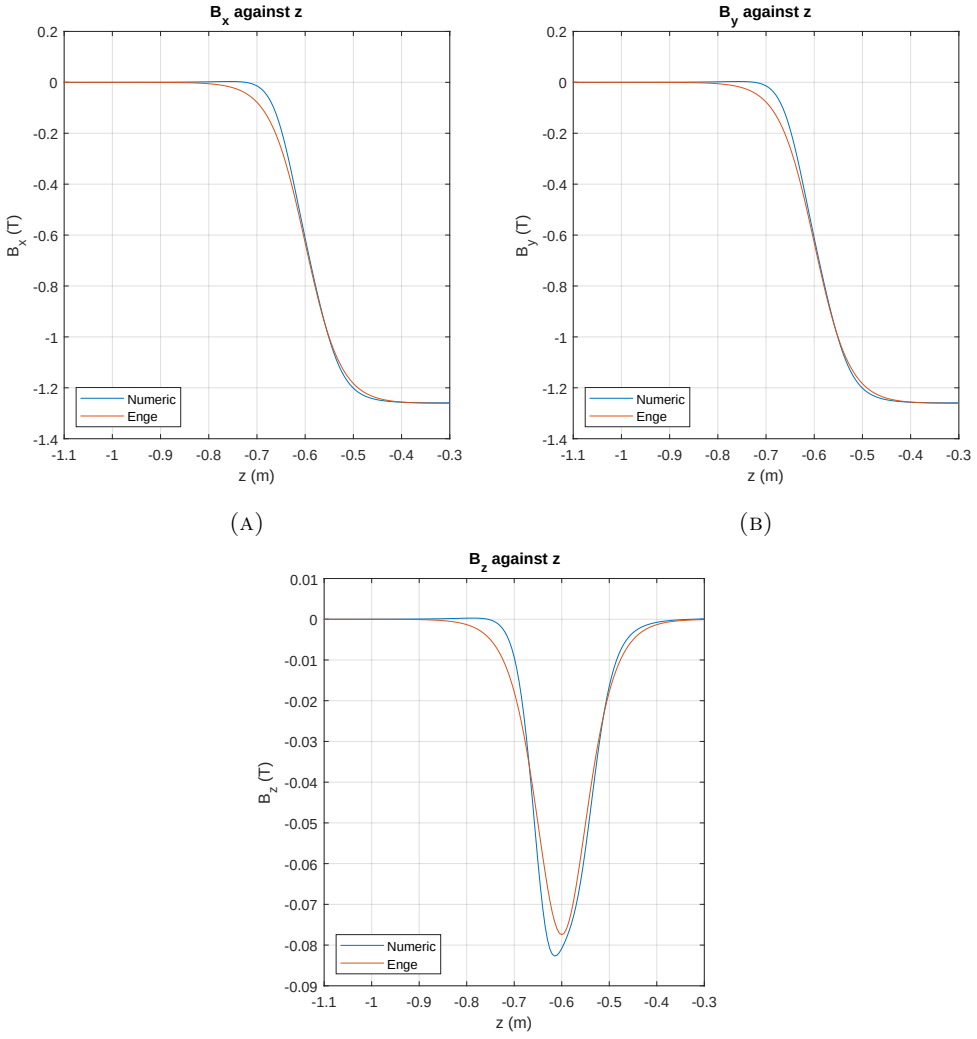

FIGURE 4.2: A comparison between a simulated field of the HL-LHC fringe region, and an analytic Enge field model which has been fit to the simulated field. A) The horizontal magnetic field B_x component at x=0, y=1mm, along the field axis. B) The vertical magnetic field component B_y at x=1mm, y=0 along the field axis. C) The longitudinal magnetic field B_z component at x=1mm, y=1mm along the field axis. [36]

Muratori et al. derives relationships between the transverse components and the longitudinal component that satisfy Maxwell's equations for a static field (given by eq. (4.9)) [5]. A change in coordinates is performed to make this easier [5]:

$$u = \frac{1}{\sqrt{2}}(x + iy) \,, \tag{4.10}$$

$$v = \frac{1}{\sqrt{2}}(x - iy) \,, \tag{4.11}$$

$$\zeta = \sqrt{2}z \,. \tag{4.12}$$

The magnetic field components in the new coordinates can be expressed in terms of the old as [5]:

$$B_u = \frac{1}{\sqrt{2}} \left(B_x + iB_y \right) , \tag{4.13}$$

$$B_v = \frac{1}{\sqrt{2}} \left(B_x - iB_y \right) , \tag{4.14}$$

$$B_\zeta = \frac{1}{\sqrt{2}} B_z \, . \tag{4.15}$$

Then, the relationships between the magnetic field components in the new coordinates can be written as [5]:

$$\partial_u B_u + \partial_\zeta B_\zeta = 0 \, , \tag{4.16}$$

$$\partial_v B_v + \partial_\zeta B_\zeta = 0 \, , \tag{4.17}$$

$$\partial_\zeta B_u - \partial_v B_\zeta = 0 \, , \tag{4.18}$$

$$\partial_\zeta B_v - \partial_u B_\zeta = 0 \, . \tag{4.19}$$

From these relationships it is clear that for a fringe field, i.e. when there is a longitudinal rate of change of B_u or B_v or $\partial_\zeta B_{u,v} \neq 0$, then B_ζ cannot be constant ($\partial_{u,v} B_\zeta \neq 0$). Therefore one reason for differences seen in the numeric field compared to the analytic Enge field in fig. 4.2c (the numeric field exhibits an asymmetry that the analytic Enge field does not) could be due to the fact that the longitudinal B_z is dependent on the longitudinal rate of change of B_x and B_y. The numeric field has a different longitudinal behaviour in B_x and B_y and therefore it can be expected to have a different behaviour in B_z compared to the Enge field.

4.1.3 Generating the generalised gradients

The generalised gradients were produced from surface data. The surface data describes the normal component of the magnetic field on a circular cylindrical grid. The theory behind the generalised gradients can be found in section 3.1.6.

In this subsection the surface data production is covered first, followed by the generalised gradient generation from the surface data.

Cylindrical surface data creation

The creation of cylindrical surface data required for the generalised gradients required different methods for the numeric field and the analytic Enge field.

First the process of creating the cylindrical surface data for the numeric field is described. For the numeric field the magnetic grid data described one Cartesian quadrant across two longitudinal partitions of 300 mm to 700 mm and 700 mm to 1100 mm. The number of data points in a single partition was $(n_x, n_y, n_z) = (26, 26, 81)$. When the two files are joined the number of points in z is 161, this is due to the $z = 700\,\text{mm}$ being shared across partitions. The combined partition data is representative of the magnetic field in one Cartesian quadrant. Reflecting the quadrant along the x and y axes result in a $51 \times 51 \times 161$ grid. Note that there are grid points lying on both axes of reflection: the x and y axes. Finally the data is reflected in z which produced a $51 \times 51 \times 321$ grid.

In the case of the numeric field data, the grid data is interpolated using cubic splines to construct the surface data. The normal component of the magnetic field on a cylindrical surface was calculated for a grid of points, where $n\phi = 64$ and $nz = 400$, spanning the curved surface of the cylinder. The cylinder has a radius of 60 mm. As the axis of the cylinder is parallel to the z-axis, the normal magnetic field component can be calculated with the horizontal and vertical field components using $B_\rho = B_x \cos\phi + B_y \sin\phi$.

In section 3.1.6 it was mentioned that errors on the field descriptions generated using generalised gradients get smaller when approaching the cylindrical axis. There is also the inverse effect, that errors grow for field descriptions outside the cylinder. As it has already been mentioned, the cylinder radius chosen for this study was 60 mm.

An estimation can be used when considering the cylinder radius in terms of the amplitudes of the particles from the closed orbit. In later sections the HL-LHCv1.0 lattice will be detailed, but some key properties are needed for the discussion here. The maximum value of β_x across the lattice is $\beta_x = 20.894 \times 10^3\,\text{m}$, the x-coordinate of the closed orbit at that point is $x_{\text{co}} = -1.646 \times 10^{-2}\,\text{m}$, and the emittance is $\epsilon_x = 3.35 \times 10^{-10}\,\text{m rad}$. Using the ellipse in fig. 3.9, a simple estimation can be calculated:

$$x_{\max} = \sqrt{2\beta_x J_x} = 3.74 \times 10^{-3}\,\text{m}\,, \tag{4.20}$$

where $x_{\max}$ is an estimation of the maximum x offset from the closed orbit, and the action, J_x, was chosen to be equal to the emittance (the average of all actions in a bunch). In the frequency map analysis results, particles up to 20 beam sizes from the closed orbit will be tracked. When taking into account the closed orbit the result becomes:

$$x_{\text{co}} + 20 \times x_{\text{max}} = 5.84 \times 10^{-2}\,\text{m}\,, \tag{4.21}$$

$$x_{\text{co}} - 20 \times x_{\text{max}} = -9.13 \times 10^{-2}\,\text{m}\,. \tag{4.22}$$

Therefore these estimations suggest that the particles with the greatest initial amplitudes may be at risk of experiencing fields greater than the radius of the cylinder and would therefore experience larger errors.

David Newton's BlitzDA code was used to do the spline interpolation. More information about the program is given in the method section, section 4.4, and examples of its usage with other studies is summarised in section 2.4. Spline fitting is useful because it can be applied to arbitrary functions. Cubic splines exhibit C^2 continuity, which means the spline is a twice differentiable function that is continuous as well as its first and second derivatives. Splines also have the advantage of local fitting, and are therefore not constrained to globally fit an entire range like a polynomial fit.

As mentioned previously, the process to create the cylindrical surface data for the Enge field differs from the numeric field. The Enge field can be reconstructed at any point by using the fitting parameters and eqs. (4.4) to (4.6). This is an advantage over the surface data construction of a numeric field that relies on interpolation to calculate intermediate data. The Enge field was calculated on the grid of points on the surface of the cylinder with a radius of 60 mm, and the same number of points as the numeric field were used, $n\phi = 64$ and $nz = 400$.

For consistency, across both sets of surface data, the z values were transformed to start from $z = 0\,\text{m}$. The surface data is also reflected about $z = 0.8\,\text{m}$ so the data is periodic in z as is required in the generalised gradient construction.

The surface data constructed from the numeric field can be seen in fig. 4.3, and the surface data for the Enge field can be seen in fig. 4.4. Figure 4.5 shows the difference between the surface data produced from both the numeric field and the Enge field.

The surface data plotted in figs. 4.3 to 4.5 exhibit four fold reflectional symmetry in the x and y axes, and a reflection at the midpoint of the longitudinal axis $z = 0.8\,\text{m}$. The reflections in z are to be expected given the construction of the surface data. The four fold reflection symmetry in the case of the numeric field can be expected due to its construction, and the Enge field inherits this symmetry due to it having been fit to the numeric field.

The analytic Enge surface data appears to be asymmetric in each quadrant which is different from the numeric field surface data. This could be due to the fact that the analytic Enge solution was based on a non-symmetrised model and therefore does not respect the symmetry constraint imposed on a quadrupole (see eq. (3.25)). To restate

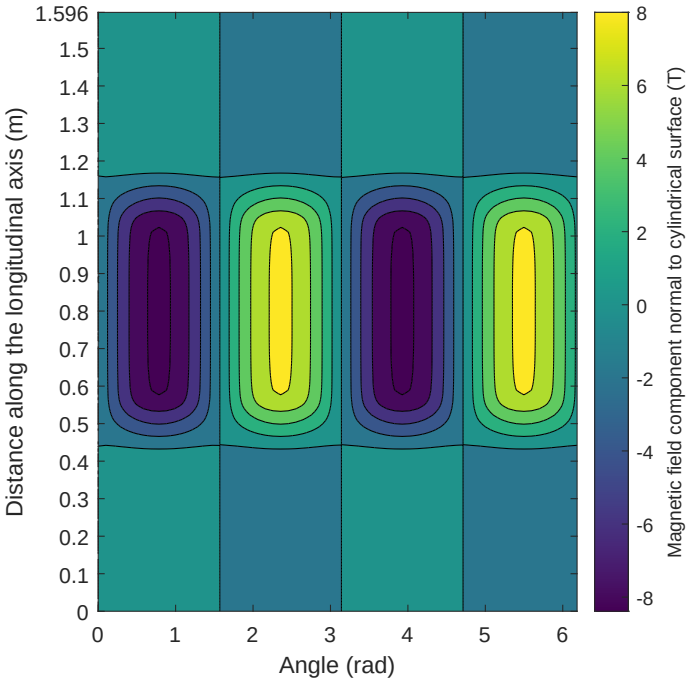

FIGURE 4.3: A contour plot of the numeric field component normal to the curved surface of a circular cylinder, with an axis along the magnetic axis.

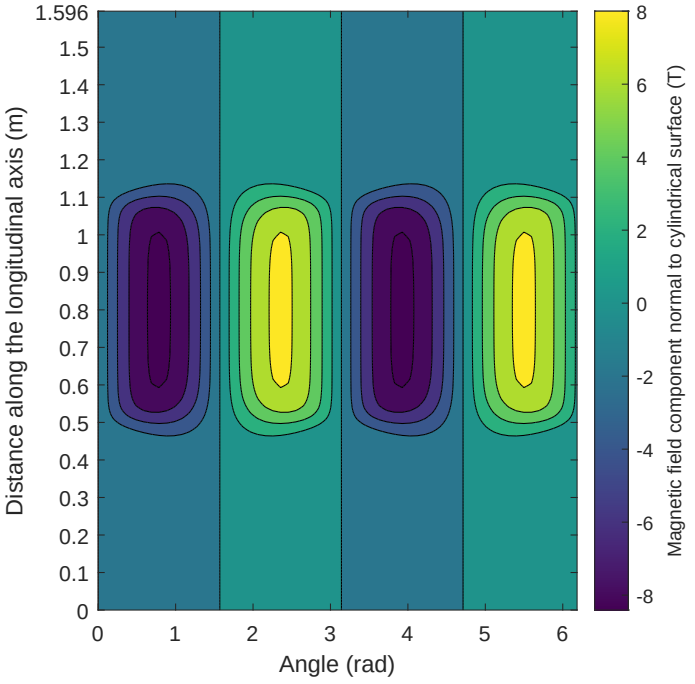

FIGURE 4.4: A contour plot of the analytic Enge field component normal to the curved surface of a circular cylinder, with an axis along the magnetic axis.

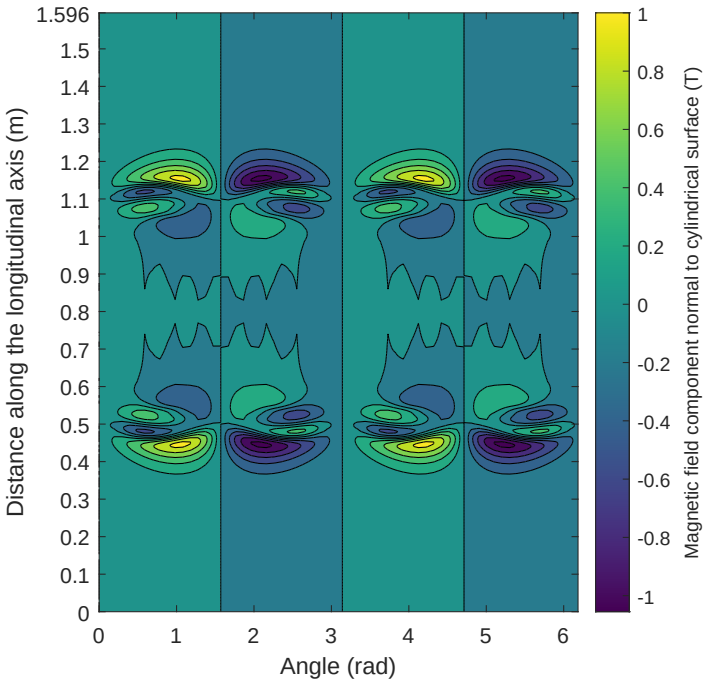

FIGURE 4.5: A contour plot of the difference in the magnetic field component normal to the curved surface of a circular cylinder between the numeric and analytic Enge fields. The cylinder axis lies along the magnetic axis.

the symmetry constraint: for a quadrupole, where $n = 2$, a rotation of the field by π/n should result in a field that is equal to the unrotated field but with an opposite sign (as discussed already in section 3.1.1).

Using the numeric fringe field data plotted in fig. 4.1, it appears that the region of the fringe field is approximately contained within the region between 400 mm to 800 mm. Converting this approximate fringe field region to the scale of the surface data results in two fringe field regions (due to reflection in z): 0.3 m to 0.7 m and 0.9 m to 1.3 m.

It can be seen that the major differences, in fig. 4.5, between the surface data constructed using the numeric field and the analytic Enge field is also confined to this region. Differences in the longitudinal fall-off of the fringe field could be expected due to the numeric field and analytic field being different models. The fact that the differences are not centred and symmetric about the expected quadrupole poles, $\pi/4, 3\pi/4, \cdots$, is due to the asymmetry exhibited by the Enge surface data.

The differences between the surface data should be taken note of, and if there is evidence that the differences are too large for the analytic Enge field to be used in place of the numeric field, then work can be done to reduce those differences. This could be achieved by using a symmetrised model of the analytic Enge field to eliminate the asymmetry seen in the current Enge surface data. Also a different fringe field model could be chosen that better replicates the longitudinal fall-off of the numeric field.

Constructing generalised gradients from surface data

The generalised gradients are produced using a two-dimensional Fourier transform of the cylindrical surface data. This two-dimensional Fourier transform is shown in eq. (3.34) [31, eq 17.3.3] [1]:

$$\tilde{\tilde{B}}_\rho(R,m,k) = [1/2\pi]^2 \int_{-\infty}^{\infty} dz \exp(-ikz) \int_0^{2\pi} d\phi \exp(-im\phi)\, B_\rho(R,\phi,z)\ , \tag{3.34 revisited}$$

where $B_\rho(R,\phi,z)$ is the normal magnetic field component on the cylindrical surface, and $\tilde{\tilde{B}}_\rho(R,m,k)$ is the Fourier transformed field. How the generalised gradients, $C_m^{[n]}$, are explicitly generated from Fourier transform results is shown in eq. (3.37) [31, eq 17.3.8]:

$$C_m^{[n]}(z) = i^n (1/2)^{|m|} (1/|m|!) \int_{-\infty}^{\infty} dk \left[k^{n+|m|-1}/I_m(kR)\right] \tilde{\tilde{B}}_\rho(R,m,k) \exp(ikz)\ , \tag{3.37 revisited}$$

where m is the multipole order, n is the index of the generalised gradient function of a given multipole, and $I_m(kR)$ is the modified Bessel function.

The wavenumber was calculated using eq. (4.23).

$$k_z^{[i_z]} = i_z\, 2\pi/(z_{\max} - z_{\min})\,, \tag{4.23}$$

where i_z the indexed z position, $i_z \in [0, n_z]$, and n_z is the total number of points in z. The equivalent wavenumber in ϕ, k_ϕ, was sampled between $[0, 2\pi)$ and so the resulting wavenumber binning in ϕ corresponds with integer cycles over 2π. The number of points in z, number of points in ϕ, is determined from the surface data file chosen.

The Fourier transform of the numeric data, as can be seen in fig. 4.6, show that the Fourier magnitudes are larger when k_ϕ is even. Furthermore every fourth bin in k_ϕ has a smaller magnitude than the other even bins that do not meet that criteria. This is in agreement with the allowed symmetries of a quadrupole, i.e. $m = 2, 6, 10, \cdots$. The Fourier transform of the analytic Enge data also show larger Fourier magnitudes for even k_ϕ bins rather than odd bins. But the Enge case does not show the same disparity as the numeric case between even k_ϕ bins not divisible by 4, and even bins divisible by 4. In fact in fig. 4.7 it can be seen that the k_ϕ bins divisible by 4 have larger magnitudes, particularly for small k_z values.

There is a cut in the data performed in the Fourier transform results; the wavenumber results $k_z \geq 400\,\mathrm{m}^{-1}$ are ignored. This is because the Fourier data becomes smaller as

[1] Unless otherwise stated i is the imaginary unit $i = \sqrt{-1}$.

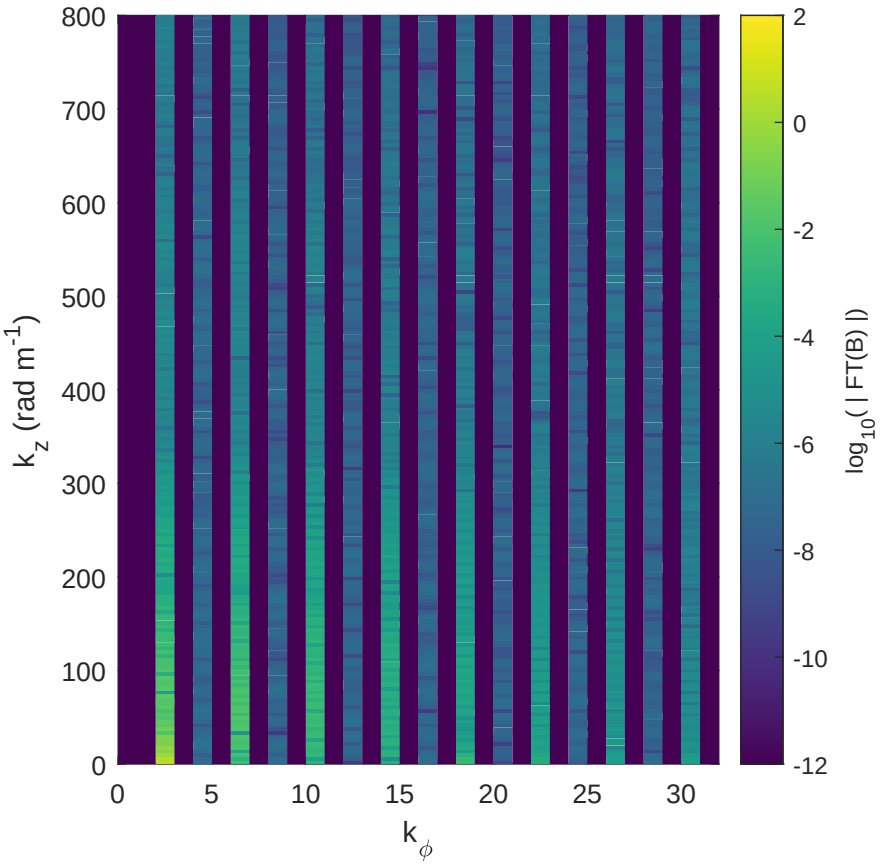

FIGURE 4.6: The magnitude of the 2-D Fourier transform of the numeric surface data. Fourier transforms were performed in ϕ and z. The Fourier transform is shown across the ϕ and z wavenumbers.

k_z increases. Therefore to reduce the influence of noise, the higher frequency components were removed.

There is a separation in the Fourier magnitudes between the even and odd bins (see figs. 4.6 and 4.7), with the odd bins being many orders of magnitude less than the even. The Fourier results with very small magnitudes were interpreted as adding unwanted noise. Therefore it was decided to cut the Fourier results for all values less than $10^{-10}\,\mathrm{T\,m\,rad}$, with the cut values set to zero.

In producing the Taylor maps for the HL-LHC, a test proton with energy 7 TeV was used. To produce a map describing an opposite magnetic field an anti-proton was used instead. An entrance fringe field, zero field to full field, can then be created by integrating for a proton travelling through the field between the bounds of 0 to 0.8 m. Similarly an exit field could be produced from 0.8 to 1.6 m.

For the numeric field data the generalised gradients were calculated for $0 \leq m, l \leq 7$. The generalised gradients for the solenoid terms, $m = 0$, were set equal to zero. This was because the solenoid term should not have a large contribution to the field,

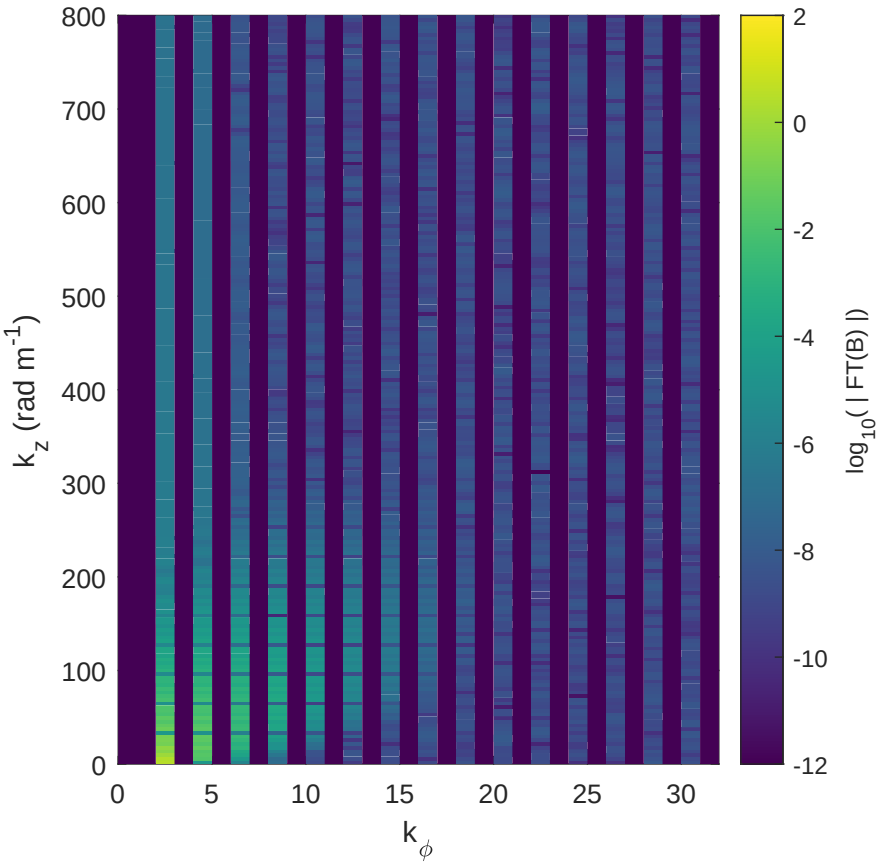

FIGURE 4.7: The magnitude of the 2-D Fourier transform of the analytic Enge surface data. Fourier transforms were performed in ϕ and z. The Fourier transform is shown across the ϕ and z wavenumbers.

and additionally Dragt recommends that the solenoid terms should not be used when generating generalised gradients from cylindrical surface field data [31]. The generalised gradients were calculated up to order $m = 7$ because the use of the differentiated vector potential, ∂A, in the Wu-Forest-Robin integration means that the vector potential has to be one order higher than the magnetic multipole being considered. The generalised gradients are then used to produce an analytic description of the magnetic vector potential A [31, eq.15.4.21 - 15.4.26].

$$A_x^{m,c} = -(1/m)x\,\mathrm{Im}[(x+iy)^m]\sum_{l=0}^{\infty}(-1)^l\frac{m!}{2^{2l}l!(l+m)!}C_{m,c}^{[2l+1]}(z)(x^2+y^2)^l\,, \tag{3.45 revisited}$$

$$A_y^{m,c} = -(1/m)y\,\mathrm{Im}[(x+iy)^m]\sum_{l=0}^{\infty}(-1)^l\frac{m!}{2^{2l}l!(l+m)!}C_{m,c}^{[2l+1]}(z)(x^2+y^2)^l\,, \tag{3.46 revisited}$$

$$A_z^{m,c} = -(1/m)\,\mathrm{Im}[(x+iy)^m]\sum_{l=0}^{\infty}(-1)^l\frac{(2l+m)m!}{2^{2l}l!(l+m)!}C_{m,c}^{[2l]}(z)(x^2+y^2)^l\,, \tag{3.47 revisited}$$

$$A_x^{m,s} = -(1/m)x\,\mathrm{Re}[(x+iy)^m]\sum_{l=0}^{\infty}(-1)^l\frac{m!}{2^{2l}l!(l+m)!}C_{m,s}^{[2l+1]}(z)(x^2+y^2)^l\,, \tag{3.48 revisited}$$

$$A_y^{m,s} = -(1/m)y\,\mathrm{Re}[(x+iy)^m]\sum_{l=0}^{\infty}(-1)^l\frac{m!}{2^{2l}l!(l+m)!}C_{m,s}^{[2l+1]}(z)(x^2+y^2)^l\,, \tag{3.49 revisited}$$

$$A_z^{m,s} = -(1/m)\,\mathrm{Re}[(x+iy)^m]\sum_{l=0}^{\infty}(-1)^l\frac{(2l+m)m!}{2^{2l}l!(l+m)!}C_{m,s}^{[2l]}(z)(x^2+y^2)^l\,. \tag{3.50 revisited}$$

The magnetic vector potential can then be used with a Wu-Forest-Robin integrator to produce a Taylor series describing a transfer map through the field. This series has to be truncated at some finite order; this truncation means that despite using a symplectic integrator, the transfer map is non-symplectic.

The Runge-Kutta process was different to the Wu-Forest-Robin Taylor map process. The generalised gradients were only produced for the $m = 2, 6$ cases, because these are the main multipole components allowed for a quadrupole for $m \leq 7$. The vector potential, A_x, A_y, was then calculated from the generalised gradients. The first and second derivatives of the vector potential were calculated and used for the calculation of ∇H and $\nabla^2 H$.

Once the generalised gradients have been constructed for the numeric and Enge fields, and transfer maps generated from them - the next step is to put the transfer maps into the HL-LHC lattice.

4.2 Construction of the HL-LHC in the simulation

4.2.1 Importing a MAD lattice into SAMM

The HL-LHC model lattice used in the particle tracking studies is the conversion of a MAD [7] lattice description into SAMM [14], (for more information on SAMM see section 4.5). The following steps were used to generate the MAD lattice and import into SAMM.

1. The lattice in MAD form was produced from a MAD-X script [2].
2. The script was designed to calculate the Twiss parameters for a lattice, and was run on a thin lens HL-LHC lattice sequence file[3].
3. The script is also designed to generate a file of the appropriate magnetic field errors for a given random seed and lattice description. The random seed used was set to 1.
4. The file of magnetic error files was parsed by a SAMM file[4]. The file of Twiss parameters was parsed by a SAMM file[5]. Both parser files were provided by A. Wolski [37].
5. The Error file parser was run first. It would iterate the MAD-X error table of the HL-LHC and store the multipole field errors into an array.
6. The Twiss file parser was run after the Error file parser. It was used to iterate over the HL-LHC sequence and convert the MAD elements in SAMM equivalents, whilst maintaining their order and copying their relevant properties. The elements that the parser was able to convert were: Marker, Drift, Kicker, Multipole, and RF-Cavity. The Twiss parser would then apply the multipole field errors, converted using the Error file parser, and apply them to the multipole in the SAMM lattice.

4.2.2 Adding fringe fields to the HL-LHC lattice

To add fringe fields it is necessary to also add additional components. For an entrance field the following is added:

- A negative drift.
- A retuning element.

[2]The script was job-tracking.mask from CERN's servers.
[3]The sequence file was hllhc_thin.seq, for HL-LHCv1.0.
[4]The file was ParseMADXFieldErrors.m.
[5]The file was ParseMADXTwiss.m.

- The fringe field.
- A positive drift.

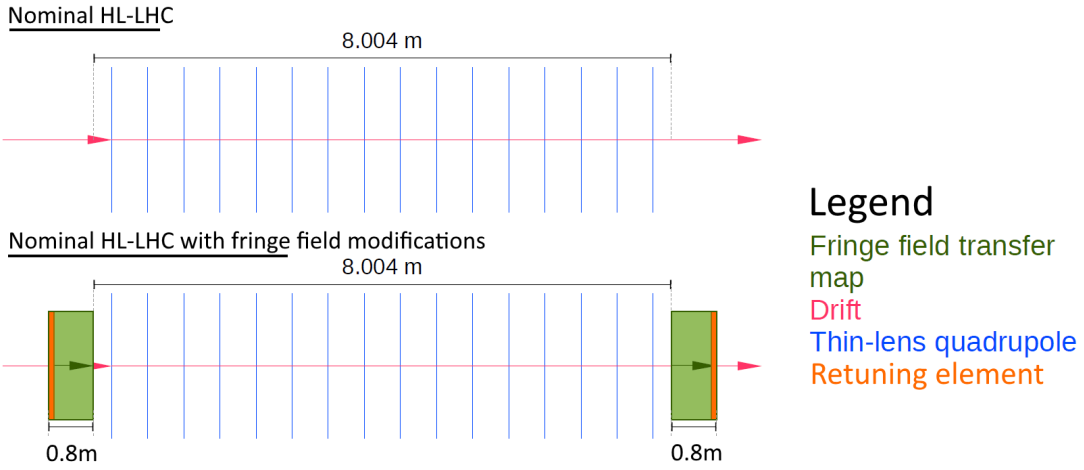

FIGURE 4.8: A schematic showing how drifts and a retuning element are added in combination with the fringe fields on either side of the inner triplet which is decomposed into thin lenses. NB: The length of the full magnet is for a HL-LHCv1.0 Q1 or Q3 class inner triplet magnet, whereas a Q2 class has a length 6.792 m

The negative and positive drifts are required to place the fringe fields in the correct location within the lattice. The retuning element is a linear inverse of the fringe field and is intended to remove the contribution of the fringe field to the linear dynamics of the lattice (primarily in the form of additional focusing). For an exit field, the components are added in the opposite order as can be seen in fig. 4.8. It should be clarified that in fig. 4.8 the retuning element actually has infinitesimal length. This is because the SAMM tracking code (see section 4.5) applies the linear inverse to the linear dynamics but does not treat it as having length. It is shown as a thicker orange element attached to the fringe field length to make it distinguishable on the schematic.

4.2.3 Restoring the desired chromaticity of the HL-LHC lattice

Adding fringe fields to the lattice has an effect on the chromaticity of the ring, even after the retuning element has been added.

Once the fringe fields are added the tunes and chromaticity of the lattice is calculated. The magnetic field strengths of the sextupoles around the lattice are then readjusted by the same factor to change the chromaticity to the desired value. The chromaticity stated in the MAD files is used for reference.

The chromaticity is calculated using turn by turn tracking and then using a NAFF algorithm to find the tune. See section 4.3.2 for more information about the NAFF algorithm.

The chromaticity restoration algorithm used in this thesis makes use of Matlab's *fzero* root finding algorithm [38], also known as Brent's method [39]. The chromaticity restoration algorithm calculates the chromaticity of a lattice. The function passed to the root finding algorithm was: the difference between the horizontal chromaticity calculated by SAMM and the chromaticity determined by MAD-X (each for the HL-LHCv1.0 lattice). The independent variable of Brent's method was the rescaling factor to be applied to the sextupoles. Each of the sextupoles in the HL-LHC ring was then scaled by this factor. Therefore the chromaticity restoration algorithm, by using Brent's method, would try to find the rescaling factor that results in (or as close to) a zero difference between the desired MAD chromaticity and the chromaticity calculated using NAFF.

4.3 Techniques used to produce results

4.3.1 Transfer functions

The transfer function is produced by tracking particles through a map with a range of initial displacements, and then comparing these displacements against the resultant change in momentum through the map. Transfer functions can also be known as trace space plots [40]. This method should reveal the magnitude of a focusing or defocusing effect.

Any non linearities in the focusing can be examined by fitting a straight line to the fit and then plotting the data minus the linear fit. This technique will be referred to later as the nonlinear transfer function

4.3.2 Numerical analysis of fundamental frequencies (NAFF)

Laskar [26] describes an algorithm called Numerical Analysis of Fundamental Frequencies (NAFF) which can be used to find the fundamental frequencies of quasi periodic motion of a Hamiltonian system. It is useful because NAFF gives a better estimation of the largest peak of Fourier-transformed data by several orders of magnitude compared to a plain Fourier transform.

First, a Fourier transform is applied to a sampling of the quasi periodic motion over a certain period of time. The Fourier transform results in an approximation of the frequency space of the motion being considered. A window function is applied to the data, usually in the form of a Hanning window [41]. The effect of the window is to reduce the side-lobes peaks neighbouring the fundamental frequency peaks; this is useful because peaks that are close by can distort each other and lead to a less accurate determination of the fundamental frequency. After applying the window, an iterative process is used to determine each fundamental frequency:

1. Find the maximum value of the Fourier transform.
2. Use quadratic interpolation for a better determination of the peak, ν_j, where j is the number of the frequency.
3. Remove this frequency component, $e^{i\nu_1 t}$, from the transform and repeat from Step 1, until as many frequencies as required have been identified.

4.3.3 Chromaticity investigations

The chromaticity can be determined in two ways: numerically or using a one turn map.

In the numeric method, the particles can be set up with a range of initial energy deviations from the reference energy. The particles are also given the same displacement from the closed orbit. This displacement is necessary as the tunes of the particles are then calculated by particle tracking and then computed using the NAFF algorithm; for very small displacements the tune computation was not accurate (see section 4.3.2). Once the turns are computed for each particle, it is then a matter of determining the gradient of the tune against energy deviation at zero energy deviation. This can be done by fitting to a polynomial, and then using the fit values to compute the chromaticity. Imagine a hypothetical case where that energy deviation against tune is well approximated by a quadratic fit like in eq. (4.24):

$$\nu = p_1\delta^2 + p_2\delta + p_3\,, \tag{4.24}$$

where δ is the energy deviation and ν is the tune. It is easy to see by differentiation that the linear parameter p_2 is the gradient of the tune against energy deviation for $\delta = 0$.

In the one turn map method, the tune, ν, of particles with different momentum, dp, is investigated. Crucially these particles are also tracked in a lattice where the RF cavity frequency has been changed from reference frequency. The chromaticity is then calculated as the gradient of tune against dp.

4.3.4 Tune shift with amplitude

The *tune shift with amplitude* shows the change in tune of a particle for different displacements from the closed orbit.

The particles are set up to have a range of initial displacements from the closed orbit. The tune of each particle is calculated from turn-by-turn data produced by tracking simulations. More specifically the tune is found using a NAFF algorithm (more detail can be found in section 4.3.2) which gives a better determination of the peak position in the turn-by-turn Fourier power spectrum.

4.3.5 Frequency map analysis

In Laskar [24] a technique called *Frequency Map Analysis* (FMA) is discussed. It is used to describe how the tune of a particle changes, for an array of particles of different actions.

Particles with a tune that varies more are more likely to be unstable, in comparison to particles with a consistent tune. The change in tune is measured by:

$$\boldsymbol{\nu}_{\Delta} = \sqrt{\boldsymbol{\nu}^2_{[T_1,T_2]} + \boldsymbol{\nu}^2_{[T_2,T_3]}}\,, \tag{4.25}$$

where $\boldsymbol{\nu}_{[T_1,T_2]}$ is the tune calculated by the NAFF algorithm between turn number T_1 and T_2. The amount of turns to sample for NAFF is in the order of thousands of turns.

Therefore frequency map analysis can provide an estimate of dynamic aperture, but without the computationally expensive long-term tracking required of other techniques like survival plots. Frequency map analysis can also reveal changes in the general stability over phase space for different changes in lattice, particularly when errors and nonlinearities are introduced.

The frequency maps can be shown in action (analogous to coordinate space for fixed momenta), as well as in tune space. In tune space it can reveal which resonances have an impact on the beam. The geometry of the frequency map in tune space can also be important. Frequency maps can exhibit one or more folds, which could imply unstable fast escape regions [24]; therefore the stability of the folds are important to consider.

4.3.6 Processing the tracking results

The tracking data can produce values known as *not-a-number* (NaN) which represent floating point numbers that are undefined, e.g. the result due a division by 0. The particles which have NaNs in their coordinates after tracking are omitted.

NaNs are unordered, which means they cannot be less than, greater than, or equal to other floating point values. Therefore it is crucial to test for NaNs separately, because they will not test positive if they are outside the aperture limits. Also NaNs propagate in the sense that any floating point operations with a NaN as an operand will produce a NaN. Therefore NaNs could not be used in a tune calculation, for example, because the NaNs would propagate via the algorithm resulting in a NaN as the value calculated for the tune [42].

Also any particles with distance flag equal to zero, which represents them reaching an extent greater than a limit, are considered lost. These particles are also removed.

4.4 BlitzDA differential algebra code

The BlitzDA differential algebra code is a program that was developed by D. Newton. It has been used in various studies requiring accurate descriptions of electromagnetic fields [18, 21, 19, 20]. It is a C++ program that is designed for quick numerical processing of differential algebra objects, such as the expansion of a Taylor series. The code has functionality to do basic maths (add, multiply, etc.) to the series as well as performing operations such as differentiation. This code was used in this work to compute generalised gradients from surface data. The generalised gradients were then used to describe the vector potential as a power series. The vector potential was then integrated to produce a transfer map in the form of a truncated Taylor series.

The code is composed of several modules, at the core is a Differential Algebra module.

The spline interpolation within BlitzDA is performed by a Fortran library designed by Wolfgang Schadow [43]. The library is simply referred to as B-spline library, and BlitzDA uses version 2.2. The library comes in Fortran 77 and Fortran 90 versions, of which the BlitzDA code uses the Fortran 90 version. The Fortran code is designed to be similar to an implementation in the IMSL library released by Rogue Wave Software [44]. The spline functions themselves are based on work by Carl de Boor [45]. The steps taken to perform the spline interpolation is as follows:

- dbsnak - Computes the "not-a-knot" spline knot sequence. [44]
- dbs3in - Computes a three-dimensional tensor-product spline interpolant, returning the tensor-product B-spline coefficients. [44]
- dbs3vl - This function evaluates a three-dimensional tensor-product spline, given its tensor-product B-spline representation. [44]

The routines used were set to generate cubic splines. The advantage of b-splines for fitting an arbitrary function is that they are piecewise polynomial descriptions, and so can fit complicated curves/surfaces with several points of inflection. The b-splines also offer the ability to interpolate. This is how the field was calculated for the points on the cylindrical surface.

4.5 SAMM particle tracking code

The SAMM particle tracking code is a particle tracking program developed by A. Wolski [14]. It is developed first as a MATLAB teaching tool, and so has a clear structure and is easy to extend and interface with the code. The code has extensions written in

the programming languages C and CUDA which are more performant numerically and so allow for results to be produced faster.

In this work, SAMM has been used extensively to describe beams of protons, as well as the HL-LHC lattice. SAMM has classes to define an accelerator beam and an accelerator beamline. The beamline itself can be made up of the following components such as the marker, drift space, solenoid, orbit corrector, dipole, quadrupole, sextupole, a generic multipole, RF cavity, RF accelerating structure, master oscillator, and beam position monitor. In this study the multipole component was used to model the magnets imported from the MAD-X thin lens HL-LHCv1.0 lattice. This method is further described in section 4.2. The multipole component can model upto an arbitrary number of multipoles.

SAMM can also compute the transfer matrix by using the results of tracking particles with a small change from the reference trajectory. Furthermore SAMM can calculate the closed orbit in a looped accelerator or storage ring. The dispersion can be computed indirectly by changes to the master oscillator. The Courant-Snyder parameters along the ring can also be calculated using SAMM.

Chapter 5

Results

The stability of the beam is critical to the successful operation of the HL-LHC. As established in earlier chapters, fringe fields have the potential to reduce the beam stability due to their nonlinear effects. In this chapter, the effect of fringe field models on the stability of the beam is compared with the no fringe lattice. This was investigated primarily with frequency map analysis.

The results from other techniques, namely generalised gradients, transfer functions, chromaticity, and tune shift with amplitude, were used to characterise the beam and lattice.

5.1 Generalised gradients

The generalised gradients produced from two field models are compared in this section. The numeric field model is generated via a magnetic field program which models the HL-LHC inner triplet magnet. The Enge field model is an analytic model, which is fitted against the numeric model. The construction of these field models is covered in sections 4.1.1 and 4.1.2 for the numeric and Enge models respectively.

Generalised gradients are a technique used to describe s-dependent fields decomposed into sets of multipole fields, indexed by parameter m, and the differentials of those fields, which are indexed by parameter l. The parameters chosen for producing the generalised gradients are shown in section 4.1.3 and the theoretical background is covered more extensively in section 3.1.6.

Generalised gradients for the comparison in this section were calculated for both fields where $m = 0, 1, \ldots, 7$ and where $l = 0, 1, \ldots, 7$.

It should be noted that the generalised gradients produced are subject to a couple of cuts, setting generalised gradients that met certain conditions equal to zero, e.g. $C(z) = 0\,, \forall z$.

The first cut to consider is the cut on higher wavenumbers; wavenumbers for which $k_z \geq 400\,\mathrm{m}^{-1}$ are ignored. To summarise the explanation set out in section 4.1.3, this was to reduce the effects of noise on the construction of the generalised gradients. Any extra noise in the generalised gradients could affect the calculation of the vector potential, which would also influence the generation of transfer maps, and ultimately the tracking.

The second cut to note is the cut during the Fourier transform calculation in the generalised gradient calculation. There is a cut for all Fourier values less than $10^{-10}\,\mathrm{T\,m\,rad}$. This again was to reduce the effect of noise during the creation of the generalised gradients.

The generalised gradients produced from the numeric field are non-zero for $m = 2, 6$. This is consistent with the expected multipoles allowed by symmetries as discussed in section 3.1.1. In the case of the analytic Enge field it also has a non-zero octupole term, $m = 4$. This is due to choice of equations used for the Enge field here. In Muratori et al. the equations that describe the Enge field can be either symmetrised or non-symmetrised [5].

The choice in this study was to use the non-symmetrised solutions, as it is a simpler model. The non-symmetrised solutions are non-symmetric for the four-fold case, and therefore the analytic fringe fields do not have the four-fold symmetry expected by a true quadrupole [5]. In other words when transposing the coordinates, $x \Leftrightarrow y$, the magnetic field is not symmetric when transposing $B_x \Leftrightarrow B_y$. The octupole term, $m = 4$, is likely to feature more prominently due to there being no symmetric constraints. This can be seen in the $m = 4$ results in (fig. 5.2).

The magnetic symmetric constraint is described by eq. (3.25) and accompanying text in section 3.1.1. Furthermore an octupole field, $m = 4$, can be seen in fig. 3.2a.

It is possible to use a symmetrised solution for the Enge field, but according to Muratori et al. it requires the superposition of two quadrupole solutions [5]. If a symmetrised solution is used for the Enge field it is possible that this could lead to agreement in the octupole components between the numeric field and the Enge field.

The generalised gradients are even functions when $l = 0$ which corresponds with their construction by reflecting the fringe field in the z-axis (for more information see section 4.1.3). It is a property of the generalised gradients that a generalised gradient with order $l + 1$, $C_m^{[l+1]}$, represents a derivative in z of the lower-order generalised gradient with order l, $C_m^{[l]}$. As such it can be noted that in figs. 5.1 to 5.3 that each function alternates between an odd and an even function with increasing l. This is expected due to the differentiation of an even function producing an odd function and vice versa.

As can be seen in the $m = 2$ graphs (fig. 5.1), there is good agreement between the two field models for small l.

Figures 5.1 to 5.3 also exhibit oscillatory behaviour as l increases. This can be attributed to the continued differentiation of an analytic function, $f(t)$, over some region in t-space, which can produce oscillations that grow larger in t-space [46].

As l gets larger the higher-order derivative behaviour between the models diverge. The Enge field exhibits less oscillations and smaller amplitudes, whereas in comparison the numeric field data exhibits oscillatory behaviour that exhibits more oscillations and greater amplitude for each step in l.

Section 4.1.2 details the fitting process of the Enge field to the numeric field. Similar discrepancies discussed in section 4.1.2 which can be seen in fig. 4.2 are also exhibited in the fig. 5.1. In particular the asymmetries visible in the B_z component of the Enge field (fig. 4.2c) are similar to those of the $C_2^{[1]}$ generalised gradient plotted in fig. 5.1b. This similarity can be attributed to the relationship between the partial derivatives of the magnetic field components for a magneto-static field. These relationships derives from Maxwell's magneto-static equations eqs. (4.16) to (4.19).

As can be seen by the $m = 6$ graphs (fig. 5.3), the generalised gradient $C_6^{[0]}$ which corresponds directly to the dodecapole field, shows that the numeric field exhibits a much larger amplitude than the Enge field. The shape of the graphs are the same for low orders of l. For the higher orders of l the rapid differentiation leads to differences in shape. The higher l-order generalised gradients also show much greater amplitudes for the numeric field compared with the Enge field which corresponds with the $m = 2$ graphs (fig. 5.1).

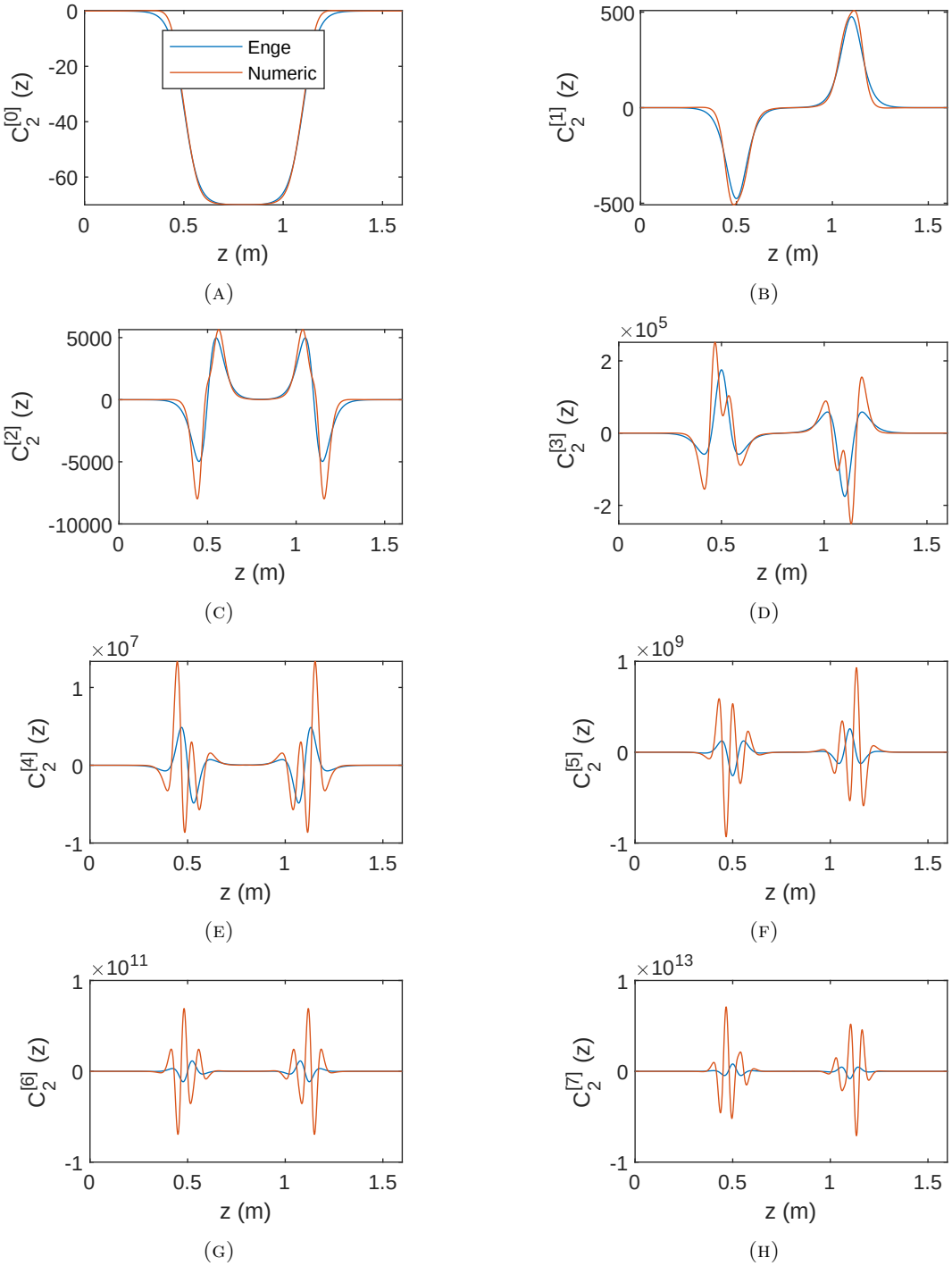

(A) (B) (C) (D) (E) (F) (G) (H)

FIGURE 5.1: A comparison of the generalised gradients, for multipole $m = 2$ and orders from $l = 0$ up to 7, of the analytic Enge field and the numeric field.

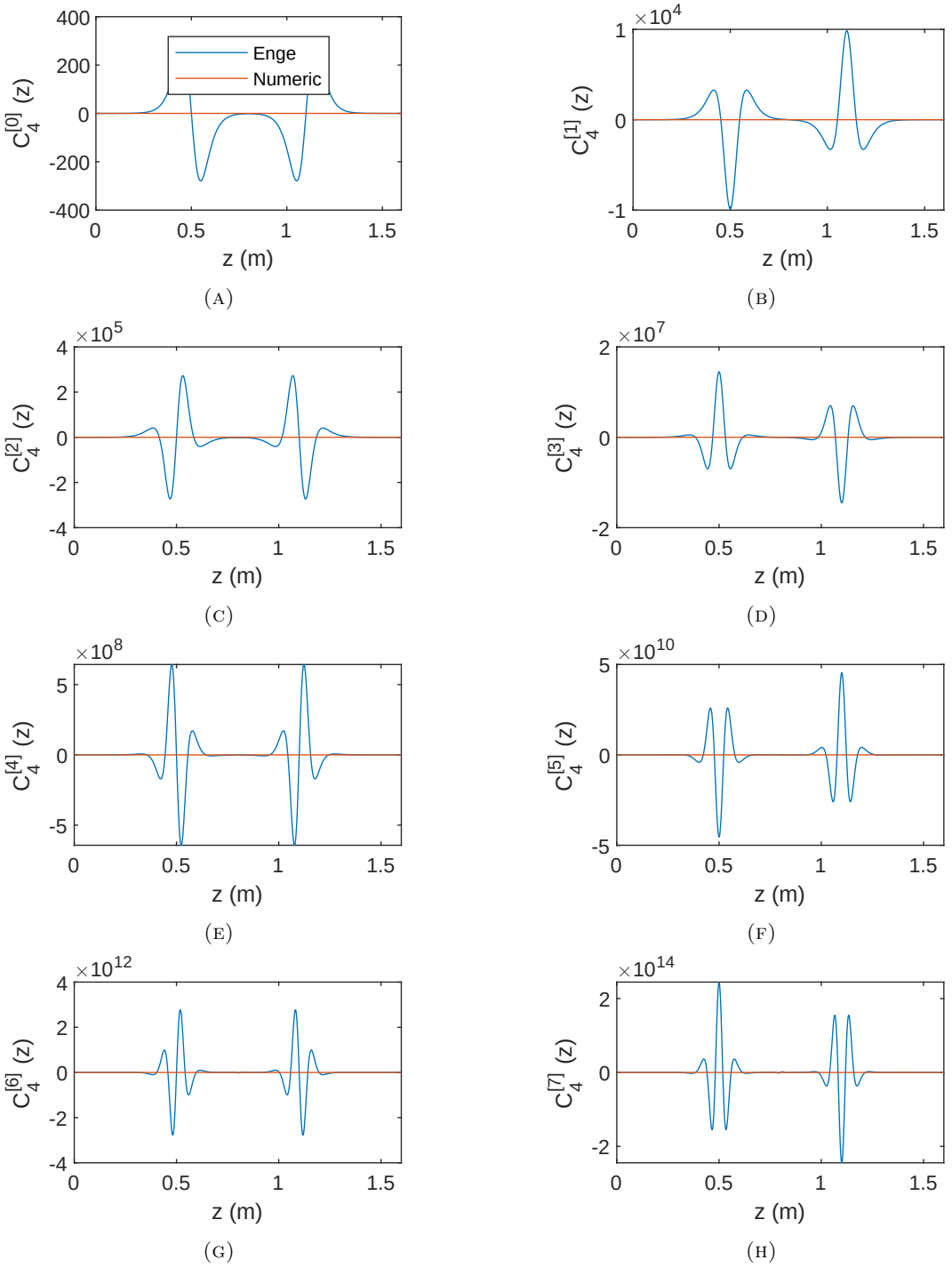

FIGURE 5.2: A comparison of the generalised gradients, for multipole $m = 4$ and orders from $l = 0$ upto 7, of the analytic Enge field and the numeric field.

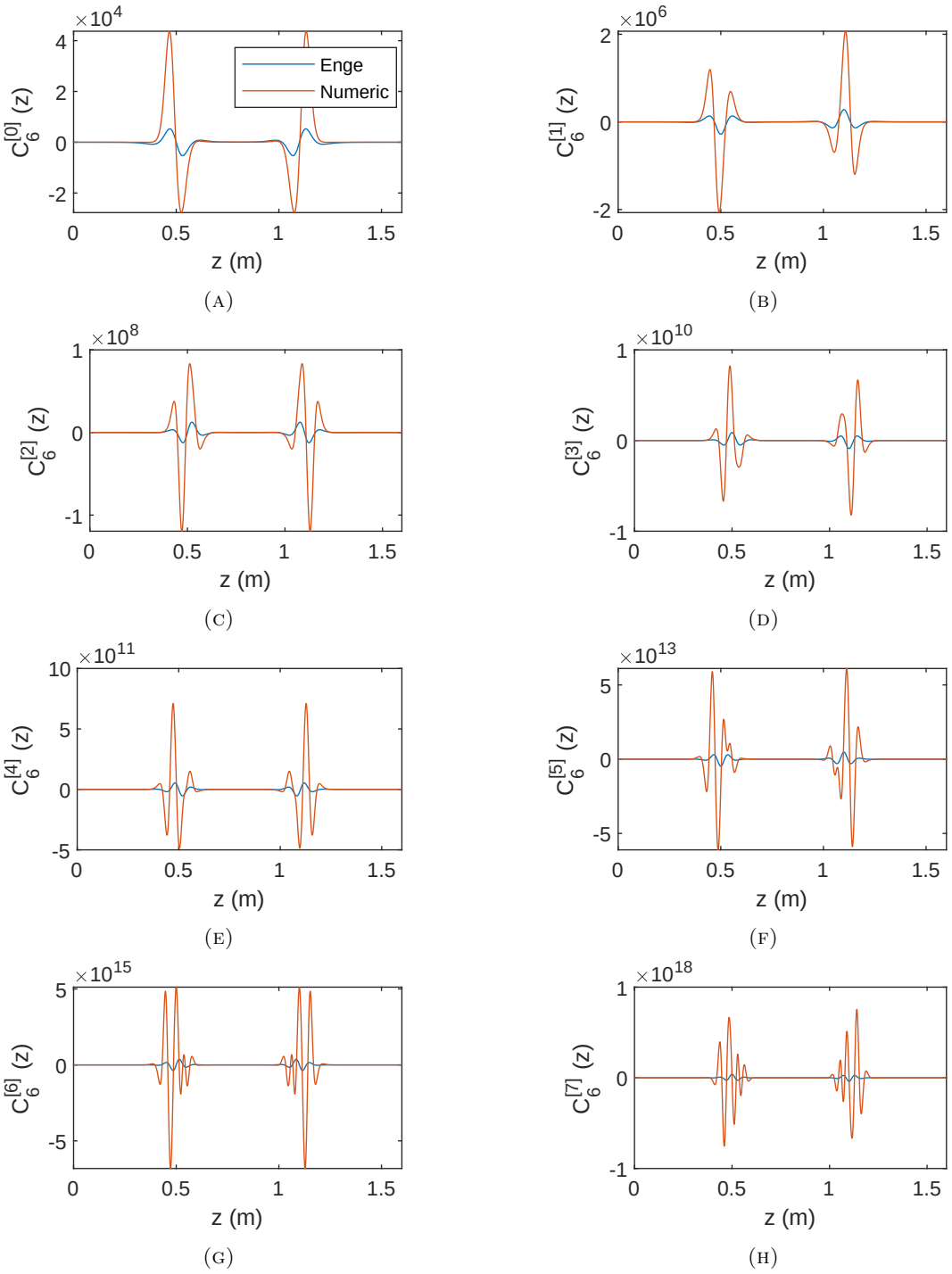

FIGURE 5.3: A comparison of the generalised gradients, for multipole $m = 6$ and orders from $l = 0$ up to 7, of the analytic Enge field and the numeric field.

5.2 Transfer functions

Transfer functions show the change in momentum for a given initial coordinate displacement. The results are obtained by tracking particles with these displacements, x_i, through different field models and calculating their change in momentum, δp_x. Thus this technique is useful in examining the focusing dynamics of accelerator components such as a quadrupole magnet. More information and theory behind transfer functions is covered in section 4.3.1. In this section linear and nonlinear transfer functions for both the Enge and numeric fields using the Taylor map or Runge-Kutta methods are presented.

Figures 5.4 to 5.7 show the transfer functions for the Enge and numeric fields, and for both integration methods: Taylor map and Runge-Kutta. On each subplot within the figures there are two axes; the left axis corresponds with the transfer function results unmodified, and the right axis corresponds with the nonlinear transfer function. As the fields are quadrupoles, the transfer functions are linear in shape. If a fifth order polynomial is fit to this linear transfer function, then the linear part (conventionally $f = ax + b$) can be removed from the data. The remainder after removing the linear part is referred to here as the nonlinear transfer function. The nonlinear transfer function shows the non-linearity of the transfer functions, which is otherwise difficult to see given their predominantly linear behaviour.

As stated previously the transfer functions cover the four fringe field models. The models are based either on a numeric (N) or Enge (E) field, and additionally a choice of numeric integration in the form of a Wu-Forest-Robin Taylor map (TM) or implicit Runge-Kutta (RK) integrator. The model with no fringe field is not included here because by definition there would be nothing to integrate over. Each case can be split into two: those for the entrance fringe (from no field into full field) and exit fringe (from full field to no field). Each of the former cases can be further split into results for the horizontal phase space and those in the vertical phase space. Lastly the transfer functions can be calculated for focusing and defocusing cases.

The transfer functions were fit using a fifth order polynomial (also known as a quintic polynomial); the equation of the polynomial fit is shown in eq. (5.1). The results of the fitting across the different dimensions is shown in tables 5.1 to 5.4. The column headings correspond with the parameters shown in eq. (5.1).

$$f = p_1 x^5 + p_2 x^4 + p_3 x^3 + p_4 x^2 + p_5 x + p_6 \,. \tag{5.1}$$

Several patterns are observed in these fits. The fifth order polynomials fit matches exactly the data in each case as shown in figs. 5.4 to 5.7. To confirm this agreement it is also observed in the nonlinear transfer functions, where the linear fit is subtracted from the data and plotted against a nonlinear fit. The nonlinear fit is represented by:

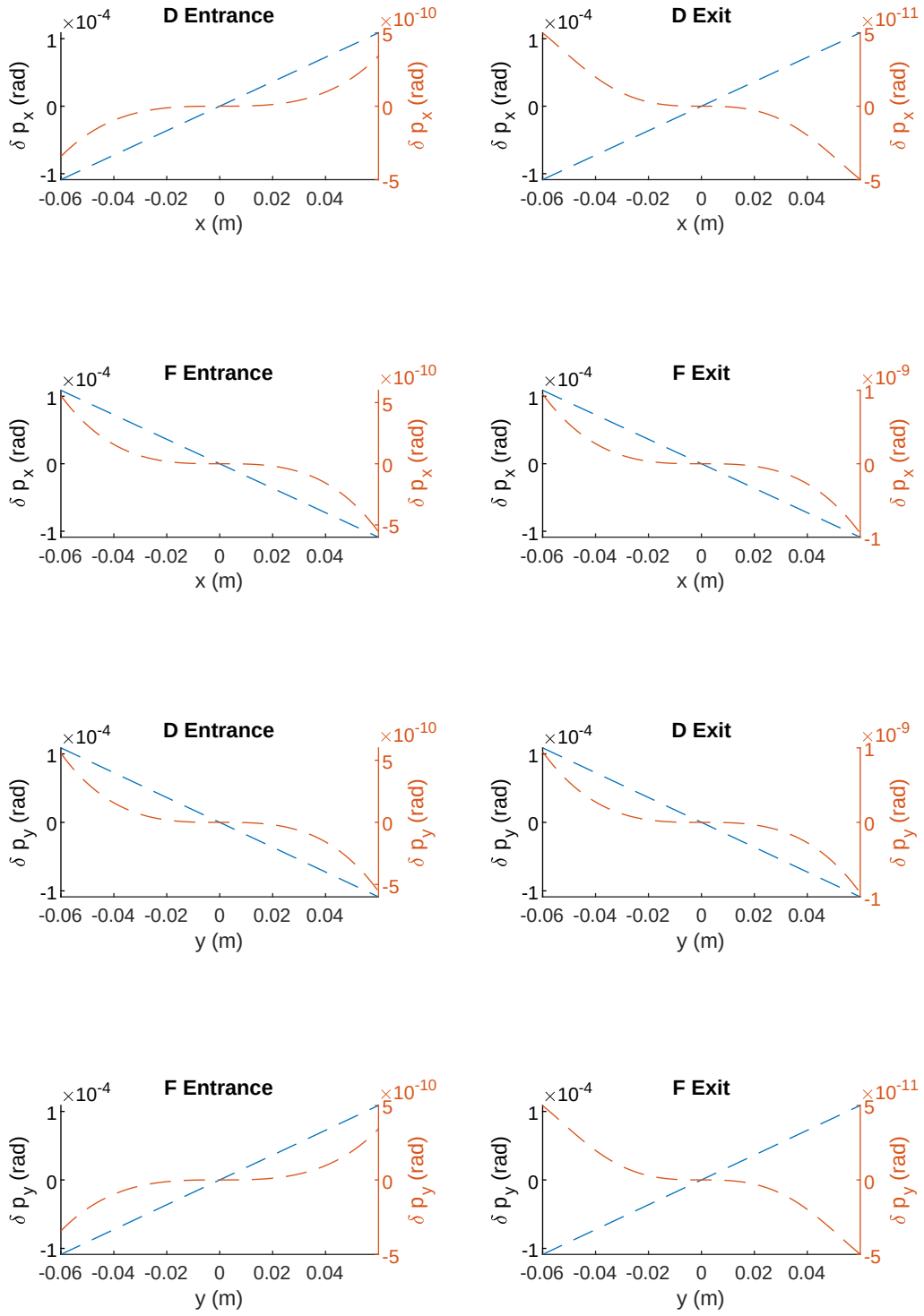

FIGURE 5.4: The transfer functions of the Enge field Runge-Kutta model. (Top four) Horizontal phase space. (Bottom four) Vertical phase space. (Blue plot/Left axis) Linear transfer function. (Red plot/Right axis) Nonlinear transfer function

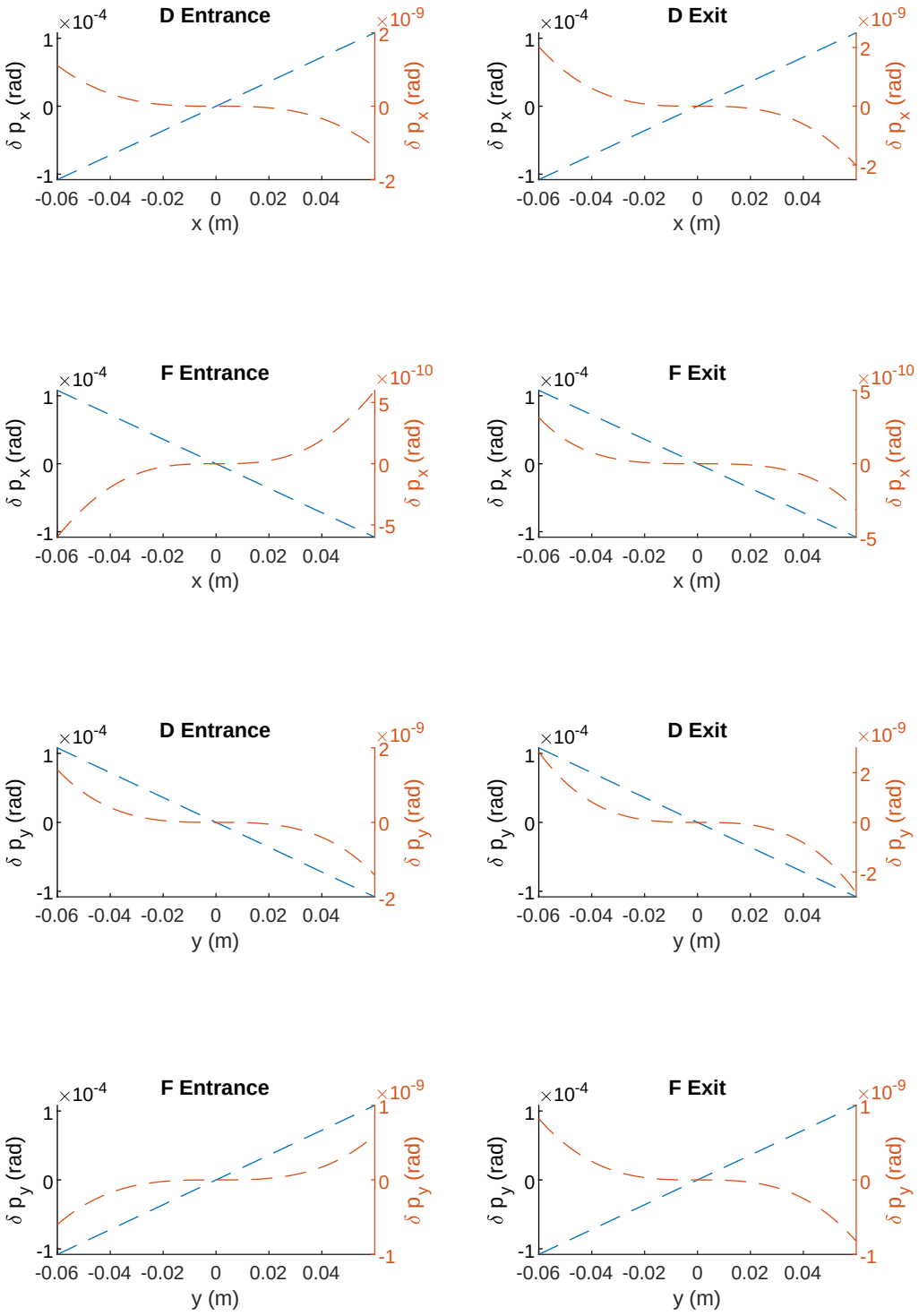

FIGURE 5.5: The transfer functions of the Enge field Taylor map model. (Top four) Horizontal phase space. (Bottom four) Vertical phase space. (Blue plot/Left axis) Linear transfer function. (Red plot/Right axis) Nonlinear transfer function

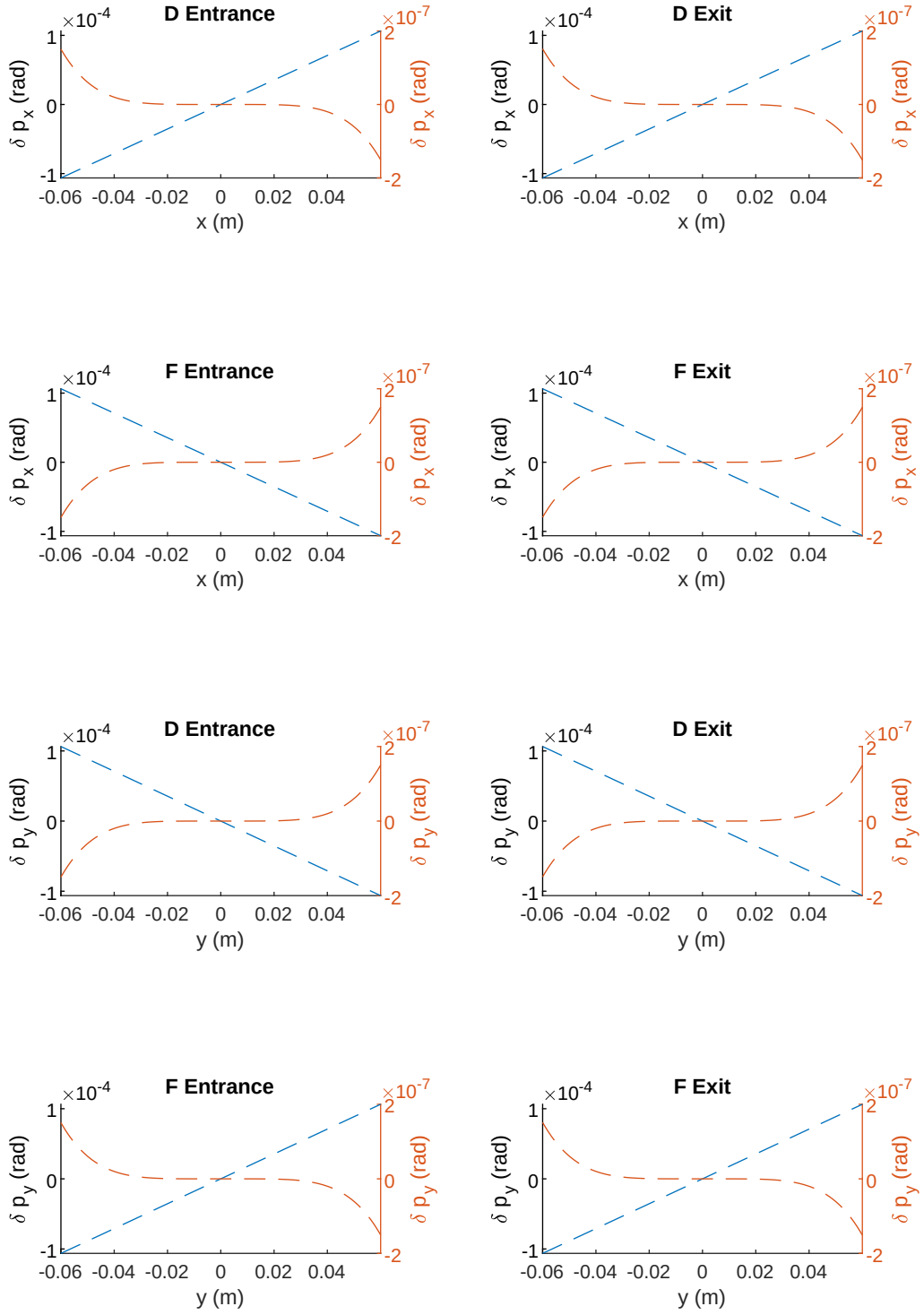

FIGURE 5.6: The transfer functions of the numeric field Runge-Kutta model. (Top four) Horizontal phase space. (Bottom four) Vertical phase space. (Blue plot/Left axis) Linear transfer function. (Red plot/Right axis) Nonlinear transfer function

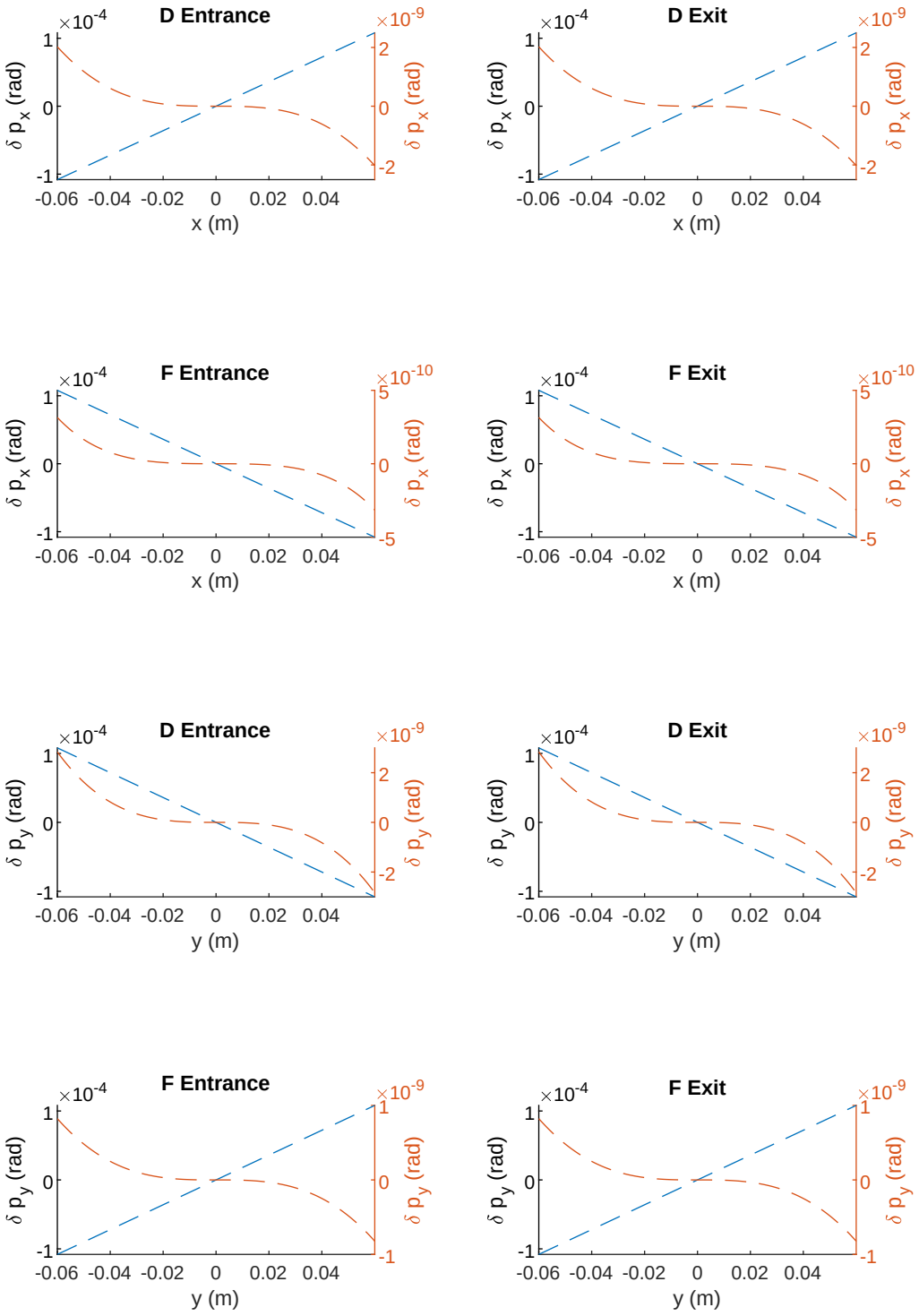

FIGURE 5.7: The transfer functions of the numeric field Taylor map model. (Top four) Horizontal phase space. (Bottom four) Vertical phase space. (Blue plot/Left axis) Linear transfer function. (Red plot/Right axis) Nonlinear transfer function

Magnet model and integrator and other properties	p1	p2	p3	p4	p5	p6
E-RK-D-Entrance-Horizontal	3.951E-05	-1.111E-14	1.443E-06	1.960E-17	1.813E-03	-5.748E-21
E-RK-D-Entrance-Vertical	-5.698E-05	1.231E-14	-2.371E-06	-3.524E-17	-1.813E-03	1.004E-22
E-RK-D-Exit-Horizontal	3.933E-05	-6.658E-15	-3.728E-07	3.579E-18	1.813E-03	-1.129E-21
E-RK-D-Exit-Vertical	-5.717E-05	1.067E-14	-4.183E-06	-3.724E-17	-1.813E-03	7.028E-22
E-RK-F-Entrance-Horizontal	-5.698E-05	5.869E-15	-2.371E-06	-1.623E-18	-1.813E-03	5.723E-21
E-RK-F-Entrance-Vertical	3.951E-05	-1.277E-14	1.443E-06	4.043E-17	1.813E-03	-1.732E-21
E-RK-F-Exit-Horizontal	-5.717E-05	9.012E-15	-4.183E-06	-1.248E-17	-1.813E-03	3.112E-21
E-RK-F-Exit-Vertical	3.933E-05	-7.415E-15	-3.728E-07	2.790E-17	1.813E-03	4.493E-21

TABLE 5.1: The transfer function polynomial fit coefficients for the Enge field Runge-Kutta.

Magnet model and integrator and other properties	p1	p2	p3	p4	p5	p6
E-TM-D-Entrance-Horizontal	6.958E-05	-7.010E-15	-5.391E-06	8.418E-18	1.801E-03	-4.392E-21
E-TM-D-Entrance-Vertical	-1.576E-04	4.363E-15	-5.986E-06	-2.233E-18	-1.801E-03	4.819E-21
E-TM-D-Exit-Horizontal	6.930E-05	-7.244E-15	-9.620E-06	8.882E-18	1.801E-03	-3.539E-21
E-TM-D-Exit-Vertical	-1.581E-04	1.092E-14	-1.256E-05	-1.535E-17	-1.801E-03	3.690E-21
E-TM-F-Entrance-Horizontal	-1.287E-04	3.854E-15	3.226E-06	-3.760E-18	-1.801E-03	7.705E-21
E-TM-F-Entrance-Vertical	4.067E-05	-9.757E-15	2.632E-06	1.644E-17	1.801E-03	-3.137E-21
E-TM-F-Exit-Horizontal	-1.290E-04	5.638E-15	-9.949E-07	-7.524E-18	-1.801E-03	3.790E-21
E-TM-F-Exit-Vertical	4.015E-05	-7.470E-15	-3.953E-06	1.421E-17	1.801E-03	-6.626E-21

TABLE 5.2: The transfer function polynomial fit coefficients for the Enge field Taylor map.

Magnet model and integrator and other properties	p1	p2	p3	p4	p5	p6
N-RK-D-Entrance-Horizontal	-1.938E-01	-6.024E-15	-1.671E-07	1.000E-17	1.774E-03	-4.744E-21
N-RK-D-Entrance-Vertical	1.936E-01	5.906E-15	-8.668E-07	-2.026E-17	-1.774E-03	-4.392E-21
N-RK-D-Exit-Horizontal	-1.942E-01	-3.815E-15	-1.938E-06	5.756E-19	1.774E-03	-3.564E-21
N-RK-D-Exit-Vertical	1.931E-01	1.354E-14	-2.635E-06	-4.421E-17	-1.774E-03	8.785E-22
N-RK-F-Entrance-Horizontal	1.936E-01	3.824E-15	-8.668E-07	-9.064E-19	-1.774E-03	3.639E-21
N-RK-F-Entrance-Vertical	-1.938E-01	-1.259E-14	-1.671E-07	4.332E-17	1.774E-03	-3.263E-22
N-RK-F-Exit-Horizontal	1.931E-01	7.522E-15	-2.635E-06	-4.357E-18	-1.774E-03	1.682E-21
N-RK-F-Exit-Vertical	-1.942E-01	-5.227E-15	-1.938E-06	1.725E-17	1.774E-03	3.664E-21

TABLE 5.3: The transfer function polynomial fit coefficients for the numeric field Runge-Kutta.

Magnet model and integrator and other properties	p1	p2	p3	p4	p5	p6
N-TM-D-Entrance-Horizontal	6.930E-05	-7.244E-15	-9.620E-06	8.882E-18	1.801E-03	-3.539E-21
N-TM-D-Entrance-Vertical	-1.581E-04	1.092E-14	-1.256E-05	-1.535E-17	-1.801E-03	3.690E-21
N-TM-D-Exit-Horizontal	6.930E-05	-7.244E-15	-9.620E-06	8.882E-18	1.801E-03	-3.539E-21
N-TM-D-Exit-Vertical	-1.581E-04	1.092E-14	-1.256E-05	-1.535E-17	-1.801E-03	3.690E-21
N-TM-F-Entrance-Horizontal	-1.290E-04	5.638E-15	-9.949E-07	-7.524E-18	-1.801E-03	3.790E-21
N-TM-F-Entrance-Vertical	4.015E-05	-7.470E-15	-3.953E-06	1.421E-17	1.801E-03	-6.626E-21
N-TM-F-Exit-Horizontal	-1.290E-04	5.638E-15	-9.949E-07	-7.524E-18	-1.801E-03	3.790E-21
N-TM-F-Exit-Vertical	4.015E-05	-7.470E-15	-3.953E-06	1.421E-17	1.801E-03	-6.626E-21

TABLE 5.4: The transfer function polynomial fit coefficients for the numeric field Taylor map.

$$f = p_1 x^5 + p_2 x^4 + p_3 x^3 + p_4 x^2 \,. \tag{5.2}$$

In the case of the Taylor maps, the linear term, corresponding to p_5 in eq. (5.1), is in agreement between numeric and Enge. However the Enge Runge-Kutta has a larger magnitude whereas the numeric Runge-Kutta has a smaller magnitude. Broadly speaking the focusing strength taken from p_5 is similar across all cases. It also exhibits symmetry as expected between focusing/defocusing, horizontal/vertical cases. The focusing horizontal quadrupole fields result produce a negative change to the momentum and therefore and a negative p_5 as expected.

One noticeable feature of the results shown in table 5.3 is that the numeric field Runge-Kutta has much larger quintic p_1 coefficients than the other cases. The numeric field Runge-Kutta also has a quintic coefficient that is opposite in sign to the other cases when comparing for Entrance/Exit, Focusing/Defocusing, Horizontal/Vertical. It is expected that the defocusing maps have gradients with a similar magnitude but opposite sign. This is due to fact that the defocusing maps were created using the same method as the focusing maps with one crucial difference. During the integration of the maps, the particle used for focusing maps is a proton, but for the defocusing maps it is an antiproton.

The entrance and exit results have quintic (5th) orders of similar magnitude across all transfer function results. The cubic orders do not exhibit this behaviour in general; the only one to keep this is the numeric Taylor map. Therefore it seems that the focusing does not depend on the direction of integration of the fringe field.

The biggest coefficients are in the odd orders (linear, cubic, quintic) and the zeroth, second, and fourth orders are comparatively much smaller. This could be explained by the observation that a transfer function is expected to be an odd function and therefore the odd polynomials should dominate. The lower order polynomial terms are useful for fitting real data that is not perfectly aligned at the origin.

It should be noted that there are several features of the fit results that may require further probing to explain their cause. For instance, although the quintic coefficients of the numeric field and Enge field Taylor map cases are in good agreement, the magnitude of the quintic coefficients of the Runge-Kutta cases are not in agreement with the Taylor map cases or each other.

Additionally, in the Runge-Kutta cases there appears to be a symmetry in the fifth (p_1) and third (p_3) order polynomial coefficients when interchanging the focusing type, $F \Leftrightarrow D$, and interchanging the horizontal and vertical phase space, $(x, p_x) \Leftrightarrow (y, p_y)$.

Furthermore, the numeric Runge-Kutta is the only case for which the quintic orders are of similar magnitude between the F-Entrance-Horizontal and F-Entrance-Vertical.

For all other cases the F-Entrance-Horizontal is greater than the F-Entrance-Vertical. Finally, the numeric Taylor map is the only case for which the cubic coefficients have a smaller magnitude for the F-Entrance-Horizontal than the F-Exit-Horizontal. The reason for these discrepancies is unclear.

5.3 Chromaticity

The chromaticity of a lattice is a property that defines the change in tune depending on the change in the energy deviation from the reference momentum of a test particle [1]. The change in tune ν is due to the difference in focusing strength for particles with differences in energy deviation with respect to the reference momentum. The result is that particles of different energies are focused by differing amounts as they traverse a quadrupole field. Chromaticity is so called because this effect is analogous to visible light being split into different frequencies of light by a prism.

The chromaticity can be measured by taking into account either the change in horizontal or vertical tune of the particles to produce what is referred to here as the horizontal chromaticity or vertical chromaticity.

The chromaticity investigation was conducted using the four fringe field models, numeric (N) or Enge (E) field using either a Taylor map (TM) or Runge-Kutta (RK) integration. In addition to these four fringe field models (abbreviated as NTM, ETM, NRK, ERK) is the nominal case which has no fringe fields.

The fringe fields are added to the entrance and exit of each of the inner triplet quadrupoles around the interaction points IP1 and IP5 in the HL-LHC lattice. Every fringe field model inserted into the lattice is accompanied by a transfer map representing the inverse of the linear part of the fringe field. This is done to remove additional focusing contributions from the quadrupole fringe field. The fringe field is also accompanied by drift spaces which are needed to position the fringe field at the end of the hard edge model. More information about the method of adding fringe fields to the lattice can be seen in section 4.2.2.

The addition of fringe fields modifies the chromaticity of the lattice. This change in chromaticity is still seen even if the fringe field is accompanied by a retuning element. Therefore, it is necessary to correct the chromaticity. The details of the chromaticity restoration technique used for these results are described in section 4.2.3. In short, a root finding algorithm was chosen to minimise the difference between the horizontal chromaticity of a modified HL-LHC lattice, (with or without fringe fields) calculated by SAMM, and the horizontal chromaticity of the HL-LHC v1.0 as calculated by MAD-X. The difference in the chromaticities was used to scale the field strength of each sextupole in the lattice.

To produce the results shown below, the tune, ν, was calculated numerically by tracking particles over 1024 turns and then computing the tune using a NAFF algorithm (see section 4.3.2). The number of turns was chosen based on how other studies calculate the

[1] Remember that the energy deviation δ is a property that is related to the reference momentum of the particle, and is more convenient to work with than the longitudinal momentum itself. See 3.2.4 for more details.

Magnet model and integrator	p_1	p_2	p_3	R^2	Difference from MAD	Percent
Chromaticity from MAD	-	*2.038E+00*	-	-	*0.000E+00*	*0.00*
No fringe case	2.131E+03	1.993E+00	3.095E-01	1.000E+00	-4.581E-02	-2.30
Numeric Taylor map	2.512E+03	1.987E+00	3.096E-01	1.000E+00	-5.158E-02	-2.60
Numeric Runge-Kutta	2.359E+03	2.141E+00	3.089E-01	1.000E+00	1.026E-01	4.79
Enge Taylor map	2.572E+03	2.096E+00	3.100E-01	1.000E+00	5.777E-02	2.76
Enge Runge-Kutta	2.525E+03	2.087E+00	3.095E-01	1.000E+00	4.831E-02	2.32

TABLE 5.5: Table of fit coefficients for the horizontal chromaticity results. The MAD chromaticity result is included to provide a comparison.

tune for frequency map analysis. In frequency map analysis the tune is calculated for two equally sized partitions of turns. For example in other literature, turn numbers of the order of 1000 turns are used [23]. It is therefore expected that 1024 turns will be sufficient for a precise tune calculation. Figure 5.8a shows the horizontal chromaticity of the four fringe field models: numeric field Taylor map, Enge field Taylor map, numeric field Runge-Kutta, Enge field Runge-Kutta, as well as the no fringe case. Figure 5.8b shows similar plots but for the vertical chromaticity.

The numeric field Runge-Kutta and Enge field Taylor map cases exhibit the largest tune shifts at zero. In both the horizontal and vertical cases two of the results are in closer agreement with the no fringe model: these are the numeric field Taylor map (NTM) and the Enge field Runge-Kutta (ERK). The other two fringe field models, the numeric field Runge-Kutta (NRK) and the Enge field Taylor map (ETM), have bigger tune shifts at $\delta = 0$ compared to the no fringe model. The tune shift therefore is not correlated based on the choice of integration method, Runge-Kutta or Taylor map, or the choice of fringe field model, numeric field or Enge field. This supports the idea that the tune shift is introduced independent to the field model or integrator. How this tune shift is introduced requires further investigation.

The table of fit coefficients can be seen in tables 5.5 and 5.6. The p_i coefficients correspond with the coefficients of the quadratic fit (eq. (5.3)), and R^2 is the R-squared statistic. The R-squared returned is used as an indicator of goodness of fit. A value of R-squared closer to one might suggest that the fit is a good predictor the data that it has been fit against. R-squared was calculated using Matlab's fit function [47].

As can be seen from the the R^2 values in table 5.5 the horizontal chromaticity results are approximated very well by the quadratic polynomial fit.

To recap, the first order chromaticity, Q', is defined as the change in tune for a change in energy deviation at an energy deviation of zero. This is the gradient at $\delta = 0$ of the plots in figs. 5.8a and 5.8b. The gradients can be found numerically using the following quadratic fit:

$$f = p_1 x^2 + p_2 x + p_3 \,. \tag{5.3}$$

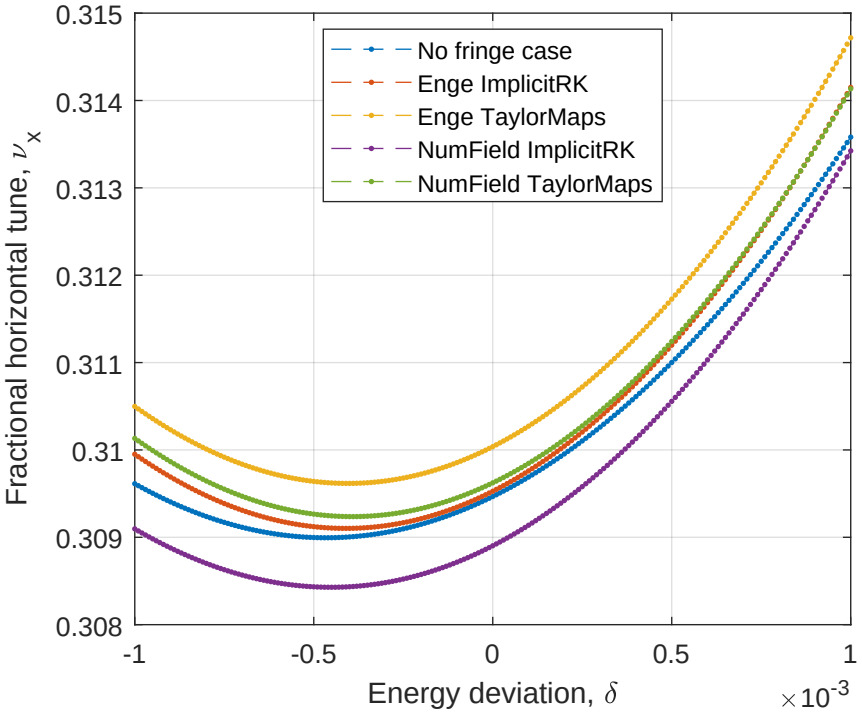

(A)

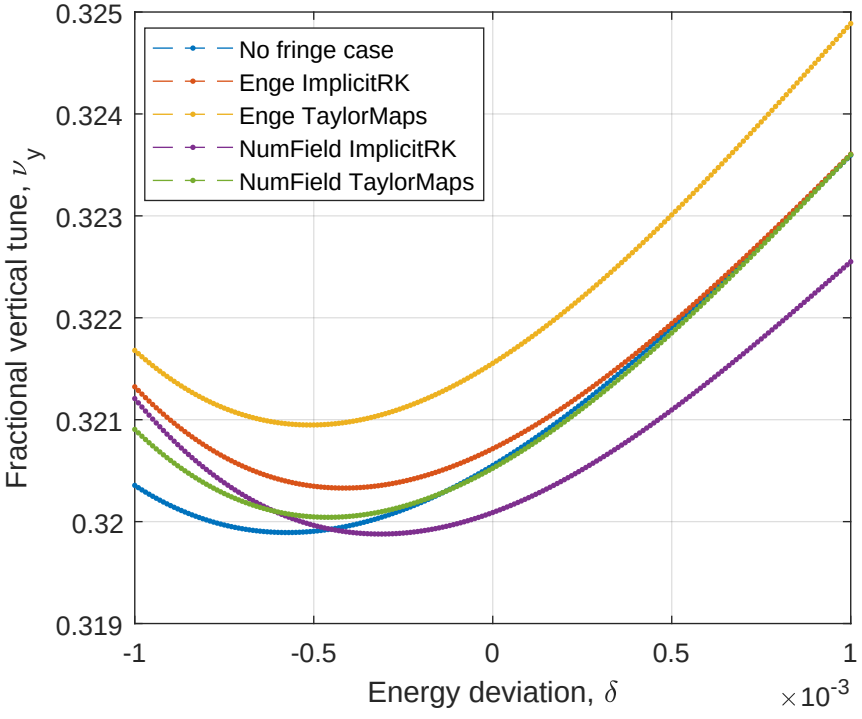

(B)

FIGURE 5.8: The tune of a particle with respect to its deviation from the reference energy (chromaticity), for different fringe field models, in the: (a) horizontal and (b) vertical phase space. The different fringe field models are for the Taylor maps/implicit Runge-Kutta integrators using the analytic/numeric fields, as well as the case of no fringe field.

Magnet model and integrator	p_1	p_2	p_3	p_4	p_5	R^2	Difference	Percent
Chromaticity from MAD	-	-	-	*2.004E+00*	-	-	*0.000E+00*	*0.00*
No fringe case	1.831E+07	-5.007E+05	1.406E+03	2.122E+00	3.206E-01	1.000E+00	1.180E-01	5.56
Numeric Taylor map	3.742E+07	-6.071E+05	1.692E+03	1.956E+00	3.205E-01	1.000E+00	-4.738E-02	-2.42
Numeric Runge-Kutta	3.694E+07	-6.129E+05	1.752E+03	1.285E+00	3.201E-01	1.000E+00	-7.186E-01	-55.92
Enge Taylor map	3.732E+07	-6.086E+05	1.693E+03	2.213E+00	3.216E-01	1.000E+00	2.098E-01	9.48
Enge Runge-Kutta	3.645E+07	-6.069E+05	1.712E+03	1.749E+00	3.207E-01	1.000E+00	-2.549E-01	-14.58

TABLE 5.6: Table of fit coefficients for the vertical chromaticity results determined by SAMM for different lattice configurations. The chromaticity result calculated using MAD is included to provide a comparison.

As with the horizontal chromaticity, the same method was applied for the vertical phase space. The vertical chromaticity, Q'_y, is therefore the change in vertical tune, ν_y, for a given change in energy deviation, δ.

The results of the fits applied in the vertical case are shown in table 5.6. There is one key difference between the horizontal and vertical cases in terms of calculating the chromaticities. It was found that for the vertical case a quadratic polynomial was underfitting the data. The next step was to increase the polynomial to the next even order of fourth. The fourth order polynomial was observed to be a better approximation of the results. The R^2 values from the vertical chromaticity fit show that the fourth order fit does indeed approximate the tracking result data well. The equation of fit for the vertical chromaticity as follows:

$$f = p_1 x^4 + p_2 x^3 + p_3 x^2 + p_4 x + p_5 \,. \tag{5.4}$$

The HL-LHC lattice model used in this study was the HLLHCV1.0 lattice. The chromaticity values calculated by MAD-X for this lattice are $Q'_x = 2.038324162$ and $Q'_y = 2.003656081$. The horizontal p_2 values from the fit show that the chromatic restoration technique by retuning sextupoles has brought the chromaticity values to within 5% of the MAD chromaticity values. In fact most of the horizontal chromaticity values are within 3% of the MAD value. The numeric field Runge-Kutta has the largest difference to MAD (at 5%). It is not clear why the numeric field Runge-Kutta has a larger discrepancy in the horizontal chromaticity compared to the other fields and integrator models. The discrepancies in the horizontal chromaticity show that the method of sextupole retuning is limited.

Table 5.7 shows the retuning values for each of the fringe field models. The first MS lattice sextupole in the lattice was chosen and its sextupole field component was compared between the HL-LHC lattice that had not undergone the chromaticity restoration procedure, against the lattice with different fringe field models that had chromaticity restoration applied. The chromaticity calculated for the no fringe field case was in good agreement between the MAD and SAMM values. It can be expected that the chromaticity values will not be the same because both codes model the magnetic elements, and chromaticity finding algorithms using independent implementations. Therefore as can be expected

Magnet model and integrator	Retuning factor	Sextupole field coefficient of MS.11R3.B1 (Tm^{-2})
No fringe case (no correction)	1.0000	631.655
No fringe case	1.0003	631.827
Numeric Taylor map	1.0831	684.127
Numeric Runge-Kutta	1.0849	685.275
Enge Taylor map	1.0855	685.688
Enge Runge-Kutta	1.0863	686.151

TABLE 5.7: The retuning factor values for each fringe field case.

the change in sextupole strength, needed to restore the chromaticity, is small. The other fringe field cases have an average retuning factor of 1.0849 with a standard deviation of 0.0014. There is no major discrepancy in the chromaticity retuning values when the fringe fields, using any model, are inserted into the HL-LHC.

The vertical p_4 values from the fit show that the chromaticity restoration is significantly less effective at bringing the vertical chromaticity towards the MAD value. Only one model, the numeric field Runge-Kutta, is within 5% of the MAD value, most of the cases are within 15% of the MAD value. Meanwhile the numeric field Runge-Kutta has a 55.9% difference to the MAD value. As the chromatic restoration algorithm is only concerned with bringing the horizontal chromaticity closer to the MAD value, it could be expected that the vertical cases would exhibit larger differences compared with the horizontal cases.

Because the chromatic restoration works by minimizing the difference in horizontal chromaticity, possibly a better chromatic restoration scheme would minimise the differences of the calculated horizontal and vertical chromaticities with the MAD values in quadrature. This method would no longer be a root finding method and would have the disadvantages of minimisation algorithms. For example, the minimisation algorithm might find local minima instead of global minima, and the algorithm could take a longer amount of calculation time to find its solution due to having a bigger problem space.

Two or more sextupole families are required to correct both the calculated horizontal and vertical chromaticities [3]. The current restoration takes advantage of the families already in the HL-LHC. There are 4 families of the MS lattice sextupoles [1]. The MS sextupoles are used to correct chromaticity changes introduced from the inner triplet magnets [1]. In the chromaticity correction used in this study, for simplicity the sextupole strength of every sextupole, no matter the family, is modified by the same magnitude.

The LHC design report [1] recommends that the change in chromaticity during collision must be within 1 unit, i.e. $|\Delta Q'| < 1$. It should be noted that the results in this study were within 1 unit, and the largest difference of -0.7186 was for the vertical chromaticity in the numeric field Runge-Kutta case.

5.4 Tune shift with amplitude

As discussed in the theory section (section 3.1.7) quadrupole fringe fields introduce nonlinear effects on beams transported through the field. One notable nonlinear effect is the change in betatron oscillation depending on the transverse offset from the closed orbit. This effect is also known as tune shift with amplitude [48, Lecture 7].

The tune shift with amplitude investigation was done for the four fringe field models, numeric or Enge field using a Taylor map or Runge-Kutta integration. These four fringe field models are compared to the nominal case which has no fringe fields.

The fringe field were added to the lattice using the same method as for the chromaticity results (see section 5.3). To recap, fringe fields are added to entrance and exit of each of the inner triplet quadrupoles around the interaction points IP1 and IP5 in the HL-LHC lattice. The fringe fields are accompanied by a linear inverse map component to remove linear dynamic effects as well as drift spaces for positioning (see section 4.2.2).

There was a chromatic restoration applied to each lattice to bring the chromaticity closer to the value calculated by MAD. This chromatic restoration method was also implemented in the same way for the chromaticity results.

The tune, ν, is calculated numerically by tracking particles over 1000 turns and then computing the tune using a NAFF algorithm. The total number of turns was chosen, as for the argument given in the chromaticity results, because other studies use a similar number of turns using NAFF to calculate the tune.

Figure 5.9a shows the results for the four field models plus no fringe case for horizontal offsets from the closed orbit. It is evident that there is good agreement between the cases, apart from the numeric field Runge-Kutta which needs further investigation. The sharply changing notches on the tune line (seen on the left of the graph) are where the particles cross a resonance in tune space. This effect is more clearly visualised in the latter Frequency Map Analysis section, where the tune space plots show the distortion of the particle spread near resonant tune lines.

The numeric field Runge-Kutta has an opposite tune shift with amplitude compared to the other cases. This could be a result of the transfer function for the numeric field Runge-Kutta having an opposite sign for the fifth order polynomials contrary to the other cases. If the nonlinearity for the numeric field Runge-Kutta is opposite to that of the other cases, it is possible that this would translate into an opposite tune shift with amplitude. Another possibility is that the chromatic restoration method is producing different outcomes for the numeric field Runge-Kutta.

The numeric field Runge-Kutta and Enge field Taylor map have the largest tune shifts at zero.

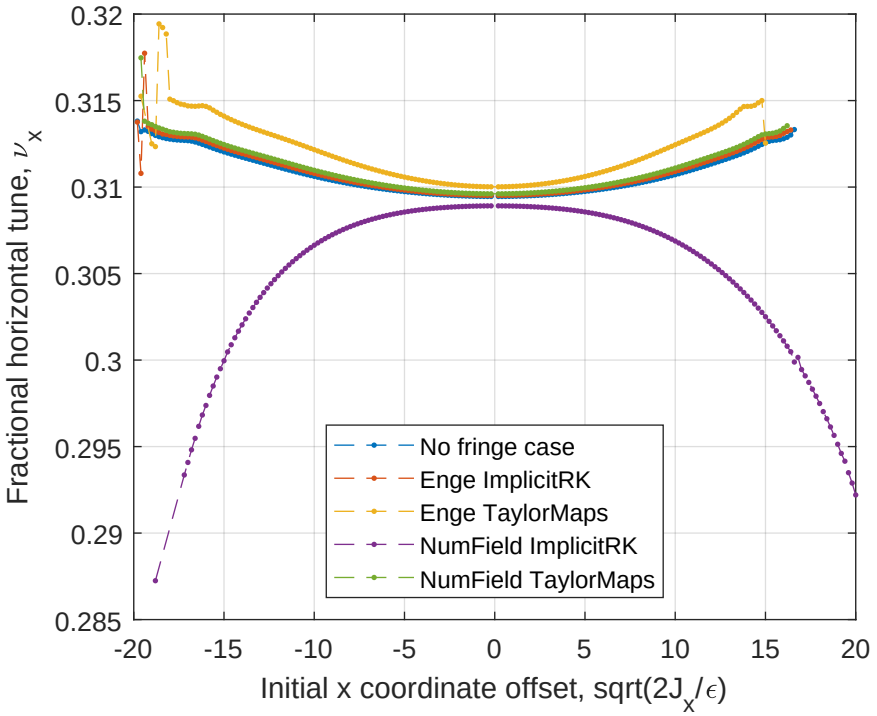

(A)

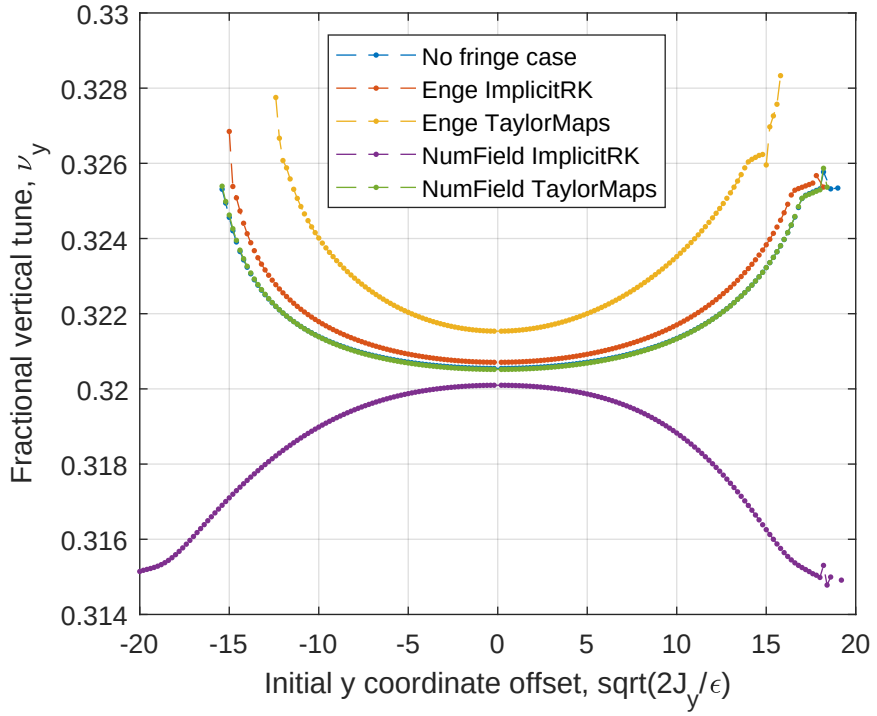

(B)

FIGURE 5.9: The tune of a particle with respect to its deviation from the closed orbit, for different fringe field models, in the: (top) horizontal and (bottom) vertical phase space. The different fringe field models are for the Taylor maps/implicit Runge-Kutta integrators using the analytic/numeric fields, as well as the case of no fringe field.

Field model and integrator	p_1	p_2	p_3	p_4	p_5	R^2	Difference	Percent
Tune from MAD	-	-	-	-	*3.100E-01*	-	*0.000E+00*	*0.00*
No fringe case	-3.120E-09	9.470E-08	1.310E-05	-5.130E-06	3.094E-01	9.975E-01	-5.890E-04	-0.19
NumField TaylorMaps	-1.680E-10	8.760E-08	1.380E-05	-1.230E-06	3.096E-01	9.630E-01	-3.854E-04	-0.12
NumField ImplicitRK	-1.070E-07	7.080E-07	-1.030E-05	-5.950E-05	3.089E-01	9.981E-01	-1.120E-03	-0.36
Enge TaylorMaps	-2.130E-08	3.670E-08	2.490E-05	1.190E-05	3.100E-01	8.829E-01	-7.961E-06	0.00
Enge ImplicitRK	-4.340E-09	8.760E-08	1.430E-05	-3.110E-06	3.095E-01	9.189E-01	-5.228E-04	-0.17

TABLE 5.8: Table of fit coefficients for the horizontal tune shift with amplitude results. The MAD tune result is included to provide a comparison.

Field model and integrator	p_1	p_2	p_3	p_4	p_5	R^2	Difference	Percent
Tune from MAD	-	-	-	-	*3.200E-01*	-	*0.000E+00*	*0.00*
No fringe case	4.340E-08	-2.360E-07	4.190E-06	2.040E-05	3.206E-01	9.847E-01	5.422E-04	0.17
NumField TaylorMaps	4.890E-08	-2.430E-07	3.210E-06	1.990E-05	3.206E-01	9.902E-01	5.418E-04	0.17
NumField ImplicitRK	-1.330E-09	-6.380E-08	-1.480E-05	-5.140E-06	3.202E-01	9.906E-01	2.283E-04	0.07
Enge TaylorMaps	7.070E-08	-6.810E-07	1.580E-05	3.030E-05	3.216E-01	9.897E-01	1.547E-03	0.48
Enge ImplicitRK	4.870E-08	-3.390E-07	5.740E-06	2.730E-05	3.207E-01	9.807E-01	7.126E-04	0.22

TABLE 5.9: Table of fit coefficients for the vertical tune shift with amplitude results. The MAD tune result is included to provide a comparison.

The tune shift with amplitude for the Enge field with the octupole ($m = 4$) field results in points of inflection compared to the field without the $m = 4$ term.

The tuneshift with amplitude can be described the following simple model:

$$\nu(J) = \nu_0 + \nu_1 \cdot J + \nu_2 \cdot J^2 + \nu_3 \cdot J^3 \ldots , \tag{5.5}$$

where ν is the tune, J is the action of a particle (related to its amplitude), and $\nu_{n=0,1,2,3,...}$ are the coefficients on the tune of the different orders of action. This simple model has the form of a polynomial. The coefficient terms $\nu_{n=0,1,2,3,...}$ are related to the quadrupole term, octupole term and so on.

As the simplified model dictates, the octupole has a significant effect through ν_1. It is also likely that the higher order terms ($m = 8$ and $m = 10$) would also have an effect and could possibly bring the Enge field Runge-Kutta back into agreement.

The tune shift results can be fitted and this data can be seen in tables 5.8 and 5.9.

5.5 Frequency map analysis

Frequency map analysis, as previously discussed in the section 4.3.5, is a method to identify potentially unstable regions of the beam in both frequency space (also known as tune space) or amplitude space. To recap, one particular advantage of this technique is that the beam is simulated for a comparatively smaller amount of time as compared to survival studies involving orders of magnitude more beam time [24]. Survival studies require upwards of 1×10^6 turns [49]. In this study the frequency map analysis is calculated over 2000 turns for 10000 (100^2) particles per model.

One key difference between each model used in the frequency map analysis, is that the initial coordinate offset from the closed orbit is dependent on the particles emittance, ϵ, because of $\sqrt{(2J_{x,y}/\epsilon)}$. The emittance is calculated independently for each model. Furthermore the closed orbit is also calculated independently. Therefore for a given offset (a multiple of beam size), the initial coordinates of the particles is model dependent, because the beam size is also model dependent.

Frequency map analysis uses the Numerical Analysis of Fundamental Frequencies algorithm (NAFF) to calculate the tune of each particle. The tracking data is partitioned into two, and the tune of both halves is calculated. The tune diffusion rate is a quantity that characterises the change of the tunes. The tune diffusion is calculated using [25]:

$$\boldsymbol{D} = \boldsymbol{\nu}_{[T_1,T_2]} - \boldsymbol{\nu}_{[T_2,T_3]}\,, \qquad \text{(4.25 revisited)}$$

where $\boldsymbol{\nu}_{[T_1,T_2]}$ is a two-dimensional vector of the horizontal and vertical tunes calculated by NAFF between turn number T_1 and T_2. Particles that are more stable are thought to have a smaller tune diffusion [25].

The set of frequency maps, in amplitude and tune space, for the four different fringe field models as well as the case of no fringe field model is shown in figs. 5.10 to 5.19. Particles have an initial position in a grid spaced across x and y up to a multiple of twenty beam sizes away from the closed orbit. As with the tune shift with amplitude results (section 5.4), the notation used here is $\sqrt{(2J_{x,y}/\epsilon)}$ for either the horizontal x or vertical y offset.

The theory behind the tune shift with amplitude and resonances, which are fundamental components of frequency map analysis, was described previously in section 3.2.12. To restate, lattices can be designed in such a way that the working point of the lattice (the tune for a particle on the closed orbit) is chosen to be far away from problematic resonances. This is because particles that have a tune close to a resonance can become unstable, and thus the particle can be lost.

Model	Energy deviation	Amplitude estimate at 0°	Amplitude estimate at 90°
None	Neg	17.8	18.2
None	Zero	16.6	18.0
None	Pos	15.4	17.6
Enge RK	Neg	17.0	17.2
Enge RK	Zero	16.4	17.8
Enge RK	Pos	14.6	17.0
Enge TM	Neg	16.2	15.6
Enge TM	Zero	15.0	15.8
Enge TM	Pos	13.7	15.4
Simulated RK	Neg	20.0	20.0
Simulated RK	Zero	20.0	18.6
Simulated RK	Pos	19.6	20.0
Simulated TM	Neg	17.4	18.2
Simulated TM	Zero	16.4	18.2
Simulated TM	Pos	15.0	17.8

TABLE 5.10: An estimate of the dynamic aperture for each of the frequency map analysis results, of a given model and energy deviation. The estimate is of the greatest amplitude for which particles on the x-axis or y-axis.

Despite the choice of a working point far away from resonances, the tune shift with amplitude can result in particles having a tune close to resonances. Frequency map analysis offers a way to estimate the strength of a resonance by observing how the smooth grid of particles is disrupted by a resonance. Frequency map analysis also allows the tune shift with amplitude to be visualised in a two dimensional tune space. By comparing tune space plots between different results one can see how the tune shift with amplitude differs by looking at the differences in shape and size of the spread of particles.

Looking at the tune space plots it can be seen that the working point is in good agreement across the results. The shape and size of the particle distribution in phase space for the numeric field Runge-Kutta case indicates that it has an tune shift with amplitude of opposite sign to the other results. This is in agreement with what was seen for the numeric field Runge-Kutta result from the tune shift with amplitude results (section 5.4) as expected.

Table 5.10 shows an estimate of the amplitudes of the particles, furthest from the closed orbit, that have survived for each of the frequency map results. The estimates are given for each of the fringe field models, and for each of the initial energy deviations. These results were taken by visually selecting points with the largest deviations from the closed orbit for $y = 0$ and for $x = 0$. Points were also selected based on their continuity with the rest of the data. For example, the no fringe field case with positive energy deviation has a singular point on the y-axis separated from the main body of data. In this case the plotting software gave the coordinates of extreme points to two decimal points, but the results were rounded to one decimal point as the method is only an estimate.

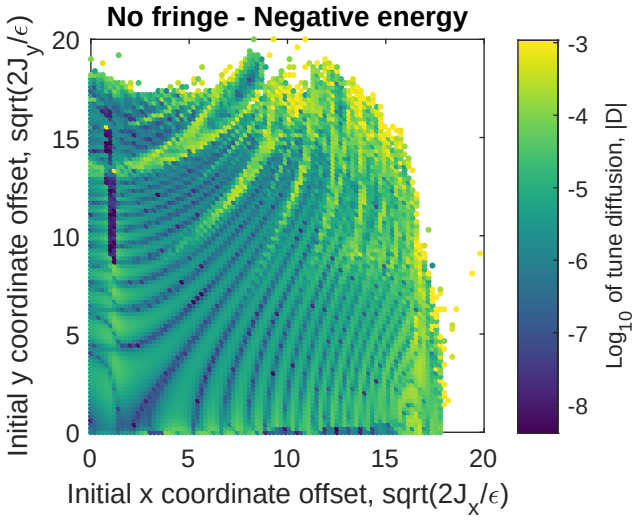

(A)

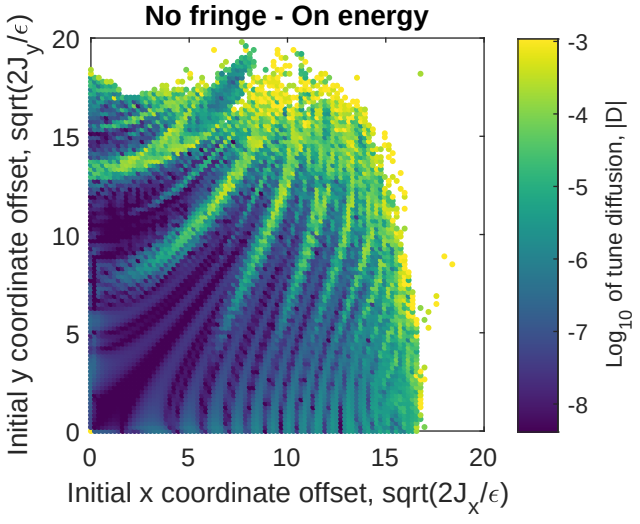

(B)

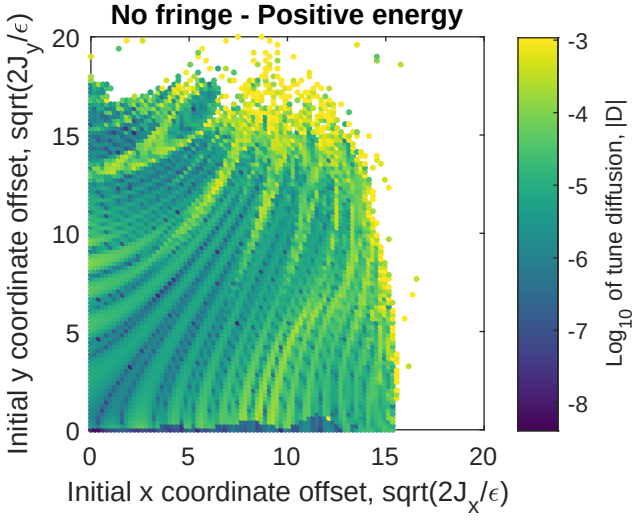

(C)

FIGURE 5.10: Frequency maps in amplitude space for the lattice without a fringe field. The tune diffusion rate is shown in relationship to particles different amplitudes from the closed orbit. The particles have different energy deviations from the reference energy; (a) negative energy deviation, (b) on reference energy, and (c) positive energy deviation.

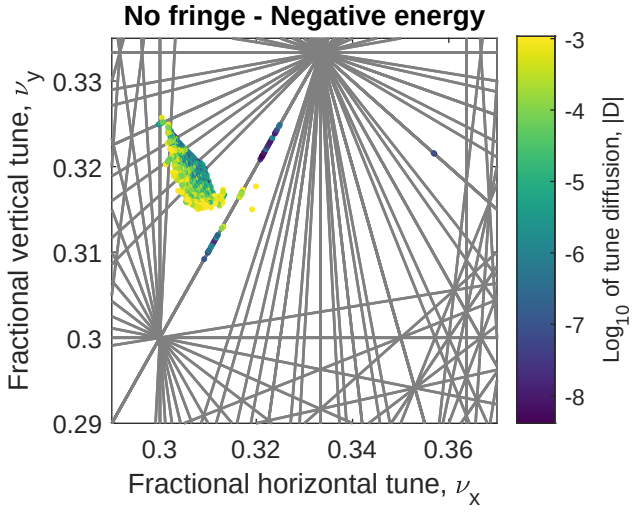

(A)

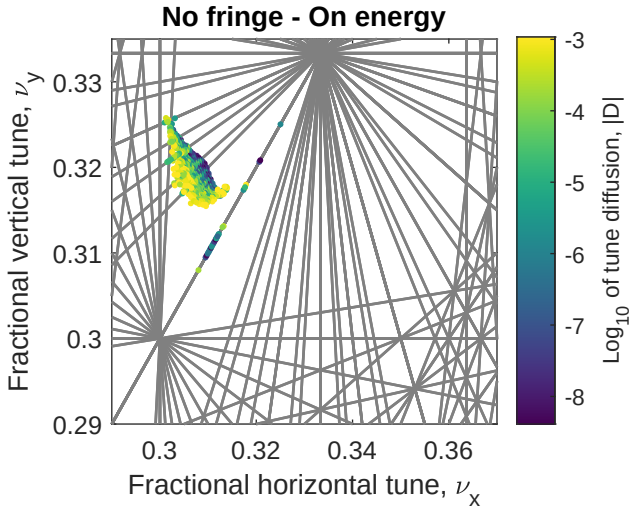

(B)

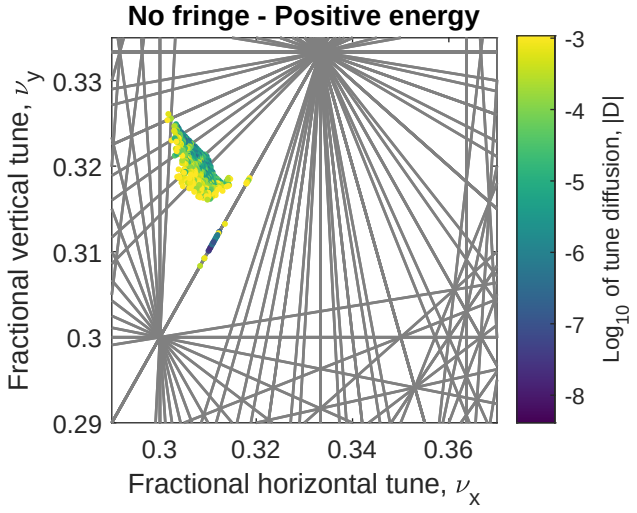

(C)

FIGURE 5.11: Frequency maps in tune space for the lattice without a fringe field model. The tune diffusion rate is shown in relationship to particles different amplitudes from the closed orbit. The particles have different energy deviations from the reference energy; (a) negative energy deviation, (b) on reference energy, and (c) positive energy deviation.

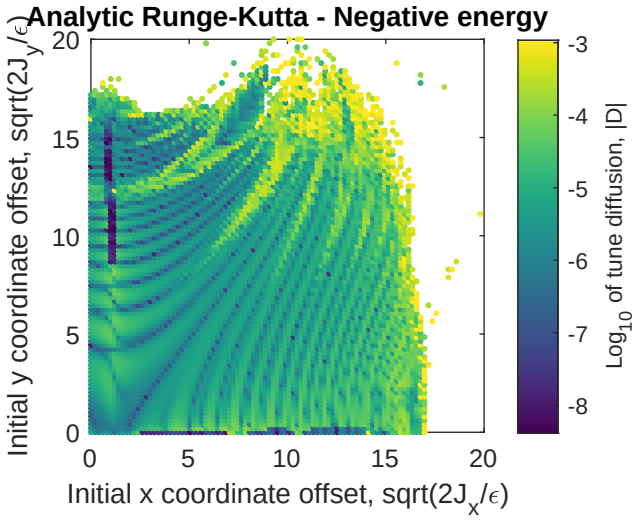

(A)

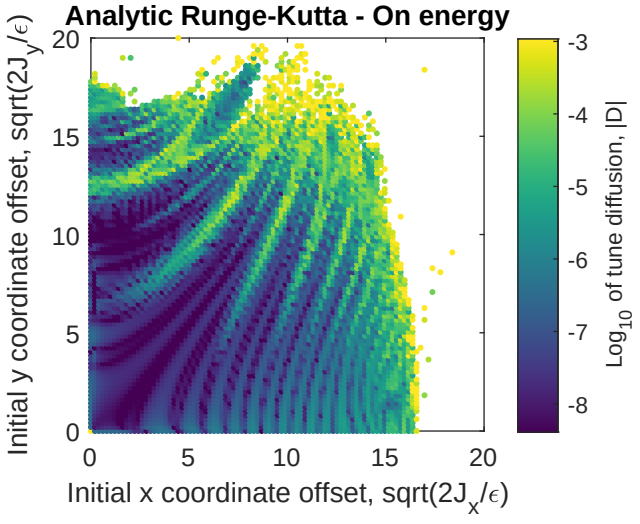

(B)

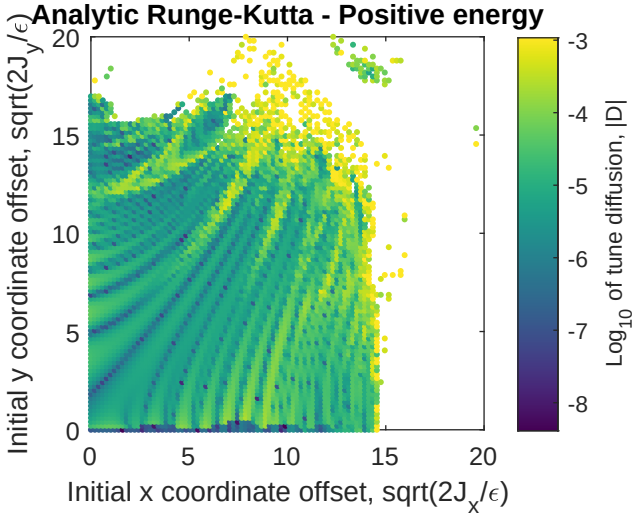

(C)

FIGURE 5.12: Frequency maps in amplitude space for the lattice with the analytic Runge-Kutta fringe field model. The tune diffusion rate is shown in relationship to particles different amplitudes from the closed orbit. The particles have different energy deviations from the reference energy; (a) negative energy deviation, (b) on reference energy, and (c) positive energy deviation.

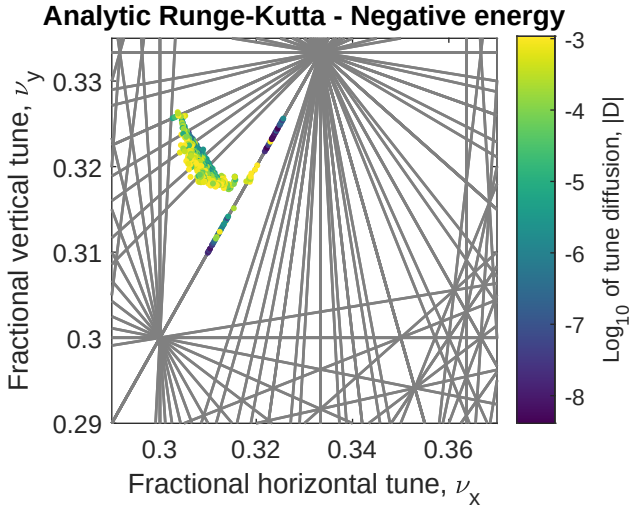

(A)

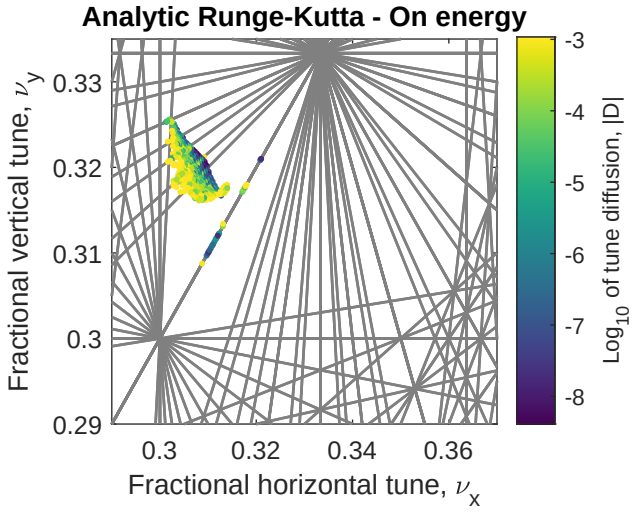

(B)

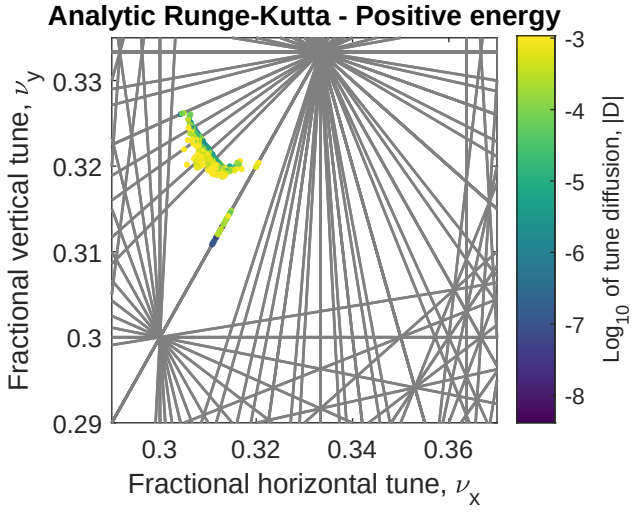

(C)

FIGURE 5.13: Frequency maps in tune space for the lattice with the analytic Runge-Kutta fringe field model. The tune diffusion rate is shown in relationship to particles different amplitudes from the closed orbit. The particles have different energy deviations from the reference energy; (a) negative energy deviation, (b) on reference energy, and (c) positive energy deviation.

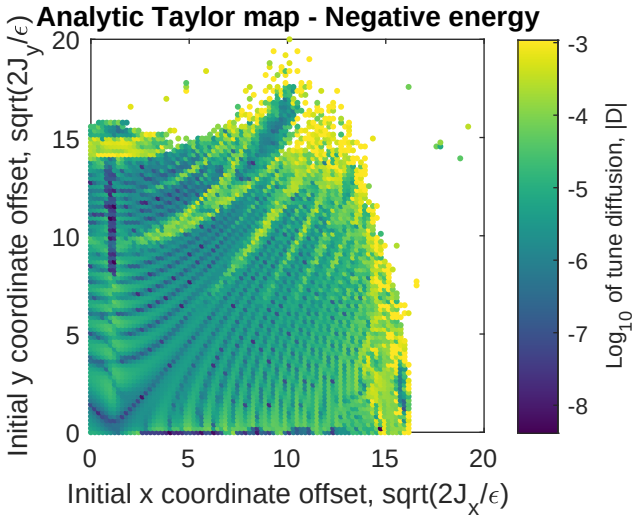

(A)

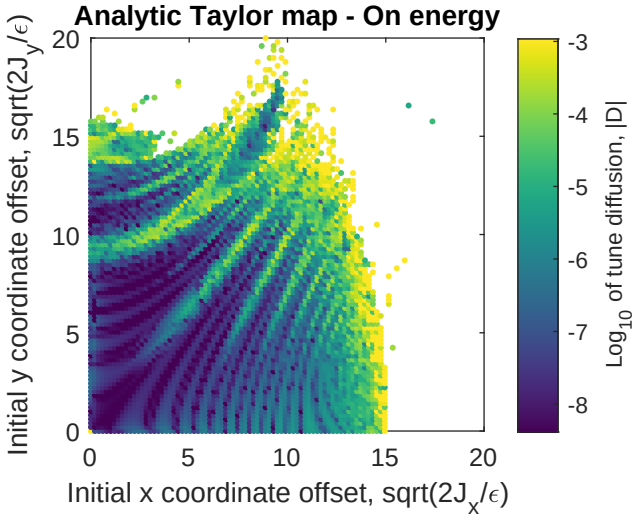

(B)

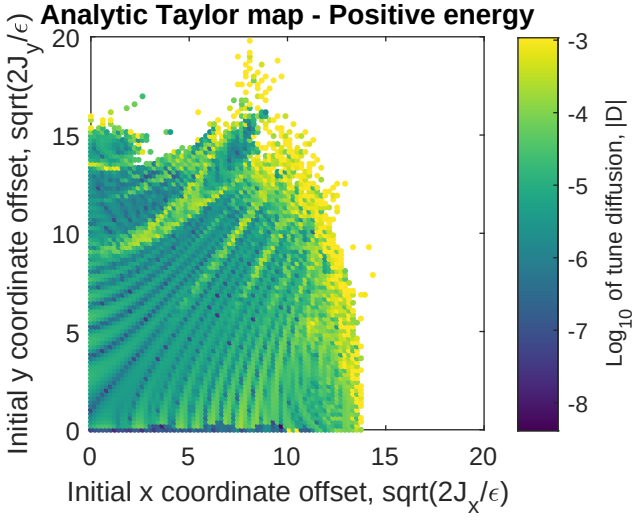

(C)

FIGURE 5.14: Frequency maps in amplitude space for the lattice with the analytic Taylor map fringe field model. The tune diffusion rate is shown in relationship to particles different amplitudes from the closed orbit. The particles have different energy deviations from the reference energy; (a) negative energy deviation, (b) on reference energy, and (c) positive energy deviation.

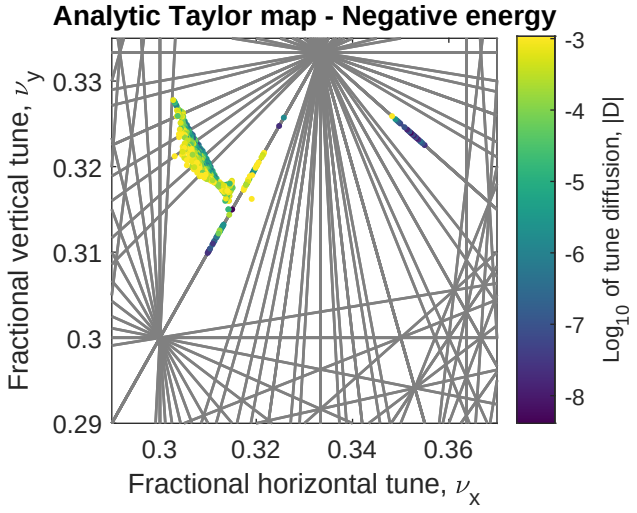

(A)

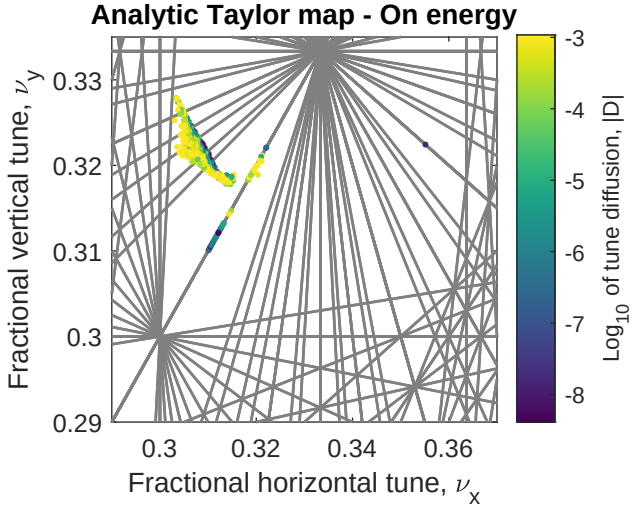

(B)

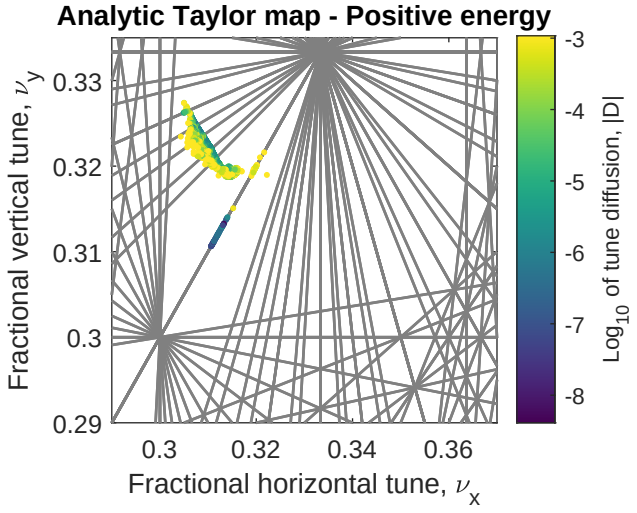

(C)

FIGURE 5.15: Frequency maps in tune space for the lattice with the analytic Taylor map fringe field model. The tune diffusion rate is shown in relationship to particles different amplitudes from the closed orbit. The particles have different energy deviations from the reference energy; (a) negative energy deviation, (b) on reference energy, and (c) positive energy deviation.

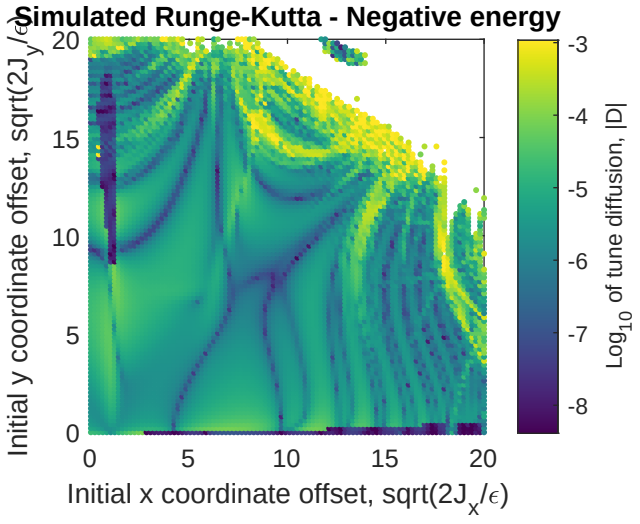

(A)

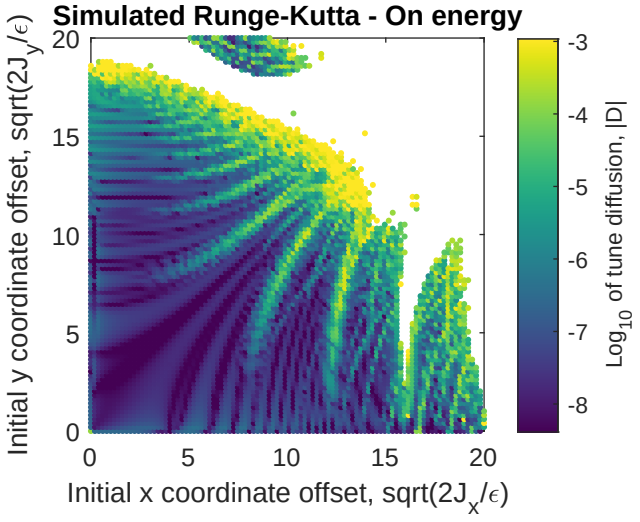

(B)

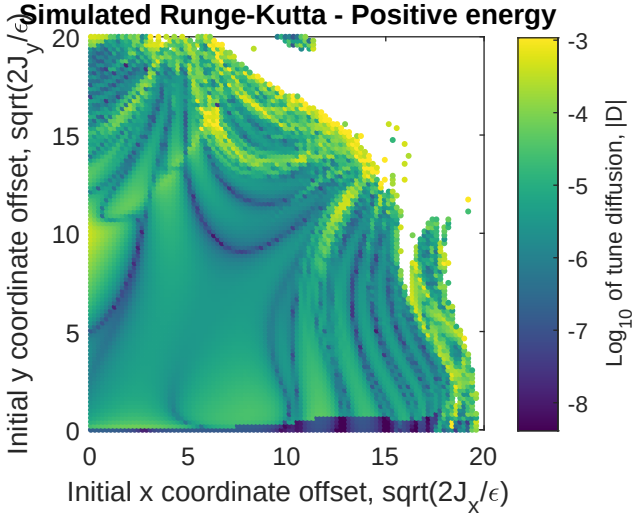

(C)

FIGURE 5.16: Frequency maps in amplitude space for the lattice with the simulated Runge-Kutta fringe field model. The tune diffusion rate is shown in relationship to particles different amplitudes from the closed orbit. The particles have different energy deviations from the reference energy; (a) negative energy deviation, (b) on reference energy, and (c) positive energy deviation.

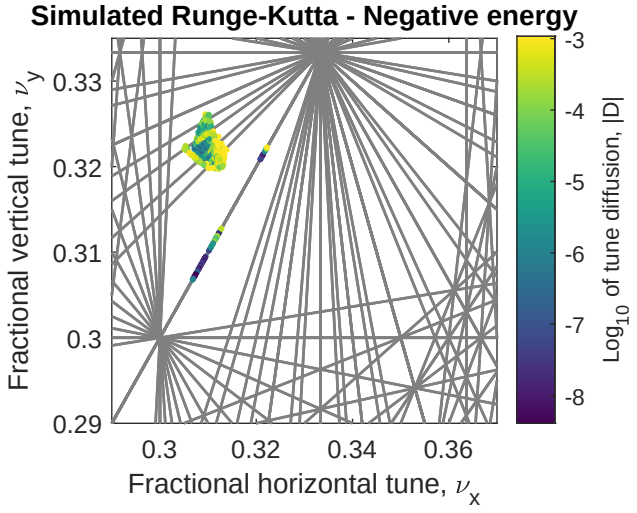

(A)

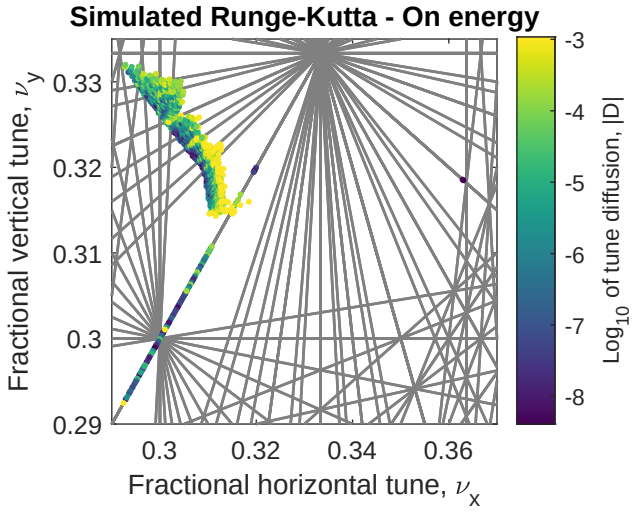

(B)

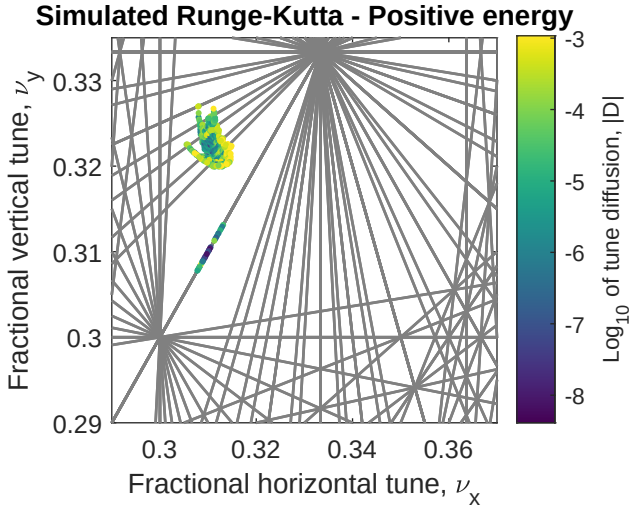

(C)

FIGURE 5.17: Frequency maps in tune space for the lattice with the simulated Runge-Kutta fringe field model. The tune diffusion rate is shown in relationship to particles different amplitudes from the closed orbit. The particles have different energy deviations from the reference energy; (a) negative energy deviation, (b) on reference energy, and (c) positive energy deviation.

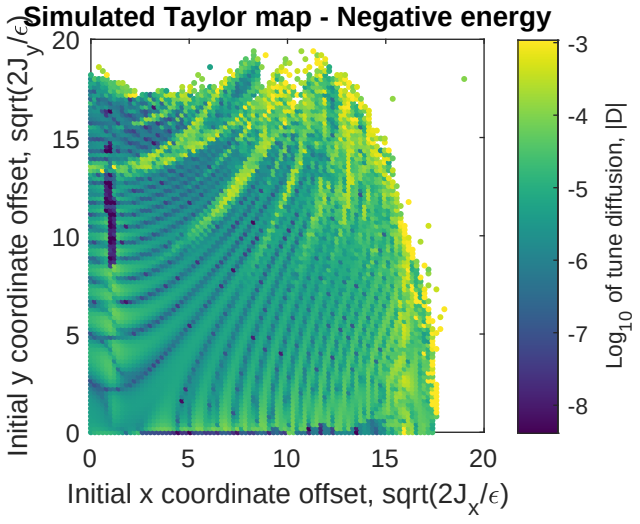

(A)

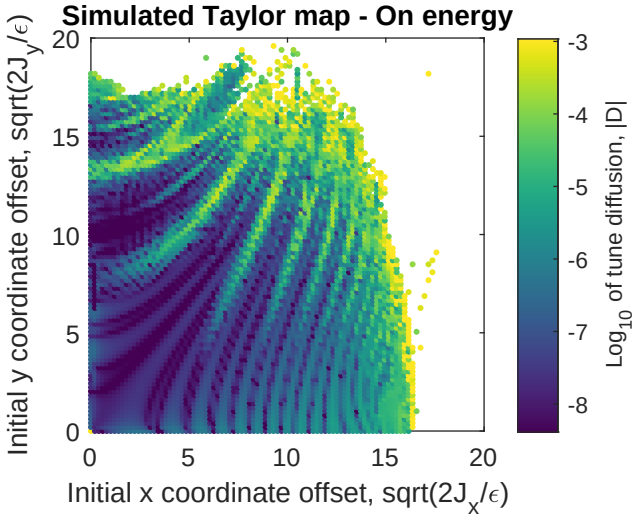

(B)

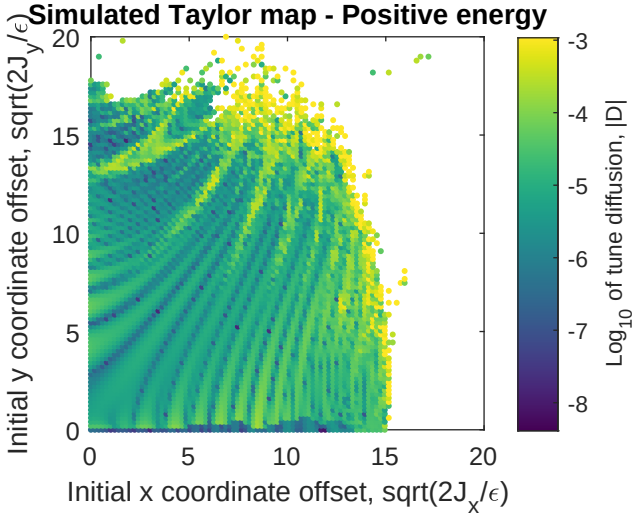

(C)

FIGURE 5.18: Frequency maps in amplitude space for the lattice with the simulated Taylor map fringe field model. The tune diffusion rate is shown in relationship to particles different amplitudes from the closed orbit. The particles have different energy deviations from the reference energy; (a) negative energy deviation, (b) on reference energy, and (c) positive energy deviation.

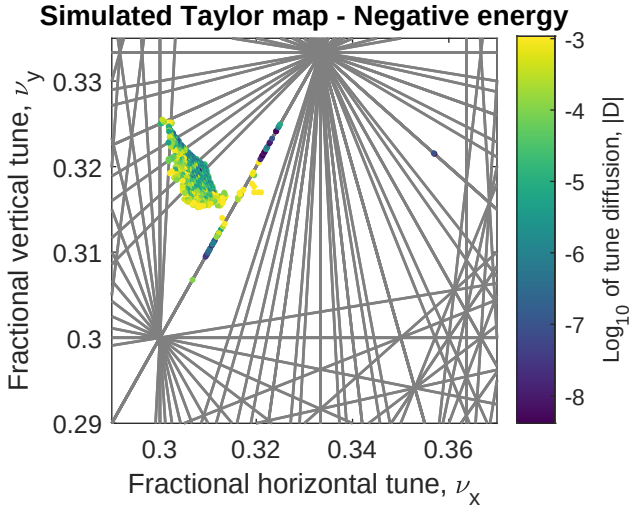

(A)

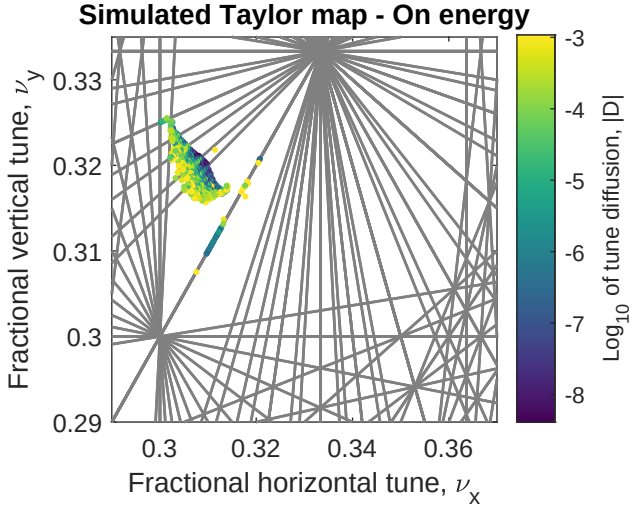

(B)

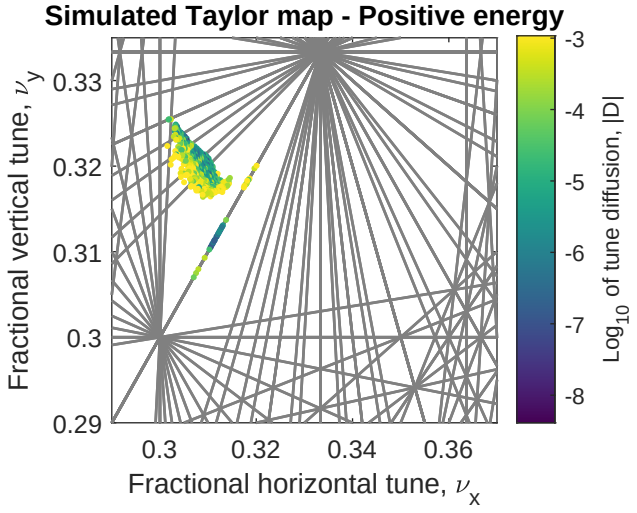

(C)

FIGURE 5.19: Frequency maps in tune space for the lattice with the simulated Taylor map fringe field model. The tune diffusion rate is shown in relationship to particles different amplitudes from the closed orbit. The particles have different energy deviations from the reference energy; (a) negative energy deviation, (b) on reference energy, and (c) positive energy deviation.

The characterisation of the estimate could be improved by using an algorithmic technique to find the contiguous limits of the phase space maps. A naive method for finding these results could be to test for contiguous points along $y = 0$, $x = 0$ lines and reporting the largest result. Such a method could be extended to look for contiguous points along a diagonal such as $x = y$. This method may be vulnerable to missing runs of particles along a line, and ignoring latter points that are in fact contiguous when considering the two-dimensional shape. A more advanced method may be to fit a boundary along the extremity of the continuous data. Any method that would try to determine the boundary would have to be robust to the sporadicly populated border region (seen in the upper right of Enge field Runge-Kutta plots fig. 5.12), as well as other features like islands (seen in numeric field Runge-Kutta plots fig. 5.16).

Instead of estimating the border between lost particles (those unbounded particles that travel outside some limit) and tracked particles, it might be of more use to find the dynamic aperture border. The dynamic aperture is the region of the beam in phase space for which particles are expected to have stable motion; particles outside this region might become lost due to chaotic motion [23]. More can be read about dynamic aperture (DA) in section 3.2.13.

There is an appearance of "fingers" of higher tune diffusion in the phase space plots. These fingers correspond with the particles that cross a resonance line as can be seen in the tune space plots. Some points get pulled on to the main linear resonance. This is also seen in other works, such as Laskar [24]. This means that the HL-LHC working point is in the neighbourhood of problematic resonances. As shown by the variety of different shapes and sizes of the particle distributions in tune space across the results, it is important to understand and control the contributions to tune shift with amplitude. This is because resonances experienced by particles is largely dictated by the tune shift with amplitude.

From the plots and from the estimates in table 5.10 it appears that there is the greatest dynamic aperture at a negative energy deviation. It gets smaller for zero energy deviation and then smaller again for positive energy deviation.

The plots and the estimates in table 5.10 also show that the particles appear to have a bigger limit of stability in the y-direction than the x-direction. That is to say that generally the edge of the limit is greater for $X - Y$ angle at 90° (y-axis) compared to 0°. The HL-LHC preliminary design report found that the dynamic aperture was greater for $X - Y$ angles at 0° and that it reduced with greater angle [2, Figure 2.5]. It should be noted that the preliminary design report result was found by plotting both the minimum and average dynamic apertures over $X - Y$ angle. It is possible that a similar result to the design report could be found if another set of magnetic field errors were applied to the lattice. It is also a possibility that the dynamic aperture does not correlate well with the limit of the amplitude space plots.

Chapter 6

Conclusions

6.1 Summary and conclusions

The main aim of this work was to identify if the fringe fields from the new inner triplet magnets would have a detrimental effect on the stability of the HL-LHC beam. Additional objectives were: to compare the Runge-Kutta and Wu-Forest-Robin Taylor map integration models against each other, to see in what circumstances the Enge field could be used in place of a numeric field and how they otherwise compare, and to perform a full frequency analysis in a timely manner on a single desktop computer by leveraging GPU computing.

In this study a comparison of four fringe field implementations using a choice of integration schemes (Wu-Forest-Robin truncated Taylor map or Runge-Kutta integrator), and a choice of fringe field models (numeric or Enge field) was conducted.

The magnetic field descriptions between the Enge field and the simulated numeric field agree closely, as can be seen in the plots of magnetic field (fig. 4.2), and in the plots of the generalised gradients generated from the field (figs. 5.1 to 5.3). This was expected following the results of the inner triplet magnet shown by Muratori et al. [5].

The generalised gradients start to differ due to high oscillatory behaviour for higher orders of l. This is likely due to the effect of repeated differentiation, as this is what each higher order of l represents [46]. The BlitzDA differential algebra code is only capable of generating generalised gradients with $m < 9$ and $l < 9$; if a higher order multipole or derivative term would impact the tracking results, then it would not be seen in this experimental setup.

The tune shift with amplitude has different results between the 5 fringe field models (including the no fringe model). Two of the models agree closely with the no fringe model: the numeric field Taylor map and the Enge field Runge-Kutta. The other two:

the numeric field Runge-Kutta and the Enge field Taylor map, diverge from the no fringe model. Whether a model agrees or diverges from the no fringe model does not correlate with either the field type (Enge or simulated numeric) or the integrator type (Runge-Kutta or Taylor map), but rather it suggests that there is an independent factor driving the tune shift with amplitude. Looking at the plots (fig. 5.9), it might be the case that the tune shift with amplitude is driven by the tune approaching zero amplitude deviation from the closed orbit.

From the chromaticity plots (fig. 5.8), it is clear that the chromaticity retuning has successfully brought the chromaticities into agreement with the no fringe field case.

The stability of the frequency map analysis appears to be most influenced by the tune shift with amplitude of the underlying model. It appears that the fringe field models can have a large impact on the stability of the beam; but as the results suggest, if the frequency map analysis is influenced by tune shift with amplitude (which could itself be influenced by an unknown independent variable) then more work needs to be done before a definitive conclusion can be made about the impact of the inner triplet fringe fields on beam stability in the HL-LHC.

The production of the results show that frequency map analysis can be performed on desktop computer hardware in a reasonable time with the assistance of GPU computation. The SAMM code is capable of being extended with new capabilities to track over interesting field models with bespoke integration routines. SAMM is also capable of being extended to perform additional processes such as chromaticity retuning. Additionally the BlitzDA code is capable of producing generalised gradients for the HL-LHC inner triplet quadrupole field.

6.2 Recommendations for further work

Further investigations to assess the difference in tune shift with amplitude between the four fringe field models are recommended. Whilst the Enge field Taylor map model has the largest reduction in the stable region of the beam (compared to the no fringe case), the simulated numeric field Runge-Kutta model has a marked increase in stability (compared to the no fringe case). Both of these models are the two that diverge the most, in terms of their tune shift with amplitude, from the others. It is likely that it is this difference in tune shift with amplitude that is driving the difference observed in stability. Because the tune shift with amplitude is independent of the underlying magnetic field model or integration routine - there is likely an independent factor which is governing the tune shift with amplitude and therefore likely having the biggest impact on differences in stability in the frequency maps between models.

The chromaticity retuning scheme could also be improved. Currently all the strengths of the sextupoles around the lattice are modified by the same factor to reach the chromaticity desired. The sextupoles in the HL-LHC are divided into families [1] and it is possible that the chromaticity could be brought more closely into line by tuning each of these families independently.

The generalised gradient description of the fields could be extended beyond the limits of multipole order $m < 9$ and l-order $l < 9$ that restrained this study. Higher orders would provide a more accurate description of the underlying field and could suggest if high order features in the magnetic field have an impact on the tracking results.

The Fourier transform used in the production of the generalised gradients could be replaced with a spline Fourier transform. A spline Fourier transform could offer a more accurate transform than the Fourier transform used when generating the generalised gradients [31].

The HL-LHC lattice has since been updated to a version known as HL-LHCv1.4 [50]. There have been incremental updates (v1.1, v1.2, v1.3) from the version used in this study HL-LHCv1.0 to v1.4 [28, 51, 52]. To best model what the effect of the fringe-fields would mean repeating this study on the latest lattice optics.

The simulated fringe field maps [35] could also be improved. The simulations could be performed to a higher resolution. The model of the magnet used to produce the simulation may have been refined since the production of the simulated data used in this study. Lastly the simulated data was restricted to one quadrant; this may have been desirable to reduce the simulation complexity. Although the one quadrant simulated data has to be reflected and transformed appropriately to generate a complete field, this has the effect of repeating noise with a 4-fold symmetry. This could mean that in the generalised gradient description which relies on multipoles, that noise would feature more prominently in lower multipoles. As the whole goal of using generalised gradients is to have a field description that is highly accurate, this repeated noise could be a feature that is reducing the accuracy. Therefore simulated fringe field data spanning four quadrants may offer more accurate results.

The fringe fields have been positioned at each end of the hard-edge model. When comparing a hard edge model with the true field, the hard-edge model would extend past where the true field starts to taper. This means that in order for the fringe fields to be positioned accurately, they should be placed in line with where the real field would taper. This position could be calculated by using an accurate integration of the quadrupole field strength of the fringe field, and then using that strength to place the fringe field more accurately using drifts.

6.3 Closing remarks

This work has shown that the inner triplet quadrupole fringe field models could potentially have a detrimental impact on the stability of the HL-LHC beam as evidenced by the reduction in the extent of the surviving particles in the Enge field Taylor map case compared with the no fringe case.

This study does not allow a definitive conclusion to be drawn on whether the fringe fields would have a detrimental impact on the stability of the beam. This is due to the fact that the four fringe field models differ largely in their tune shift with amplitude independent of the magnetic field model or integration routine.

Therefore further work is recommended to determine the cause of the different tune shift results between the different fringe field models.

List of Publications

1. S. Jones, D. Newton, and A. Wolski. *Initial Estimate of Fringe Field Effects in HL-LHC Using Frequency Map Analysis.* International Particle Accelerator Conference (IPAC'14), Dresden, Germany, June 2014. JACOW, Geneva, Switzerland 2014.

   `http://jacow.org/IPAC2014/papers/tupro025.pdf`

2. A. T. Herrod, S. Jones, A. Wolski et al. *Modelling of Curvilinear Electrostatic Multipoles in the Fermilab Muon g-2 Storage Ring.* International Particle Accelerator Conference (IPAC'17), Copenhagen, Denmark, May 2017. JACOW, Geneva, Switzerland 2017.

   `http://accelconf.web.cern.ch/AccelConf/ipac2017/papers/thpab055.pdf`

Bibliography

[1] L. Evans and P. Bryant. 'LHC Machine'. In: *Journal of Instrumentation* 3.8 (2008), S08001. ISSN: 17480221. DOI: 10.1088/1748-0221/3/08/S08001. URL: http://stacks.iop.org/1748-0221/3/i=08/a=S08001.

[2] The HiLumi LHC Collaboration. *HL-LHC Preliminary Design Report*. Tech. rep. CERN, 2014. URL: http://hilumilhc.web.cern.ch.

[3] H. Wiedemann. *Particle accelerator physics: Third edition*. Berlin, Heidelberg: Springer, 2007, pp. 1–948. ISBN: 9783540490432. DOI: 10.1007/978-3-540-49045-6. URL: http://link.springer.com/10.1007/978-3-540-49045-6.

[4] C. E. Mitchell and A. J. Dragt. 'Accurate transfer maps for realistic beam-line elements: Straight elements'. In: *Physical Review Special Topics - Accelerators and Beams* 13.6 (2010), p. 064001. ISSN: 10984402. DOI: 10.1103/PhysRevSTAB.13.064001. URL: http://link.aps.org/doi/10.1103/PhysRevSTAB.13.064001.

[5] B. D. Muratori, J. K. Jones and A. Wolski. 'Analytical expressions for fringe fields in multipole magnets'. In: *Physical Review Special Topics - Accelerators and Beams* 18.6 (2015), p. 064001. ISSN: 10984402. DOI: 10.1103/PhysRevSTAB.18.064001. arXiv: 1404.1762. URL: http://link.aps.org/doi/10.1103/PhysRevSTAB.18.064001.

[6] S. Kelly et al. 'Study of the Impact of Fringe Fields of the Large Aperture Triplets on the Linear Optics of the HL-LHC'. In: *Proceedings of IPAC2013* 1 (2013), pp. 2642–2644. URL: http://accelconf.web.cern.ch/AccelConf/IPAC2013/papers/wepea059.pdf.

[7] CERN - BE/ABP Accelerator Beam Physics Group. *MAD-X - Methodical Accelerator Design*. URL: https://madx.web.cern.ch/madx/ (Accessed: 28 Feb. 2019).

[8] S. Fartoukh and R. D. Maria. 'Optics and Layout Solutions for Hl-Lhc With Large Aperture Nb3Sn and Nb-Ti Inner Triplets *'. In: *Proceedings of IPAC2012*. 2012, pp. 4–6. ISBN: 9783954501151. URL: https://accelconf.web.cern.ch/accelconf/IPAC2012/papers/moppc011.pdf.

[9] R. de Maria, S. Fartoukh and A. Bogomyagkov. 'HLLHCV1.0: HL-LHC Layout and Optics Models for 150 MM NB3SN Triplets and Local Crab-Cavities'. In: *Proceedings of IPAC2013*. 2013. ISBN: 9783954501229. URL: https://cds.cern.ch/record/1581701.

[10] A. Wolski. *Beam Dynamics in High Energy Particle Accelerators*. Imperial College Press, 2014, p. 606. ISBN: 978-1-78326-277-9. DOI: 10.1142/p899. URL: http://www.worldscientific.com/worldscibooks/10.1142/p899.

[11] B. Dalena et al. 'Fringe Fields Modeling for the High Luminosity Lhc Large Aperture Quadrupoles'. In: *Proceedings of IPAC2014*. 284404. 2014, pp. 993–996. ISBN: 9783954501328.

[12] A. Bogomyagkov et al. 'Analysis of the Non-Linear Fringe Effects of Large Aperture Triplets for the HL-LHC Project'. In: *Proceedings of IPAC2013*. 2013, pp. 1–3. ISBN: 9783954501229. URL: http://cds.cern.ch/record/1591597.

[13] R. de Maria et al. 'Dynamic Aperture Studies for the Lhc High Luminosity Lattice *'. In: *Proceedings of IPAC2015*. 2015. ISBN: 9783954501687.

[14] A. Wolski. *Website of SAMM Tracking Code*. URL: http://pcwww.liv.ac.uk/~awolski/main_links_computercodes.htm (Accessed: 28 Feb. 2019).

[15] K. M. Hock, A. Wolski and R. B. Appleby. 'Applying the "Simple Accelerator Modelling in Matlab" (SAMM) Code To High Luminosity LHC Upgrade'. In: *Proceedings of IPAC2013*. 2013, pp. 2690–2692. ISBN: 9783954501229.

[16] E. Forest, F. Schmidt and E. McIntosh. *Introduction to the Polymorphic Tracking Code*. Tech. rep. CERN, 2002. URL: https://cds.cern.ch/record/573082/files/sl-2002-044.pdf.

[17] N. Phinney. *ILC Reference Design Report-Accelerator Executive Summary*. Tech. rep. SLAC. URL: http://tesla.desy.de..

[18] S. Jones, D. Newton and A. Wolski. 'Initial Estimate of Fringe Field Effects in HL-LHC Using Frequency Map Analysis'. In: *Proceedings of IPAC2014*. 2014, pp. 1067–1070. ISBN: 9783954501328. URL: http://jacow.org/IPAC2014/papers/tupro025.pdf.

[19] O. Karamyshev, D. Newton and C. Welsch. 'Optimization of Low Energy Electrostatic Beamlines'. In: *Proceedings of IPAC2014*. 2014, pp. 1202–1204. ISBN: 9783954501328.

[20] J. Resta-López et al. 'Beam Life Time and Stability Studies for Elena'. In: *Proceedings of IPAC2014*. 2014, pp. 154–156. ISBN: 9783954501328.

[21] A. T. Herrod et al. 'Modelling of Curvilinear Electrostatic Multipoles in the Fermilab Muon g-2 Storage Ring'. In: *Proceedings of IPAC2017*. 2017. URL: http://accelconf.web.cern.ch/AccelConf/ipac2017/papers/thpab055.pdf.

[22] R. Edgecock et al. 'EMMA -The World's first non-scaling FFAG'. In: *Proceedings of EPAC2008*. 2008, pp. 3380–3382. URL: https://accelconf.web.cern.ch/AccelConf/e08/papers/thpp004.pdf.

[23] Y. Papaphilippou. 'Detecting chaos in particle accelerators through the frequency map analysis method'. In: *Chaos: An Interdisciplinary Journal of Nonlinear Science* 24.2 (June 2014), p. 024412. ISSN: 1054-1500. DOI: 10.1063/1.4884495. arXiv: 1406.1545v1. URL: http://aip.scitation.org/doi/10.1063/1.4884495%20https://arxiv.org/pdf/1406.1545.pdf.

[24] J. Laskar. 'Frequency map analysis and particle accelerators'. In: *Proceedings of PAC2003*. Vol. 1. 2. 2003. ISBN: 0-7803-7738-9. DOI: 10.1109/PAC.2003.1288929. arXiv: 0305364 [math]. URL: http://arxiv.org/abs/math/0305364.

[25] Y. Papaphilippou. 'Frequency maps of LHC models'. In: *Proceedings of PAC1999*. New York, 2003, pp. 1554–1556. DOI: 10.1109/pac.1999.794171. URL: https://inspirehep.net/record/499744/files/TUP35.PDF.

[26] J. Laskar, C. Froeschlé and A. Celletti. 'The measure of chaos by the numerical analysis of the fundamental frequencies. Application to the standard mapping'. In: *Physica D: Nonlinear Phenomena* 56.2-3 (1992), pp. 253–269. ISSN: 01672789. DOI: 10.1016/0167-2789(92)90028-L.

[27] J.-P. Koutchouk and G. Sterbini. 'An Early Beam Separation Scheme for the LHC Luminosity Upgrade'. In: *Proceedings of EPAC2006*. Edinburgh, 2006, pp. 2134–2136. URL: https://accelconf.web.cern.ch/accelconf/e06/PAPERS/WEPCH094.PDF.

[28] R. de Maria, S. Fartoukh and M. Fitterer. 'HLLHCV1.1: Optics Version for the HL-LHC Upgrade'. In: *Proceedings of IPAC2015*. 2015. ISBN: 9783954501687. URL: https://cds.cern.ch/record/2112237.

[29] M. Berz, B. Erdélyi and K. Makino. 'Fringe field effects in small rings of large acceptance'. In: *Physical Review* 3 (2000), pp. 1–11. ISSN: 1098-4402. DOI: 10.1103/PhysRevSTAB.3.124001. URL: http://www.bt.pa.msu.edu/pub/papers/fringeprstab/fringeprstab.pdf.

[30] H. A. Enge. 'Focusing of Charged Particles'. In: *Deflecting Magnets* 2 (1967), pp. 203–264.

[31] A. J. Dragt. *Lie Methods for Nonlinear Dynamics with Applications to Accelerator Physics*. December. 2017. URL: http://www.physics.umd.edu/dsat/dsatliemethods.html.

[32] A. Wolski. *Linear Dynamics in Particle Accelerators*. 2012. URL: http://pcwww.liv.ac.uk/~awolski/.

[33] Y. K. Wu, E. Forest and D. S. Robin. 'Explicit symplectic integrator for s-dependent static magnetic field'. In: *Physical Review E - Statistical Physics, Plasmas, Fluids, and Related Interdisciplinary Topics* 68.4 (2003). ISSN: 1063651X. DOI: 10.1103/PhysRevE.68.046502.

[34] A. Wolski. *Nonlinear Dynamics for Particle Accelerators*. 2006. URL: http://pcwww.liv.ac.uk/~awolski/.

[35] S. I. Bermudez. *"Production of numeric fringe field grid data"*. Personal communication. 15th Feb. 2013.

[36] A. Wolski. *"Fitting of the Enge field to the numeric field"*. Personal communication.

[37] A. Wolski. *"Providing parsers for importing MAD to SAMM"*. Personal communication.

[38] MathWorks. *MATLAB Documentation - fzero - Root of nonlinear function*. URL: https://uk.mathworks.com/help/matlab/ref/fzero.html (Accessed: 28 May 2019).

[39] R. P. Brent. *Algorithms for Minimization without Derivatives*. Prentice-Hall, Englewood Cliffs, NJ, 1973. ISBN: 0-13-022335-2.

[40] A. Szczepkowicz. 'Application of transfer matrix and transfer function analysis to grating-type dielectric laser accelerators: Ponderomotive focusing of electrons'. In: *Physical Review Accelerators and Beams* 20.8 (2017). ISSN: 24699888. DOI: 10.1103/PhysRevAccelBeams.20.081302. URL: https://journals.aps.org/prab/pdf/10.1103/PhysRevAccelBeams.20.081302.

[41] A. V. Oppenheim. *Discrete-time signal processing*. Pearson Education India, 1999.

[42] GNU Project. *"The GNU C Library documentation"*. URL: https://www.gnu.org/software/libc/manual/html_node/Infinity-and-NaN.html (Accessed: 21 Dec. 2019).

[43] W. Schadow. *"B-Spline Library"*. Code is published online. URL: http://www.wolfgangschadow.com/software/ (Accessed: 16 Feb. 2019).

[44] Rogue Wave Software. *"IMSL Maths Library"*. "There is also https://docs.roguewave.com/imsl/fortran/6.0/math/default.htm?turl=bs3in.htm and https://docs.roguewave.com/imsl/fortran/6.0/math/default.htm?turl=bs3vl.htm". URL: https://docs.roguewave.com/imsl/fortran/6.0/math/default.htm?turl=bsnak.htm (Accessed: 17 Feb. 2019).

[45] C. De Boor et al. *A practical guide to splines*. Vol. 27. springer-verlag New York, 1978.

[46] M. Berry. 'Universal oscillations of high derivatives'. In: *Proceedings of the Royal Society A: Mathematical, Physical and Engineering Sciences* 461.2058 (2005), pp. 1735–1751. ISSN: 1364-5021. DOI: 10.1098/rspa.2005.1446. URL: https://pdfs.semanticscholar.org/5894/498141d9c79ee33dd13419118b37fb17888c.pdf%20http://rspa.royalsocietypublishing.org/cgi/doi/10.1098/rspa.2005.1446.

[47] Mathworks. *MATLAB Documentation - fit - Fit curve or surface to data*. URL: https://uk.mathworks.com/help/curvefit/fit.html (Accessed: 18 June 2019).

[48] G. Hoffstaetter. *Advanced Accelerator Physics*. 2010. URL: https://www.classe.cornell.edu/~hoff/LECTURES/10USPAS/ (Accessed: 18 June 2019).

[49] E. Mcintosh, R. D. Maria and M. Giovannozzi. 'Investigation of Numerical Precision Issues of Long Term Single Particle Tracking'. In: *Proceedings of IPAC2013*. 2013, pp. 942–944. ISBN: 9783954501229.

[50] R. De Maria, D. Gamba and F. Plassard. 'Update on the V1.4 optics'. 2018. URL: https://indico.cern.ch/event/750135/contributions/3104578/attachments/1702836/2742913/HL14-WP2-2.pdf.

[51] G. Arduini et al. 'Optics and Layout V1.2'. 2015. URL: https://indico.cern.ch/event/394926/contributions/938361/attachments/1131849/1618192/Layoutv1.2.pdf.

[52] R. De Maria. 'Status of v1.3 optics'. 2017. URL: https://indico.cern.ch/event/627307/contributions/2535226/attachments/1441305/2219084/OpticsV1.3_v2.pdf.